Partial Melting of Depleted Peridotite in the Earth's Upper Mantle and Implications for

Generation of Mid-Ocean Ridge Basalts

Thesis by

Laura Eileen Wasylenki

In Partial Fulfillment of the Requirements

for the Degree of

Doctor of Philosophy

California Institute of Technology

Pasadena, California

1999

(Submitted December 15, 1998)

Acknowledgments

I would like to express my grateful appreciation to all of the people who have helped me in various ways during my tenure at Caltech. Although time and space do not permit me to name everyone specifically, I would like to point out some individuals who have made particularly important contributions to my scientific training and general well-being.

First I thank my advisor, Ed Stolper, whose guidance, keen insight, and careful, thorough approach to problems have greatly aided my training as a scientist. One of my favorite things about Ed is his way of visualizing a problem as a simple thought experiment, carefully thinking it through, without ever misrepresenting or losing sight of the original, complex problem. I hope at least a small amount of that skill has rubbed off on me.

George Rossman, my academic advisor, has been a wonderful role model to me as a scientist, a teacher, and a human being. I thank him for his open door, for his unlimited curiosity and enthusiasm, for giving guidance but not advice, for encouragement, and for comic relief.

I am grateful to Peter Wyllie and Don Burnett for serving on my thesis advisory committee. I have enjoyed learning from them through classes, seminars, and occasional scientific discussion over the past six years.

I owe tremendous thanks to Michael Baker, who spent many, many hours instructing me in the laboratory, teaching me important concepts in petrology, and helping with interpretation of my work. His generosity and guidance are deeply appreciated.

Marc Hirschmann also deserves much credit for assistance with thermodynamic concepts, help with lab work, reassurance and encouragement, and cat talk. Others who

helped in significant ways with my work are John Beckett, Sally Newman, Paul Asimow, Glenn Gaetani, John Eiler, Adam Kent, Paul Carpenter, Chi Ma, and Eve Shaffer.

I also wish to thank all of the administrative staff members in Arms, whom I found extraordinarily competent, trusting, friendly, and caring. They brightened many of my days here!

Thanks also to the National Physical Science Consortium and NASA-Johnson Space Center, not only for financial support, but also for friendly encouragement and the knowledge that mentoring assistance was always available if needed.

I have had many wonderful friends during my stay at Caltech. I deeply appreciate all that they have done for me and thank them from the bottom of my heart. A few have been especially supportive and instrumental to my well-being and happiness, including Michele Karel, Phil Ihinger, Ariel Anbar, Marc Hirschmann, Liz Holt, Eve Shaffer, Jeri Standfield, Mark Abolins, Dave Evans, John Holt, Jean Hsieh, Diana Joseph, Adam Kent, Geoff Nichols, Rose Furkin, Gwyneth Williams, Magali Billen, Julia Goreva, Ronit Kessel, Liz Miura, Sujoy Mukhopadhyay, Greg Okin, and Beth Neroda.

Finally, I express gratitude to my family, Eugene and Barbara Wasylenki and Caroline and Mark Humphreys, without whose support and faith in me, past and continuing, I couldn't have been here in the first place. I feel very lucky to have their love and support.

Abstract

Peridotite in the earth's upper mantle undergoes polybaric, fractional melting as it rises adiabatically beneath mid-ocean spreading ridges. As liquid is continually extracted, peridotite becomes increasingly depleted in incompatible components. The amounts and compositions of partial melts of depleted peridotite are important parameters in models of MORB petrogenesis, but have not been well-constrained previously. I present partial melting experiments on a depleted peridotite composition at 10 kbar and 1250-1390°C. My experiments make use of small aggregates of glassy carbon particles into which partial melt is extracted at high temperature. I have been able to analyze low degree partial melts (<10%) and quantify the effects of incompatible element depletion on the melting behavior of peridotite. Special tests of the approach to equilibrium in this study confirm the validity of the aggregate melt extraction technique, which has sparked much debate in the literature (see Chapters 2 and 3 for details).

Melts of depleted peridotite differ in important ways from melts of fertile peridotite, mostly due to lower alkali contents and chemical consequences thereof. At low melt fractions, melts of depleted peridotite have less SiO_2, more CaO, and higher CaO/Al_2O_3 than melts of fertile peridotite at the same melt fraction. According to these results and others in the literature, solidus temperature is a linear function of incompatible major element content. Melt fraction at cpx-out is proportional to normative cpx in source peridotite.

Liquid compositions from this study are in good agreement with calculations using the quantitative models of Kinzler and Grove (1992a), Langmuir et al. (1992), and Ghiorso and Sack (1995). Calculations of polybaric, fractional melting of primitive mantle using the models of Langmuir et al. (1992) and Asimow (1997) indicate that about half of all liquid contributed to MORB is formed by partial melting of depleted peridotite.

The data presented in this thesis provide information about amounts and compositions of partial melts formed from depleted peridotite, an important upper mantle constituent beneath mid-ocean ridges, and can be used to improve quantitative models of MORB primary magma formation and further our understanding of MORB petrogenesis.

Table of Contents

List of Tables

List of Figures

Chapter 1: Introduction

Why study petrogenesis of mid-ocean ridge basalts?

Although recognized as such only in the mid-1960s, the worldwide chain of mid-ocean spreading ridges (MOR) and the mid-ocean ridge basalts (MORB) erupted therefrom are first-order features of the earth's surface. Sixty-five thousand kilometers of ridges circle the globe at present, and the basaltic rocks they have produced cover most of the ocean floors, about 60% of the earth's surface (Wyllie, 1976). Mid-ocean ridges produce an order of magnitude more volcanic rock per year than all other forms of terrestrial volcanism combined (Basaltic Volcanism Study Project (BVSP), 1981). Since the oldest of these rocks are only about 200 million years old, perhaps as much as twenty times the amount of basaltic ocean crust presently at the surface has been produced at ridges over earth's history, most of it subsequently subducted.

The earliest theories about mid-ocean ridges, based on little more than topographic data, explained them as mountain belts created by folding and deformation of previously flat ocean floor, much as folded mountain belts occur on continents (Bucher, 1957). Another theory, put forth to account for the relative motion of continents and observed high heat flow at ridge axes, was that the earth is expanding and that new surface is produced at ridges (Heezen, 1960). The lack of any ocean floor samples older than Cretaceous required that such expansion of the earth began only then, in violation of uniformitarianism. Later on it was proposed that ridges represent the surface manifestation of zones of upwelling in the earth's convecting upper mantle (Hess, 1962) and that subduction zones represent downwellings. His idea was broadly similar to that of Holmes (1928), but differed in that Hess proposed that continents ride passively along with the spreading ocean floor, rather than plowing through it (Le Grand, 1988). Hess's hypothesis was able to account for many of the observed properties of the ocean floor all

at once, but the causes of the topographic highs and low seismic velocities at ridges were still uncertain. Hess (1962) suggested that the elevation of ridges could be due to the volume expansion of peridotite and basalt as they become serpentinized by release of large volumes of water from hot, convecting mantle material beneath ridges. That the basalt which forms the shallowest layer of the ocean floor resulted from melting and volcanism at ridge axes was not yet recognized.

Discovery of zero-age basalts at ridges, age-progressive magnetic anomaly "stripes," and detailed studies of topography gave rise to the modern interpretation of mid-ocean ridges. It is now well known that ridges represent the eruption sites of basaltic magmas produced by partial melting of peridotite in the upper mantle. As mantle peridotite is carried upward in convection cells, it partially melts. The reason for this is illustrated in Figure 1-1, a schematic plot of pressure (or depth) versus temperature. Silicate rock is an extremely poor conductor of heat and thus rises adiabatically, or with negligible loss of heat to the surroundings. Upwelling mantle peridotite will thus follow a pressure-temperature path, called an adiabat, that is constrained by its heat content as it rises into shallower and cooler surroundings. Although the temperature of a parcel of mantle material rising along an adiabat decreases with decreasing pressure, it does not decrease as quickly as does the temperature required to initiate melting of that material. The temperature at which melting begins, or the solidus, is positively correlated with pressure. Since the slope of the adiabat is steeper than that of the solidus, a rising parcel of rock will begin to melt when it reaches the depth where the adiabat and solidus intersect. The slope of the adiabat flattens slightly as pressure continues to decrease because of the energy consumed by the heat of fusion as melting takes place. Less dense than its solid surroundings, the melted rock separates from the solid residue and rises, eventually erupting within a narrow zone along the sublinear chain of volcanic edifices that form the mid-ocean ridges.

Figure 1-2 is typical of cartoons depicting a cross section of a mid-ocean ridge and reflects our general knowledge of how MOR work. Melt is produced in a wedge-shaped region in the upper mantle. The melt rises, focuses to a narrow zone below the ridge, resides in a magma chamber for some time at crustal level, and then erupts in or near the axial rift valley of the ridge. The cartoon in Figure 1-2 is accurate to first-order, but many of the details are poorly constrained or unknown. Despite much work and increasingly tight constraints on some parameters in recent years, many properties of mid-ocean ridges and the mantle beneath them have yet to be characterized unequivocally, such as the shape and size of the partially molten zone, the depths at which melting begins and ends, how melt migrates, the degree to which liquid exchanges chemically with its surroundings as it migrates upward, the mechanism by which melt is focused into a narrow zone at crustal levels, and the size and shape of magma chambers in which magma resides before eruption. These aspects of how MOR work and how MORB are produced are extremely important issues for earth scientists to address because melting beneath spreading ridges is arguably the most important process by which crust is produced and by which the mantle and crust of the earth differentiate from each other.

Sampling of the lavas erupted at MOR in the past few decades has revealed that the compositions of MORB are quite remarkable. They display a high degree of uniformity and have several distinguishing chemical characteristics. When compared to basaltic rocks from other tectonic environments such as ocean islands, arcs related to subduction, or continental rift zones, the compositions of MORB span a very narrow range of compositional variability (Engel and Engel, 1964; Engel et al., 1965; BVSP, 1981). Nearly all MORB contain 49-50% SiO_2 by weight, have low concentrations of magmaphile elements such as Na, K, Ba, and Ti compared to basalts from other environments, and have distinctive trace element and isotopic signatures. In addition, the

thickness of oceanic crust produced at MOR is consistent. Young crust is typically 7 km thick (McKenzie and Bickle, 1988). While this varies by 1-2 km from place to place, it does not vary much more, nor does it vary substantially from one ocean basin to another, indicating that the overall amount of magma produced from upwelling peridotite is roughly constant. The flux of magma erupting on a given segment of ridge is dependent upon the spreading rate of the ridge, which can vary from 1 to 8 cm/year (BVSP, 1981), but the amount of lava produced per centimeter of spreading is fairly uniform. These observations indicate that MORB generation occurs in generally the same way along the entire 65,000 km of ridges around the globe and that there are no fundamental spatial or temporal differences in source rock composition, melting process, or post-melting processes such as low-pressure fractionation.

Although MORB display little variation in composition relative to igneous rocks in other tectonic environments, variations do exist. MORB crust becomes thicker, and MORB compositions appear to reflect higher degrees of melting and isotopic enrichment near hot spots. Even away from hot spots, chemical variations occur which are correlated with each other and with crustal thickness in systematic ways (Klein and Langmuir, 1987), as will be described below. Such systematic variations must reflect slight differences in the processes taking place to generate MORB. It is the goal of igneous petrologists who study MORB petrogenesis to study the compositions of MORB, to infer the process or combination of processes by which the rocks were formed, and to construct models of how the ridge system operates at depth and how the observed compositional and thickness variations arise. The next section reviews previous work done in this vein and sets the stage for the work presented in this thesis.

Review of previous work on MORB petrogenesis
Are MORB formed by direct melting of the mantle?

Once it was recognized that MORB are generated by partial melting of peridotite at zones of upwelling in the upper mantle, work began to constrain the melting process by which MORB magmas are produced and how the observed compositional variations arise. The overall compositional uniformity and widespread nature of MORB led some workers to believe that MORB might be primary magmas (BVSP, 1981), i.e., direct, partial melts of peridotite that were unchanged between original generation in the mantle and eruption. O'Hara (1968), however, presented compelling evidence that MORB cannot be primary melts of mantle peridotite. Since the residue of partial melting to form MORB primary liquids always contains olivine and orthopyroxene, which is known from sampling of abyssal peridotite, primary liquids must be in equilibrium with olivine and orthopyroxene at the pressure at which they formed. O'Hara (1968) demonstrated using phase equilibria from high pressure experiments that MORB compositions are not in equilibrium with orthopyroxene at any pressure and therefore cannot be primary melts of olivine- and orthopyroxene-bearing peridotite. He also noted that MORB compositions cluster near the olivine-plagioclase-clinopyroxene 1 bar cotectic. Thus O'Hara concluded that all MORB have undergone some degree of post-melting differentiation involving crystallization of olivine±plagioclase±clinopyroxene at low pressures.

The compositions of MORB upon eruption therefore reflect (1) the composition of the source rock that partially melted, (2) the melting process, whether by equilibrium or fractional fusion and to what degree, (3) any mixing of primary magmas or re-equilibration with peridotite through which melts migrate, and (4) low-pressure fractionation. Construction of a model which completely describes MORB petrogenesis thus requires an understanding of each of these factors.

The first of the four factors above, the composition of the MORB source, has been fairly well constrained by numerous approaches, including seismic velocity studies, petrographic, trace element, and isotopic analysis of mantle nodules and abyssal

peridotites, and cosmochemical constraints from analysis of chondrite meteorites. A detailed discussion of these constraints is not included here; for some examples of these approaches and more information, the reader is referred to the work of Ringwood (1975), Bryan et al. (1976), Maaloe and Aoki (1977), Hart and Zindler (1986), and McDonough and Sun (1995). Constraints on low-pressure processes have come from observation of phenocryst assemblages in MORB and from numerous experimental studies of the crystallization behavior of primitive MORB compositions (e.g., Grove and Bryan, 1983; Sack et al., 1987; Grove et al., 1992; Shi, 1993). Quantitative modeling of low-pressure crystallization has been presented by Yang et al. (1996) and Grove et al. (1992). The following section explains constraints on the melting process.

Efforts to identify primary magmas

Once it was established that most or all MORB have been affected by low-pressure crystallization, it became important to identify the compositions of primary magmas, or those liquids produced by direct melting of mantle peridotite before low-pressure processes take place. Two schools of thought arose in the 1970s and early 1980s as to the nature of MORB primary magmas. One group of workers believed that MORB primary magmas form at fairly shallow depths, about 8-10 kbar or 30-35 km, and experience slight degrees of olivine fractionation before eruption. This view was most strongly supported by Presnall et al. (1979), whose experiments in the simple system CaO-MgO-Al_2O_3-SiO_2 (CMAS) produced liquids at 9 kbar resembling the compositions (reduced to CMAS components) of the least-fractionated MORB basalts analyzed. Presnall et al. (1979) argued further that, since olivine phenocrysts in these least-fractionated basalts have forsterite numbers (Fo#$\equiv$100*Mg/[Mg+Fe], molar quantities) of 87-89, and olivine crystals in the basal sections of ophiolites have Fo# of 90-92, the basalts must only have experienced small amounts of fractionation; otherwise their Fo# would be substantially

lower than those in ophiolitic olivine crystals. In addition, he pointed out that if the least-fractionated basalts observed were the products of extensive fractional crystallization, one would expect to find evidence in the form of some glasses with even more olivine-rich compositions than any reported. He also challenged the conclusion of O'Hara (1968) that primitive MORB compositions are not in equilibrium with orthopyroxene at any pressure by citing some experiments in which pigeonite, in one case, and enstatite, in another, had crystallized near the liquidus of tholeiite compositions at 7.5 and 8 kbar (Kushiro and Thompson, 1972; Fujii and Kushiro, 1977). Finally, Presnall et al. (1979) suggested that the geothermal gradient beneath mid-ocean ridges may well be below the solidus temperature of lherzolite at pressures greater than about 9 kbar, making melt production at higher pressures unlikely.

Critics of this model believed instead that MORB primary magmas form at greater depths, ~30 kbar, as highly magnesian, picritic liquids that subsequently undergo extensive olivine fractionation at crustal levels. In particular Stolper (1980) argued that the conclusions of Presnall et al. (1979), while applicable in the four-component system CMAS, do not necessarily provide valid constraints on the behavior of peridotite and basalt in multi-component, natural systems. Stolper conducted experiments in which basaltic glasses were equilibrated at different temperatures and pressures within peridotitic capsules, thus enabling characterization of liquids in equilibrium with olivine and orthopyroxene over a range of conditions and location of the olivine-orthopyroxene-clinopyroxene multiple saturation points at different pressures. The results show that MORB compositions do not lie near the olivine-orthopyroxene cotectics at any pressure, except for a few olivine-rich compositions near the fringes of the MORB field, including those studied by Kushiro and Thompson (1972) and Fujii and Kushiro (1977). The least-fractionated MORB compositions are particularly far removed from saturation with olivine and orthopyroxene. The results also show, however, that MORB compositions

could be generated if primary magmas formed at 15-20 kbar and then lost substantial amounts of olivine and, in some cases, small amounts of plagioclase and/or clinopyroxene during fractional crystallization.

MORB are formed by near-fractional melting processes

The debate over the depth at which primary MORB liquids form was never resolved because new evidence from trace elements, radiogenic isotopes, and theory of melt migration showed that primary liquids are not formed at any single depth in the mantle, but by fractional fusion over a range of pressures. (In a fractional fusion process, instead of melt forming all at once and equilibrating fully with the residue before separating from it, melt is produced in infinitesimal increments, each of which is in equilibrium with the residue, but is then removed from the system and prevented from re-equilibrating as further increments of liquid are generated.) One of the most compelling arguments for fractional melting beneath mid-ocean ridges comes from rare earth element (REE) concentrations in clinopyroxene (cpx) grains in abyssal peridotites (Johnson et al., 1990). These cpx grains form part of the residue of melting and were thus in equilibrium with melt generated in their vicinity. The partitioning behavior of REE between cpx and coexisting liquid is well known, so by measuring the concentrations of REE in residual cpx grains, the concentrations of these elements in coexisting liquid can be inferred, and vice versa. Johnson et al. (1990) analyzed cpx grains from abyssal peridotites for their REE concentrations. Two plots of these compositions are shown in Figure 1-3. The concentrations of REE have been normalized to average C1 chondrite concentrations in order to smooth out extreme variations in abundances of the elements and to fit the data on one scale. The elements are listed in order of increasing compatibility in cpx from left to right. The heavy, nearly flat line at the top of each plot represents the REE pattern for cpx in MORB source peridotite before melting. This composition is a lherzolite chosen

for its light REE-depleted pattern and Nd and Hf concentrations. Johnson et al. (1990) carried out calculations of the REE pattern for residual cpx for both batch and fractional melting for melt fractions of 5% to 25%, the range of melt fractions needed to produce the amount of crust seen at MOR. Batch melting calculation results are shown in Figure 1-3a. It is clear from this diagram that no reasonable degree of batch melting will result in the strongly fractionated REE patterns observed in the actual cpx grains. Fractional melting, on the other hand, can easily account for the strongly fractionated REE in residual cpx grains, as shown in Figure 1-3b. Therefore, the melting process that produces MORB primary magmas must be a fractional or near-fractional process. When peridotite crosses its solidus, a small amount of melt is generated and then separates from the residue. Another small increment of melting occurs when the peridotite rises a bit more, and so forth. For other compelling lines of evidence to support the theory of fractional melting beneath MOR, the reader is referred to the U-Th series disequilibria work of Newman et al. (1983) and Ben Othman and Allègre (1990) and papers on the likelihood of small melt fractions separating from solid peridotite residue by Waff and Bulau (1979), McKenzie (1984, 1985, 1989), von Bargen and Waff (1986), Daines and Richter (1988), and Watson (1991).

The discovery that the MORB melting process is near-fractional led to important advances in models of major element chemical variations in MORB, most notably the work of Klein and Langmuir (1987) and Langmuir et al. (1992). Klein and Langmuir (1987) corrected MORB compositions for low-pressure fractionation and determined average compositions for ~100 km-long ridge segments. They then recognized a strong worldwide correlation between the chemistry of primitive MORB compositions and the depth of the water column above the ridge axis. (Water depth above the ridge crest is a proxy for crustal thickness, thin crust correlating with deep water and thick crust with shallow water. This can be simply understood as isostatic compensation and is borne out

by seismic measurements of crustal thickness.) In particular, Klein and Langmuir (1987) pointed out that the Na content of their averaged, corrected compositions ($Na_{8.0}$, or Na_2O content of compositions corrected to 8 wt% MgO) is strongly correlated with water depth, thus inversely correlated with crustal thickness. This correlation is presented in Figure 1-4a. The explanation for this observation rests on the known incompatibility of Na in mantle minerals during partial melting; where the axial water depth is greatest, crust is thinnest. Less crust implies a small overall melt fraction in that location and a high concentration of incompatible elements such as Na. A thicker crust would imply a greater melt fraction, resulting in dilution, and thus lower concentrations of incompatible elements. In addition, Fe content ($Fe8.0=FeO*$ content of compositions corrected to 8 wt% MgO) is negatively correlated with axial depth and therefore positively correlated with crustal thickness, as shown in Figure 1-4b. It is known from experimental work that Fe content of partial melt increases with pressure of melting (Jaques and Green, 1980; Langmuir and Hanson, 1980), so Klein and Langmuir (1987) inferred from the correlation that thick crust implies a higher mean pressure of melting.

Putting these observations together, Klein and Langmuir (1987) proposed that temperature differences from one location to another in the mantle lead to the observed variations. Figure 1-5 illustrates their model. In places where the mantle is relatively hot (case X in Figure 1-5), peridotite crosses its solidus at greater depth, melts to a greater extent with a higher mean pressure, and produces a thicker crust with relatively low Na content and high Fe content. Likewise, in areas where the mantle is relatively cold (case Y in Figure 1-5), peridotite reaches its solidus at a shallower lever, melts less at smaller mean pressures, and produces a thinner crust with higher Na content and lower Fe content.

While this model explains the "global trend" in corrected MORB compositions very well, Klein and Langmuir (1987) also point out that, within each segment of ridge from

which compositions were averaged to form the global trend, individual compositions form trends at high angle to the global trend. These trends collectively are called the "local trend," and they are attributed to source heterogeneity. The importance of source heterogeneity and how it can affect the compositions of primitive MORB liquids is a major issue in this thesis and will be discussed below and in Chapters 3 and 4.

The model of Klein and Langmuir (1987) fits the observed chemical variations in MORB extremely well, and is currently the most popular of several models in the literature. One alternative view by Shen and Forsyth (1993) contends that melting begins at the same depth from place to place, but the conductively cooling lithospheric lid has spatially varying thickness, causing melt to cease at different depths, thus leading to different total amounts and compositions of liquids.

Quantitative modeling of MORB petrogenesis

During the past ten years, much effort has been expended towards quantitative modeling of MORB petrogenesis. Several models are now the literature, i.e., McKenzie and Bickle (1988), Niu and Batiza (1991), Kinzler and Grove (1992a, 1992b, 1993), Langmuir et al. (1992), and Ghiorso and Sack (1995, and references therein), employing different approaches to calculating the amounts and compositions of melts generated by partial melting of peridotite. All of these models rely to varying extents on experimental data for calibration, since there is no *a priori* method for predicting the composition of a partial melt in a complex, multi-component system. The importance of these models is that, while experiments are the best way to determine what liquids are formed during partial melting, it is only practical to conduct experiments that simulate equilibrium, or batch, melting. Because the MORB formation process involves near-fractional melting, models must be constructed which make use of experimental data, but calculate fractional melting processes. It is beyond the scope of this thesis to discuss in detail the

approaches, merits, and drawbacks of all of the modeling approaches taken to date, but a

few of them warrant some explanation, as my experimental results will be compared to

some of the model calculations in Chapter 4.

The model of Kinzler and Grove (1992a) and Kinzler (1997) uses data from

experiments on partial melting of fertile peridotite to calculate a melting reaction for a

given spinel lherzolite composition. Applying the phase rule for an eight-component

system with five coexisting phases, a partially molten peridotite system has five degrees

of freedom. When pressure, melt fraction, liquid TiO_2 concentration, Mg#

($100*Mg/[Mg+Fe]$, molar), and NaK# ($100*Na_2O+K_2O/[Na_2O+K_2O+CaO]$, by weight;

this parameter accounts for two of the eight components) are specified, the temperature

and the composition of the liquid in terms of the mineral components Qtz, Plag, Oliv, and

Cpx are fixed. The relationships between the independent and dependent variables are

established by multiple linear regression on the experimental database. In practice, when

given the initial composition and mode of a source peridotite and a starting pressure, the

program will calculate equilibrium melt compositions for either equilibrium or fractional

melting, isobaric or polybaric, with or without retention of some of the liquid within the

residue for fractional melting. The advantage of this approach is that it allows modeling

of many different melting processes. The main drawback is that it relies on peridotite

melting experiments of which few of high quality have been published. In addition, since

there are particularly few data at very low melt fractions (<10% liquid by weight), the

program is not well-calibrated very near the solidus (Baker and Stolper, 1994). It is

difficult to know how accurate the program is in regions of composition space that

require extrapolation of existing experimental data. This issue is part of the motivation

for the work in this thesis.

Langmuir et al. (1992) predict liquid compositions for melting with and without

clinopyroxene in terms of Na_2O, MgO, TiO_2, and FeO* by using constraints on partition

coefficients from a large experimental data set. Since experiments need not contain all of the phases in lherzolite (olivine, orthopyroxene, clinopyroxene, plagioclase ± spinel ± garnet) to yield partition coefficient information, this method is calibrated with a larger experimental data set than that used by Kinzler and Grove (1992a). The program is able to predict liquid compositions and calculate aggregate liquids that form by mixing increments of liquid produced by near-fractional melting. The calculated liquid compositions for equilibrium melting at 10 kbar compare favorably with independent peridotite melting experiments (Baker et al., 1995, and Chapter 4). One potential drawback of the model is that since melt productivity, or how much liquid is produced at each decrement of pressure, is poorly known, it is assumed in this model to be linearly correlated with pressure. Asimow (1997) has since shown that this relationship is likely not linear, but the errors engendered by this assumption are not yet precisely known. Another disadvantage of this approach is that the program only predicts compositions in terms of a few components.

The MELTS program (Ghiorso and Sack, 1995, and references therein) calculates equilibrium phase assemblages and compositions by minimizing thermodynamic energy functions. MELTS is calibrated with data from experiments in systems relevant to igneous processes and from measurements of the thermodynamic properties of relevant solid and liquid phases. An important advantage of this approach over the previous two is that many important chemical components and phases, including some trace elements, volatiles, and accessory minerals, can be considered all at once. MELTS can be applied to a wide range of melting, crystallization, and reaction problems, but its accuracy depends on how much high-quality calibration data is available for the conditions and compositions of interest. The program has some known inaccuracies, such as an offset in temperature and overstabilization of orthopyroxene relative to other phases. It also sometimes displays unexpected behavior very near the solidus, where calibration

information is essentially nonexistent. Although these problems make MELTS unable to predict phase compositions very accurately, MELTS is able to predict chemical *trends* quite well and is an important tool for investigating many processes in igneous petrology.

Motivation for experimental study of depleted peridotite melting and thesis summary

One factor that all of these models are unable to take into account fully is partial melt contributed to MORB by melting of peridotite depleted in incompatible elements. An important and necessary consequence of fractional melting is depletion of the source peridotite in incompatible major and trace elements. As small increments of liquid are removed from the peridotite, those components which are incompatible within the peridotite's constituent minerals will partition into the liquid phase, and the concentrations of these components will drop markedly in the solid residue. The composition of the rock from which melt is generated changes continuously during fractional melting; it becomes increasingly refractory, and the amounts and composition of liquids produced from it also change. The shallow parts of the melting zone beneath ridges are likely dominated by depleted peridotite, which thus plays a substantial role in determining the compositions of MORB magmas. Unfortunately very little information about the melting behavior of depleted peridotite is available. The models discussed above rely on partial melting experiments for their calibrations, but almost no experiments have been previously conducted on depleted peridotite. There are qualitative expectations of the effect of source depletion, such as a higher solidus temperature at a given pressure and production of less liquid. Also, low concentrations of highly incompatible elements such as Na and Ti should lead to relatively low concentrations of these elements in partial melts from depleted peridotite and likely result in other chemical changes in the liquids, but quantitative information concerning these effects is needed for

effective construction and calibration of models of MORB petrogenesis such as those just described.

The objective of this thesis project is to characterize the melting behavior of depleted peridotite and provide information about its melting behavior which will aid in construction of better and more quantitative petrogenetic models for MORB formation. Using a new experimental technique that makes possible direct measurement of the amounts and compositions of experimentally-generated partial melts, even at very low degrees of melting (<5%), I have conducted experiments to evaluate the effects of source depletion on partial melting of mantle peridotite.

The experimental technique is described in detail in Chapter 2. This chapter includes a review of previous attempts to circumvent experimental difficulties which have made partial melting experiments hard to interpret in the past. The development and refinement of the technique used in this project, including several variations other workers and I have tried, are then described for the benefit of others who may wish to pursue this technique. The final part of the chapter concerns controversial criticisms of this technique and the results of special tests designed to dispel those criticisms.

Chapter 3, which together with much of Chapter 4 will be submitted for publication in similar form, contains the results of partial melting experiments on depleted peridotite at 10 kilobars pressure. It includes a restatement of the purpose of conducting 10 kbar partial melting experiments, detailed experimental and analytical methods, and results, including those from the special tests of equilibrium described in Chapter 2. Mass balance calculations of phase proportions in the charges and melting reaction are also presented. An appendix to this chapter contains calculations of oxygen fugacity within one of the experimental charges based on the compositions of coexisting olivine, orthopyroxene, and Fe-Pt alloy. Oxygen fugacity is calculated using two different

methods, which yield similar results. I then compare the results to estimates from the literature of oxygen fugacity in the shallow upper mantle.

In Chapter 4 the results of the 10 kbar experiments are compared with previous experimental work on fertile peridotite in order to highlight the effects of source depletion. The compositional dependences of solidus temperature, isobaric melt productivity, and the melt fraction at which clinopyroxene is exhausted from partially melting peridotite are quantitatively addressed. I also present a comparison of my experimental partial melt compositions with those predicted by three currently popular quantitative models of mantle melting. Finally, I include an assessment of the proportion of liquid contributed by depleted peridotite during formation of MORB based on the algorithms of Langmuir et al. (1992) and Asimow (1997) and on a comparison of experimentally-produced melts of fertile and depleted peridotite to MORB compositions corrected for low-pressure fractionation. The chapter ends with conclusions from the 10 kbar study. Some of the discussion presented here represents joint efforts by myself and others, primarily Michael Baker, who is acknowledged for significant scientific contributions to this chapter.

Figure 1-1. Schematic diagram of the relationship between a peridotite adiabat and solidus in the upper mantle. The solidus is the boundary between solid peridotite and partially molten peridotite. The dashed line represents the adiabat, or the pressure-temperature path taken by a parcel of mantle material isentropically upwelling. The square and arrow in the lower right represent the parcel of upwelling material and its path along the adiabat.
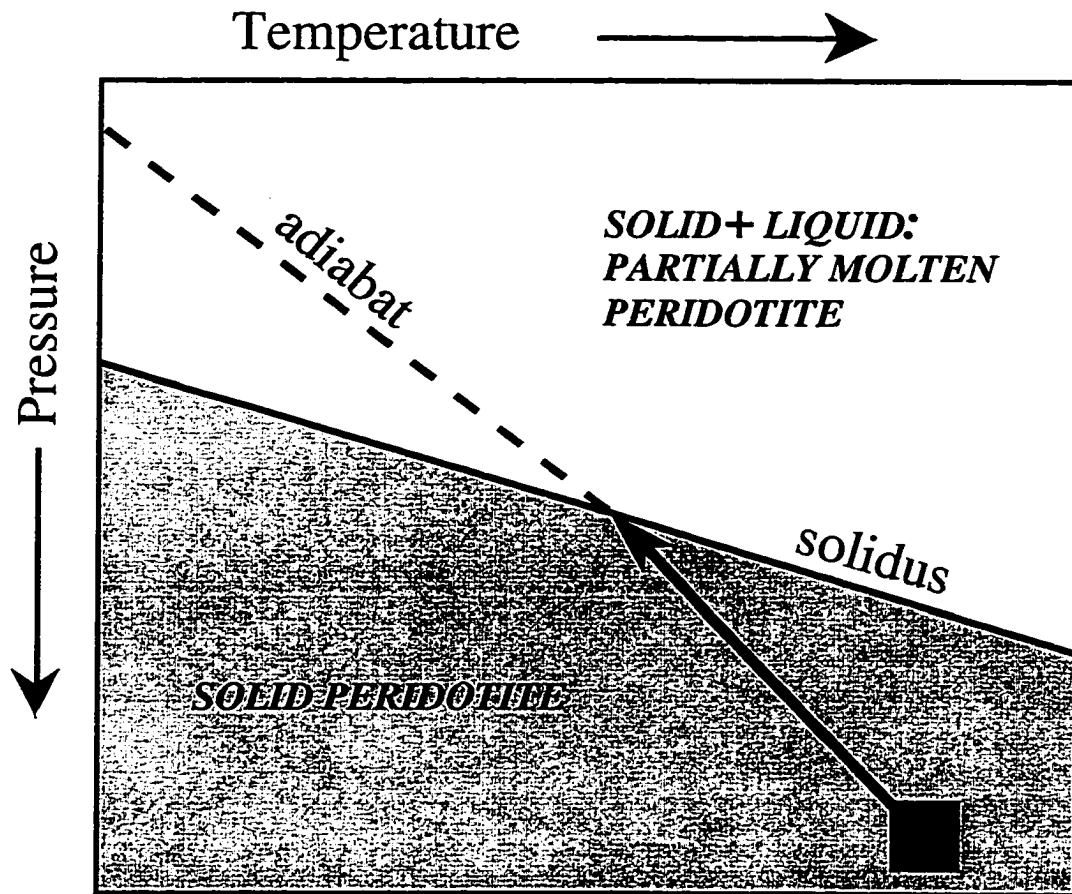
Figure 1-2. Cross-sectional cartoon of a mid-ocean ridge. Upwelling peridotite rises

beneath the ridge axis and partially melts. The melt separates from the solid residue and

eventually rises to and erupts at the ridge axis. The residue turns the corner and flows

outward underneath the newly created oceanic crust.

ridge axis

magma chamber?

mantle flow

zone of partial melting
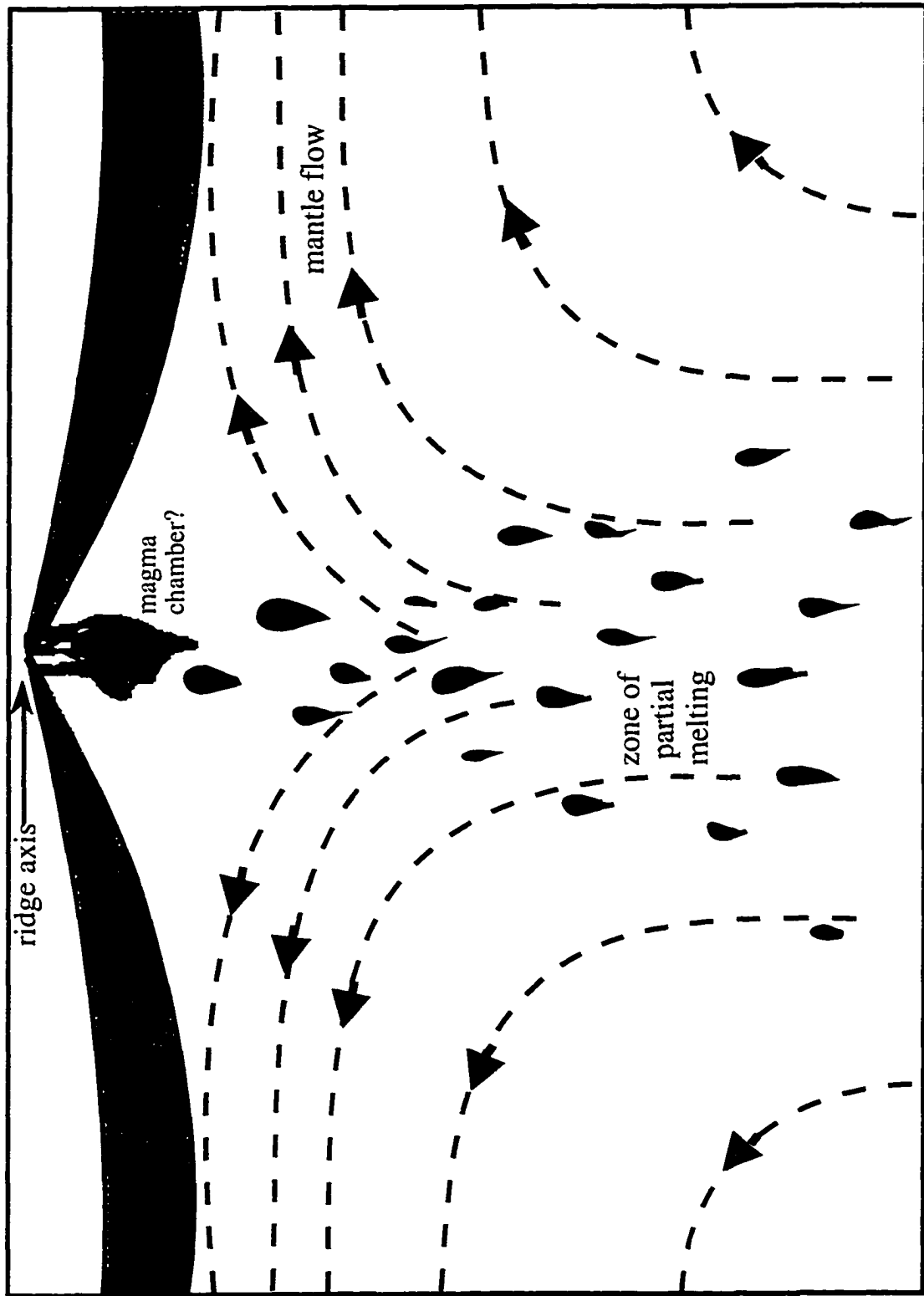
Figure 1-3. REE concentrations in residual cpx, drawn after Johnson et al. (1990).

Squares and circles joined by thin line segments represent analyses of cpx in abyssal

peridotites. Solid, black line represents REE concentrations in source cpx. Thick, gray

lines represent REE concentrations expected in residual cpx after (a) batch melting and

(b) fractional melting. Dashed line in each plot corresponds to 5% melting; solid lines

correspond to 25% melting. Batch melting calculations are unable to match the strong

fractionation patterns observed in abyssal cpx, whereas fractional melting can reproduce

the measured trends.
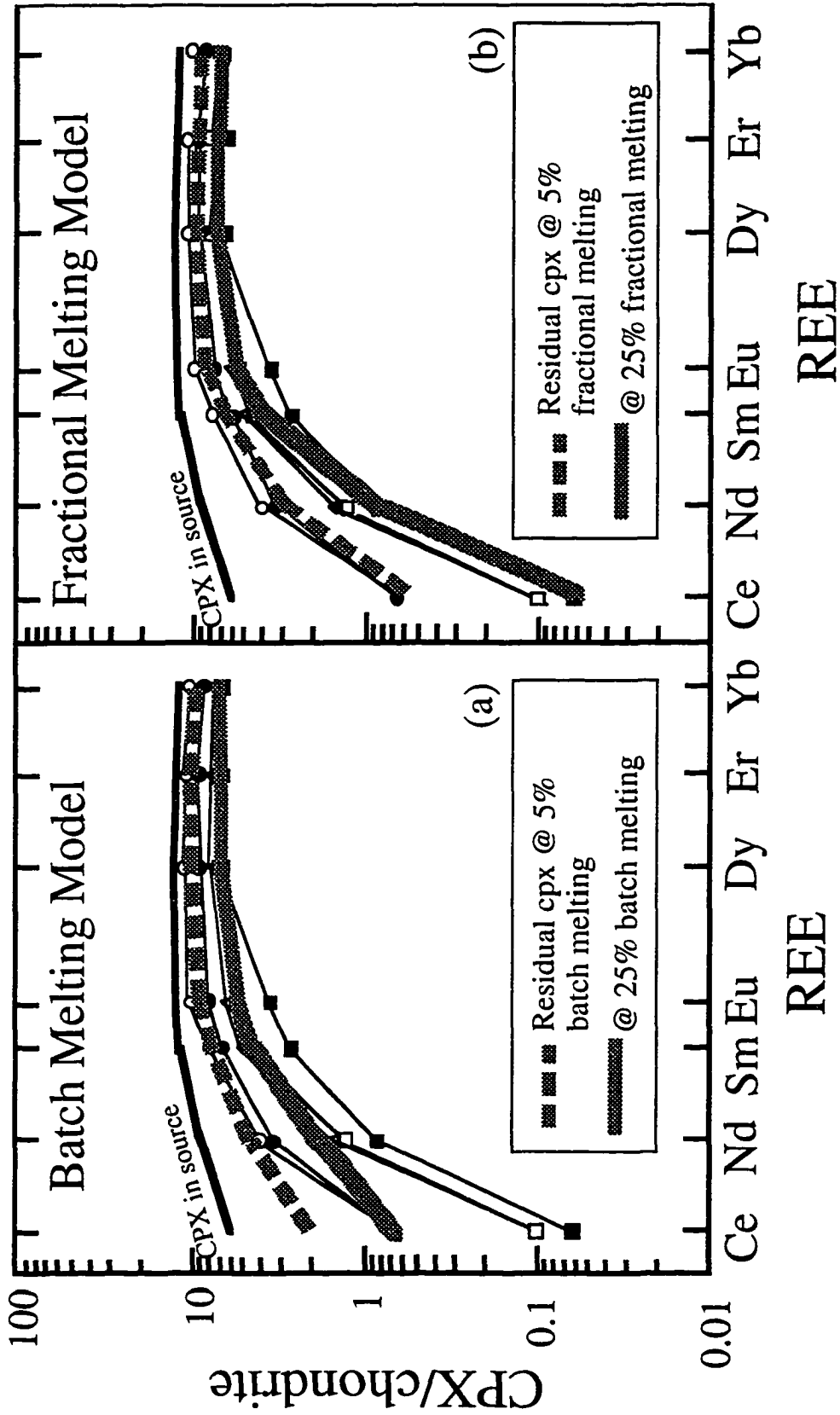
Figure 1-4. Global trend in MORB of $Na_{8.0}$ and $Fe_{8.0}$ versus axial depth, drawn after

Klein and Langmuir (1987). $Na_{8.0}$ and $Fe_{8.0}$ are the Na_2O and FeO^* (all Fe calculated as

FeO) contents in weight percent of MORB after correction for low-pressure fractionation

to 8.0 wt% MgO.

Depth to ridge crest (meters)
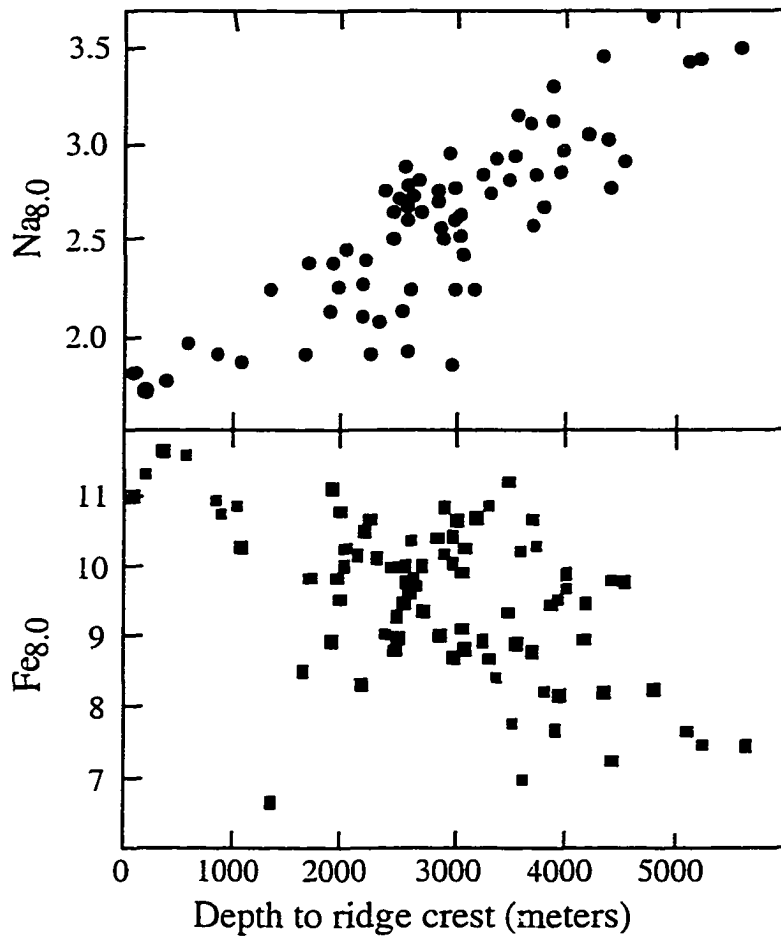
Figure 1-5. Model of Klein and Langmuir (1987). Case X represents melting of peridotite in relatively hot mantle. The solidus is intersected deep, at ~40 kb, and the extent of melting is large, producing a thick oceanic crustal section. In case Y, the mantle is colder, the solidus is not intersected until peridotite rises to ~15 kb, and less melt is produced, leading to a thinner crustal section.

Temperature ⟶

Pressure ↓

15kb

40kb

40% melt
30% melt
20% melt
10% melt

solidus

Y

X

Y

X

sea level

40% melt

30% melt

20% melt

10% melt

10%
melt

solidus = 15kb

solidus = 40kb
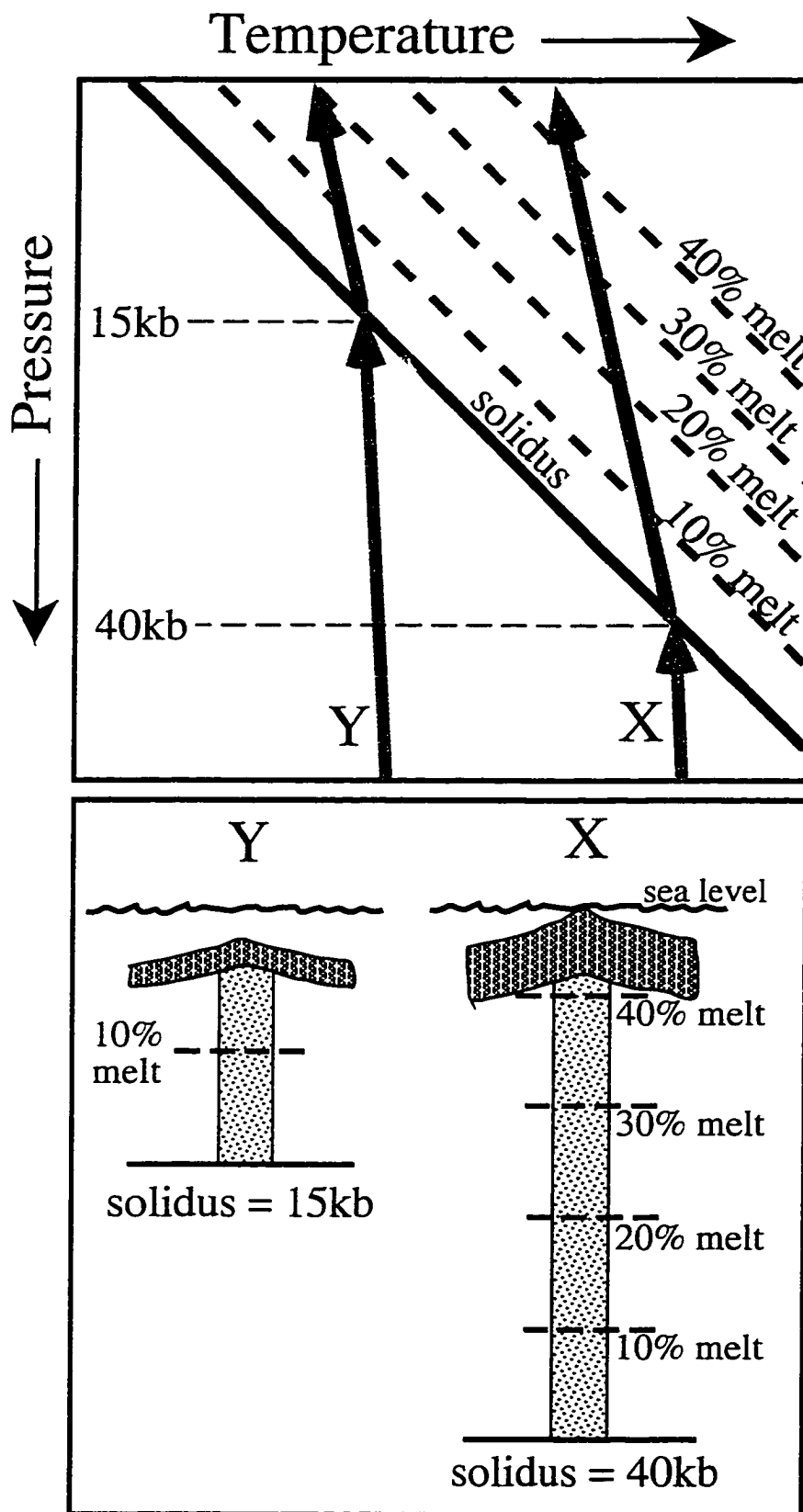
Chapter 2: Development of the melt extraction and melt segregation experimental techniques

A review of challenges in conducting partial melting experiments on peridotite

Partial melting experiments have an important role in the study of MORB petrogenesis as well as other petrologic problems. Because there is no way to predict *a priori* the amounts and compositions of liquids produced by partial melting in complex, multi-component systems, the best information about such processes often comes from laboratory simulation. By partially melting the source rock of interest over a range of relevant conditions and analyzing the phases in the resulting experimental charges, one can acquire the information needed to construct forward models of the melting process and to constrain the origin of a suite of rocks.

Although the concept of conducting partial melting experiments is straightforward, several technical problems can complicate interpretation of the results. First, because sample size and run duration in laboratory experiments can be orders of magnitude smaller than in the natural systems the experiments are intended to simulate, experimentalists rely on achievement of equilibrium within a closed system in order to obtain results that are reproducible and meaningful. In a good experimental study, achievement of equilibrium must be carefully demonstrated before the results can be used to constrain models of natural processes.

Attainment of equilibrium depends in part on having a closed system. To ensure a closed system free of contamination and exchange of material with the exterior, the samples in peridotite partial melting experiments are sealed within capsules before they are placed within the piston cylinder assembly. Capsule materials must be chosen so as to withstand the pressures and temperatures of interest without rupturing or interacting

chemically with either the sample material or the pressure assembly. For peridotite

melting experiments, Pt or Ag-Pd capsules are most common, as they have extremely

high melting temperatures, are essentially insoluble in peridotite and partial melts thereof,

and can block diffusion in or out of the sample of almost all species other than hydrogen.

Unfortunately, Fe from the peridotite will readily alloy with Pt or Ag-Pd, causing loss of

Fe from the experimental charge (Ito and Kennedy, 1967; Merrill and Wyllie, 1973) and

an increase in oxygen fugacity within the peridotite. Graphite inner capsules eliminate

this problem for all but the longest duration experiments, but the use of inner capsules

further limits the amount of material that can be loaded and imposes an oxygen fugacity

constraint of its own. Samples in this study were contained within graphite inner

capsules and Pt outer capsules. Iron loss occurred in only one or two of the longest

duration experiments, as discussed in Chapter 3.

A source of contamination that is difficult to avoid is adsorbed water on sample

material. Sample material is usually ground finely in order to promote full chemical

equilibration of mineral grains, but fine-grained powder is hygroscopic. Even a small

amount of water within the system can have profound effects on the melting behavior of

peridotite, so it is necessary to dry starting material carefully when loading capsules. It is

virtually impossible to eliminate all adsorbed water, so care must be taken to watch for

effects of the presence of water in experimental results and, in some cases, to analyze

samples for their water contents. For this study, sample powder was dried above the

boiling point of water for at least two hours prior to being loaded in capsules, and loaded

capsules were also dried for several hours before they were welded. The water contents

of the glasses within three charges were measured by ion microprobe. The highest value

was 1.2 wt% H_2O in sample #3 (1310°C). According to preliminary MELTS

calculations, this can be expected to decrease the normative olivine content of the liquid

by 5-7% and increase the SiO_2 content by about 1 wt%. Indeed the glass in this sample

has ~1 wt% more SiO_2 and MgO and slightly more FeO* in the glass than experiment #22, which had 0.3% H_2O in the glass and was run at 1300°C. It is unknown at this point whether the differences between these two experiments are due to the presence of water or to temperature uncertainties, but this issue will be explored further in upcoming work, perhaps including more ion probe analyses (Wasylenki et al., in preparation). The drying procedures and ion microprobe measurements are discussed in detail in the experimental and analytical methods section of Chapter 3.

Attainment of equilibrium often occurs by diffusion of components between and within the various phases in an experimental charge, as well as by dissolution and re-precipitation of solid phases, and therefore run durations must be sufficient to allow homogenization and equilibration to occur. The time required depends on the temperature and pressure of the experiment, diffusivity of various components in the phases present, the amount of liquid present, grain size of the solid phases, and the compositional "distance" between the initial and final states of the system. The most common way to determine the time required to reach equilibrium is to run a series of experiments at the same conditions for different durations and determine the length of time beyond which no compositional changes occur. Independent demonstration that the final composition represents equilibrium is usually required. Reversal experiments, in which the equilibrium state is approached from opposite directions in temperature, pressure, or some other controlled parameter, provide the most convincing demonstration of equilibrium. In addition, some crystalline phases, including pyroxenes and feldspars, are notorious for rarely achieving equilibrium on laboratory time scales. Because of this, it is important to analyze crystalline phases carefully, characterize well the extent and nature of inhomogeneities within solid phases, and assess the implications of disequilibrium for interpretation of the experimental results. Reversal experiments and

detailed crystal analyses for this project are discussed below in the section on criticism of the melt extraction technique and in Chapter 3.

The quench modification problem

One additional technical problem with partial melting experiments in particular has caused by far the most frustration and difficulty in interpretation of results. Once a sample has successfully reached equilibrium at high temperature and pressure, it must be returned to room temperature and pressure for polishing and analysis. The sample is brought to room temperature as quickly as possible by suddenly shutting off power to the experimental apparatus, but during the few seconds required for the temperature to drop, some compositional modification of the partial melt will occur. As the temperature drops below the liquidus of the partial melt, the liquid will begin to crystallize. Crystals adjacent to liquid will grow "quench rims," removing crystal-compatible components from the nearby liquid, thus driving the liquid's composition away from high temperature equilibrium (Cawthorn et al., 1973; Green, 1973; Nicholls and Ringwood, 1973; Jaques and Green, 1979). Compositional modification will affect the liquid as much as 30 micrometers away from the nearest crystal. Especially at low melt fractions (and it is low melt fractions that are most important to study in order to model near-fractional processes occurring beneath mid-ocean ridges), it has been impossible in the past to find unmodified glass within the sample for analysis.

Past attempts to overcome the quench modification problem

Petrologists have tried several different approaches to circumventing the quench modification problem in melting experiments. The first of these involves studying simple system analogs to natural peridotite-basalt systems (e.g., Presnall et al., 1978; Presnall et al., 1979; Walter and Presnall, 1994). Studies within the simple systems CaO-MgO-

Al_2O_3-SiO_2 and Na_2O-CaO-MgO-Al_2O_3-SiO_2 have much lower variance than natural,

multi-component systems, such that melting reactions are invariant or univariant. Since

phase compositions are fixed, phase proportions need not be; thus experiments can be

done which yield large amounts of liquid, occurring within the charge in pools whose

interiors are free of quench modifications. This principle is illustrated quite well by

Walter and Presnall (1994, Figure 1), using the system Diopside-Anorthite-Albite (Di-

An-Ab) at 1 atmosphere pressure as an example. Figure 2-1 is modeled after the Walter

and Presnall figure and shows the univariant liquidus curve in the Di-An-Ab system,

along which liquid, diopside, and plagioclase coexist. Point y represents a model

peridotite composition that yields a small amount of liquid at 1225°C. Point 1 shows the

composition of this liquid, and the other two apices of the three-phase triangle indicate

the compositions of diopside and plagioclase. The composition of the small quantity of

liquid cannot be easily measured in an experimental charge, as it will be modified by

quench crystal growth. Composition x, or any other composition within the three-phase

triangle, however, will yield the same phase assemblage and the same phase

compositions, but a higher proportion of liquid. The larger amount of liquid will likely

occur in pools within the experimental charge, some of them large enough that their

interiors are unaffected by quench crystal growth at the edges. While this approach does

make accurate determination of near-solidus liquids possible, it has a serious drawback.

Even though the components in CMAS and NCMAS represent 90-93% of the chemical

constituents in natural peridotite (Presnall et al., 1979; Walter and Presnall, 1994), other

components, most importantly K_2O, FeO, TiO_2, and Cr_2O_3, while low in abundance,

have critically important effects on phase relations and phase compositions in peridotite-

basalt systems (e.g., Baker et al., 1995; Hirschmann et al., 1998a). Although phase

relations and compositions can be readily and accurately determined in simple system

analogs, these results are not easily applied to the systems of interest.

Another approach to avoiding the quench modification problem consists of calculating the liquid composition by mass balance after analyzing solid phases and determining the mode by point counts. This strategy was adopted by Jaques and Green (1980) in partial melting studies of MORB pyrolite-40% olivine and Tinaquillo lherzolite-40% olivine. These authors removed a substantial amount of olivine from the original peridotite compositions in order to increase the proportions of liquid and minor phases within their charges and facilitate point counting. In theory, if the composition of the subtracted olivine is the equilibrium composition and if the experimental charges are still saturated with olivine, olivine subtraction should have no effect other than to change the proportions of phases present. To execute this approach perfectly would require making separate starting material for each set of conditions studied, each with 40% equilibrium olivine *for that temperature, pressure, and melt fraction* subtracted from the peridotite composition. Since this is not practical, Jaques and Green (1980) subtracted an averaged olivine composition. Because the olivine removed is not quite of the right composition for many of the charges, the authors report that phases within some low melt fraction charges are richer in FeO^* (all Fe calculated as FeO) than expected. Also because of the reduced amount of olivine in the charges, Mg# ($100*Mg/[Mg+Fe]$, molar) in some phases, which is normally strongly buffered by olivine, changed more quickly than expected as a function of temperature (Jaques and Green, 1980). An additional consequence of olivine removal is that the alkali content of the bulk composition in the charges was relatively high, which may lead to compositional differences in the run products. It is difficult to evaluate the consequences of the approach taken by Jaques and Green (1980) because run durations in this study were extremely short, and thus their results may reflect failure to attain equilibrium as well as other effects.

A third strategy for circumventing quench-related problems is to conduct "sandwich experiments" (Stolper, 1980; Takahashi and Kushiro, 1983; Fujii and Scarfe, 1985;

Falloon and Green, 1987; Falloon et al., 1988; Robinson et al., 1998). In these experiments a layer of basalt that constitutes several percent of the charge is placed within the capsule and allowed to equilibrate with the surrounding peridotite. The pool of glass is large enough to contain liquid unmodified during the quench, and thus the composition of liquid in equilibrium with peridotite can be directly measured. A large number of experiments have been conducted using this approach, and while those studies have provided much useful information, the strategy has a major disadvantage similar to one encountered by Jaques and Green (1980) above: the added basalt significantly changes the bulk composition of the system under investigation. The basaltic liquid and peridotite will come to equilibrium with each other, but the system is rich in basaltic components compared to the peridotite composition, and phase compositions and proportions will be somewhat different from what they would be if the bulk composition were simply the peridotite composition of interest.

Recognizing this drawback, Robinson et al. (1998) conducted sandwich experiments iteratively. At each temperature studied, the glass from an initial sandwich at each experiment was analyzed, and a synthetic glass of that composition was added to peridotite for another sandwich experiment. This was repeated until the basaltic glass added to the charge underwent no significant compositional changes during the run. At this point, Robinson et al. (1998) inferred that, if no reaction took place between the liquid and peridotite during the last sandwich iteration, then the glass composition represents that of a partial melt of the peridotite at that temperature and pressure, although the amount of liquid present in the charge is clearly larger than the amount produced by partial melting. The resulting liquid compositions were also tested for multiple saturation with olivine, orthopyroxene, clinopyroxene, and spinel. Unfortunately the authors do not provide independent confirmation that the composition of the liquid in equilibrium with peridotite is necessarily the same as that produced by

melting (M. Baker, pers. comm.). If enough iterations are performed, and if the equilibrium liquids are, in fact, the same as partial melts, then this technique can provide valuable information about partial melt compositions. The amounts of melt produced, however, are difficult to deduce. Robinson et al. (1998) use a complicated method of determining the relative proportions of solid phases in their charges and measuring the bulk composition of their charges and are thus able to determine indirectly how much melt would be appropriate by mass balancing the phase compositions and relative proportions of solid minerals to the original peridotite compositions, but this method relies on the assumption that the proportions of solid phases in their charges are the same as they would be following partial melting and may not provide accurate information about the amounts of partial melt which would be produced during an actual melting process.

Principle behind the melt extraction technique

The melt extraction technique represents a new approach to overcoming the problems associated with quench modification. The technique was developed independently by Stolper's group at Caltech and Kushiro's group at University of Tokyo in the early 1990s. The original procedure was to place a layer of small diamond particles (several tens of microns in diameter) next to or within the powdered peridotite starting material (Figure 2-2). The diamonds have sufficient yield strength that when the charge is subjected to high pressure, pore spaces between the diamonds remain open, filled with air. The pressure within these pore spaces is unknown, but is presumably much lower that the pressure of the experiment, probably near atmospheric pressure. When the temperature is raised and a partial melt forms, the pressure gradient draws the liquid into the pore spaces within the diamond layer. Physically segregated from the crystalline residue, the melt within the diamond layer quenches to a crystal-free glass.

This enables direct analysis of the high temperature composition of the liquid without the changes caused in conventional experiments by quench modification. Even liquids produced by very low degrees of partial melting can be extracted and analyzed in this way, making it possible for the first time to acquire direct information about peridotite melting near the solidus. This is extremely important for studying the petrogenesis of MORB, since the compositions of low degree partial melts are most relevant to the near-fractional melting process taking place to form MORB.

Aggregates of diamonds were used in this way to investigate partial melting of several different peridotite compositions at pressures ranging from 10 to 30 kilobars and melt fractions as low as ~2 wt% (Baker et al., 1992; Hirose and Kushiro, 1992; Johnson and Kushiro, 1992; Kushiro and Hirose, 1992; Hirose and Kushiro, 1993; Baker and Stolper, 1994; Baker et al., 1995). In some cases the diamond aggregates were reduced in size and modified in shape or position within the capsule to ensure that the volume of pore space within the aggregates did not exceed the volume of partial melt generated, as this would lead to uncertainties in the pressure of the experiment.

Variations on the melt extraction technique

Although the high yield strength and inertness of small diamonds (~40-70 microns) within the peridotite charges make them an extremely good material for extracting melt, they present a problem: it is extremely difficult to polish a flat surface on a diamond-bearing sample for microprobe analysis. Some groups claim to have had some success polishing diamonds using colloidal silica polishing agents or special diamond lap wheels (W. Minarik, pers. comm.), but other experimentalists have looked for ways to avoid the need to polish diamonds.

Baker and Stolper (1994) and Baker et al. (1995) dug out the glass-filled diamond layer from charges and mounted this disaggregated material separately, such that some

glass particles could be polished and analyzed. The disadvantages of this approach are that (1) even when the diamonds and glass pieces are spread out in a separate mount, the diamonds still make it difficult to achieve a perfectly flat surface for analysis, (2) some of the glass bits may be lost in the transfer process, and (3) spatial information about which glass particles were close to or far away from the bulk silicate charge is lost.

Another technique, used by Hirose and Kawamoto (1995), does not involve addition of any material to the charge for the purpose of extracting melt. Instead, reentrants in the deformed capsule wall and the long, narrow cone at one end of the capsule act as traps for melt. Polishing is easy in this case, but the problems with this approach are that one must depend on luck to some extent to end up with bends in the capsule wall of appropriate size and shape to trap large melt pools (which becomes increasingly unlikely at low melt fractions) and that the range of conditions where this technique will work is limited, since graphite inner capsules cannot be used. Systems studied this way must be free of iron or at low enough temperatures to make possible use of capsule materials that do not alloy readily with Fe, such as Au.

Another approach to avoiding the difficulties associated with diamonds is to substitute another material which can be polished with diamond grit. An appropriate material must satisfy several requirements: (1) it must have sufficient yield strength to maintain pore spaces at high pressure, (2) it must be chemically inert with respect to peridotite and basaltic melt, neither reacting nor changing oxidation state at the conditions of the experiments, thus becoming soluble in melt or residue or evolving volatiles that can alter the system of interest, (3) the material should be readily wetted by silicate melts such that the glass-filled aggregate can be polished without excessive cracking or plucking. Very few materials satisfy the first two requirements. Hard elemental metals and compounds which were determined either by consulting phase diagrams or conducting experiments to react, oxidize, or dissolve at the relevant

conditions include tantalum metal, tungsten carbide, boron carbide, boron nitride (M. Baker, pers. comm.), and silicon carbide.

I made several attempts to use iridium powder, as it is quite hard and it is relatively inert, dissolving only a small amount of Fe from the peridotite. Fe loss from the sample is insignificant if only a small amount of Ir is added to the charge. Iridium powder was sieved to between 70 and 100 microns under ethanol and loaded into capsules either in a thin layer across the bottom or inside a small hole drilled into the floor of the graphite inner capsule. In most cases, liquid successfully flowed between particles of Ir, but the Ir apparently deformed subsequently at high temperature and pressure such that melt pools appeared in cross section to be completely surrounded by Ir and isolated from the rest of the partially molten peridotite charge. Figure 2-3 is a backscattered electron photomicrograph of one such charge. Even though some of the melt pools may have approached the composition of equilibrium partial melts, it is difficult to recognize or demonstrate this, and one would expect a large proportion of such experiments to contain no fully-equilibrated glass. I attempted to acquire powdered Os-Ir alloy, as its hardness and resistance to high-temperature deformation may be greater than for pure Ir, but I was unable to locate a source of such material.

The alternative to diamonds that has been most successful in this study is vitreous carbon (also called glassy carbon), a form of amorphous carbon hard enough to maintain pore spaces up to 50 kbar (M.Pertermann, pers. comm.) The carbon is easily polished with diamond grit, thus the charge can be prepared for analysis with spatial information preserved. Vitreous carbon is readily wetted by silicate liquids. The advantage of this behavior is that glass easily migrates around the outside surfaces of vitreous carbon particles and into any fractures which form within the vitreous carbon (see Figure 2-4, backscattered electron image of a typical charge).

Vitreous carbon does have some disadvantages, however. First, it can contain an unknown, but possibly substantial, amount of water (Wasylenki, unpublished results). The material must therefore be dried carefully before use in nominally dry melting experiments, and its use in water-bearing experiments is problematic, since water from the sample material may migrate into the vitreous carbon, either reacting to form CO and CO_2 or inhabiting pore spaces in the carbon (Wasylenki, unpublished results), as Ar has been shown to do up to 2 wt% (Gazis and Ahrens, 1991). Second, the rinds of melt around particles of vitreous carbon are often quite thin, making microprobe analyses difficult in some cases. As noted in Chapter 3, microprobe totals for glasses within vitreous carbon aggregates are often significantly lower than 100% because inclusion of some carbon within the analyses volume is unavoidable in some samples.

Another disadvantage is that although vitreous carbon has nearly always led to successful melt extraction at 10 kbar, preliminary attempts at 20 kbar have been problematic because of the rapid crystallization of the amorphous carbon to graphite at the high temperatures required to partially melt depleted peridotite at that pressure (>1380°C). (Previous work with vitreous carbon at very high pressures involved melting of hydrous phases at much lower temperatures. M. Pertermann, pers. comm.) Figure 2-5 is a photomicrograph of a 20 kbar charge in which glassy carbon completely crystallized to graphite within 46 hours at 1390°C. Based on images of samples run for different lengths of time, the carbon crystallizes to graphite at the edges first. It appears that as the crystallization front advances inward, cracks form in the vitreous carbon pieces, perhaps due to the volume change during crystallization. Because of the wetting properties of silicate melt on vitreous carbon, melt migrates into the cracks. The melt then becomes trapped inside the graphite and is unable to continue chemical exchange with the bulk sample. Although it is difficult to know whether the melt is completely surrounded by graphite in three dimensions, analyses of glass in several charges indicate that the pools

of melt within the graphite in each charge have a range of compositions that form rough trends on oxide variation diagrams, suggesting that different pools of melt within the charge approached equilibrium to varying extents.

Additional variations on experiments with vitreous carbon were designed and conducted in response to criticism of the melt extraction technique, as described below.

Controversy concerning the melt extraction technique

The validity of experiments conducted with the melt extraction technique has been the issue of some controversy in the last few years (Falloon et al., 1996; Baker et al., 1996; Wasylenki et al., 1996; Falloon et al., 1997). The debate arose over the results of Baker and Stolper (1994) and Baker et al. (1995), who observed dramatic changes in the melting behavior of fertile peridotite very near the solidus. The effects they reported include a large increase in liquid SiO_2 concentration, decrease in TiO_2 content, and changes in Fe and Mg partitioning between liquid and olivine. Although a robust explanation for these effects based on high alkali content in near-solidus liquids has since been presented by Hirschmann et al. (1998a), critics attributed them to disequilibrium phenomena that are artifacts of the aggregate melt extraction technique (Falloon et al., 1996; Falloon et al., 1997). The primary complaint is that at the beginning of an experiment, the low pore pressure within the diamond (or vitreous carbon) layer can affect the composition of liquid initially filling these pores, i.e., the initial liquid is not in equilibrium with the bulk peridotite at the nominal pressure of the experiment. This has been shown clearly; liquid compositions from short duration experiments are different from those produced in long duration runs at the same temperature and pressure (Johnson and Kushiro, 1992; Baker and Stolper, 1994). Critics of the melt extraction technique believe that because the melt is physically segregated from the bulk charge, this initial

disequilibrium condition cannot be overcome and that the resulting liquid compositions do not represent equilibrium partial melts.

Because of the possibility that the initial liquid filling pore spaces is far from equilibrium, Baker and Stolper (1994) and Baker et al. (1995) conducted two-stage diamond aggregate experiments. In the first stage, peridotite powder was partially melted without diamonds in order to allow liquid and crystals to remain in intimate contact and approach equilibrium closely. This charge was then quenched and re-loaded in a new capsule with diamonds. It is believed that the initial melt in the second stage will be close to the equilibrium composition; although it may be slightly affected by the pressure gradient and by quench modification incurred at the end of the first stage, very little change in composition should be needed to regain equilibrium. Results from one-stage and two-stage experiments are in excellent agreement. This indicates that any quench modification that occurred at the end of the first stage was undone during the second stage.

I began the experiments presented in this thesis as the debate over the melt extraction technique was beginning. Most of my experiments were done in two stages, as just described, but with vitreous carbon substituted for diamonds, as illustrated in Figure 3-2. The dramatic near-solidus effects reported by Baker et al. (1995) are not evident in my results for depleted peridotite melting, thus they cannot be simple artifacts of the experimental technique. Furthermore, the near-solidus effects observed by Baker et al. (1995) are also predicted by calculations using MELTS (Wasylenki et al., 1996; Hirschmann et al., 1996; Hirschmann et al., 1998a) for the Baker and Stolper composition, but not for the depleted composition I studied. Since none of these experiments are included in the calibration of MELTS, the program gives independent predictions of whether these effects will occur near the solidus. In addition, the near-

solidus effects reported by Baker et al. (1995) have now been reproduced for a slightly

different peridotite composition at 15 kbar by Robinson et al. (1998).

In order to further address the concerns raised about melt extraction experiments, I

conducted two other types of experiments designed to demonstrate that chemical

communication between melt within an aggregate and the bulk charge is sufficient to

attain equilibrium over the course of an experiment. These are described in detail in the

following chapter (see also Figure 3-2bc) and provide extremely compelling evidence

that charges in this study have achieved equilibrium. They include temperature "half-

reversals," in which temperature is raised part way through a one-stage experiment. The

charges respond to the temperature increase by changing composition so as to be in

agreement with isothermal experiments conducted at the final temperature. The other

type of experiment (referred to as compositional convergence experiments in Chapter 3)

does not involve melt extraction, but melt segregation. Aggregates of vitreous carbon

were pre-impregnated with either an Fe-rich basaltic glass or a rhyolitic glass. A small

chip (tens of micrograms) of one of these aggregates was placed at one end of a depleted

peridotite sample in each of eight experiments conducted at temperatures ranging from

$1275°$ to $1330°C$. In every case the composition of the glass within the vitreous carbon

aggregate converged to within analytical error of the liquid compositional trends. Figure

2-7 illustrates the extreme changes in composition the liquids underwent in terms of

several oxides. The final compositions were approached from opposite directions for

many oxides and in this way demonstrate "reversal" of equilibrium. Note that these

experiments contained no empty pore space at any time. That the results of these

experiments are in excellent agreement with two-stage experiments indicates that the

pressure gradient initially present in the two-stage experiments does not cause any ill

effects if the second stage run duration is sufficient. (A two-stage experiment at $1300°C$

with a second-stage duration of one hour produced a liquid which differed from that

produced by a 115-hour second stage.) One sample (#20, see Chapter 3) contained both a chip of the Fe-rich basalt aggregate and an empty layer of vitreous carbon on opposite ends of the charge. The glasses in both locations matched within analytical error. Thus these experiments demonstrate without doubt that compositions of segregated liquids can change significantly by chemical exchange with the bulk sample over the course of an experiment and converge to the same composition when approached in several different ways. Such demonstrations confirm the reliability of high pressure partial melting experiments that use vitreous carbon and diamond aggregates to isolate small melt fractions.

Figure 2-1. Phase diagram for the simple three-component system Diopside-Albite-

Anorthite at 1 atmosphere, drawn after Figure 1 of Walter and Presnall (1994). Point y

represents a bulk peridotite composition (projected into the simple system) for which

liquid coexists in equilibrium with diopside and plagioclase. The compositions of these

phases at 1225°C are fixed and are indicated by the apices of the three-phase triangle

drawn in the figure, including point l, which represents the liquid composition. Point x

represents a bulk composition within the three-phase triangle with the same phase

assemblage and same phase compositions as point y, but a higher proportion of liquid.

Diopside

y

l

x

Albite   plagioclase   Anorthite
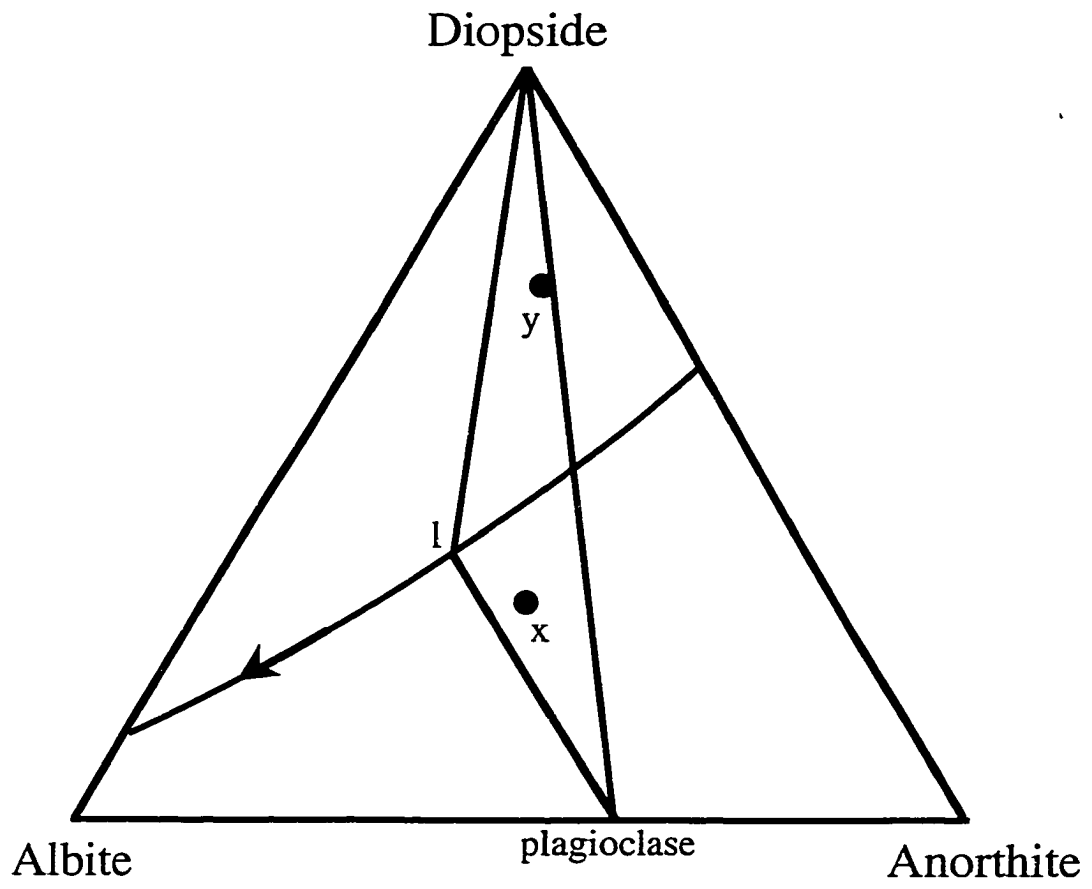
Figure 2-2. Capsule configuration for diamond aggregate experiments. The capsule is about 4 mm wide. Approximately 5 mg of powdered peridotite is loaded with a layer of fine-grained (typically 40-60 micron) diamonds.

Diamonds

Peridotite

Graphite
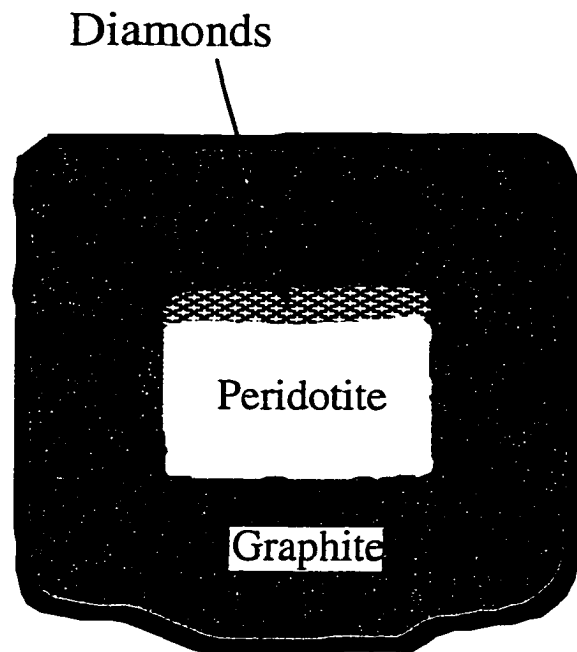
Figure 2-3. Backscattered electron photomicrograph of sample DMM1-01, a typical two-stage charge. Vitreous carbon spheres and glass rinds are indicated by arrows.

100μm 180X
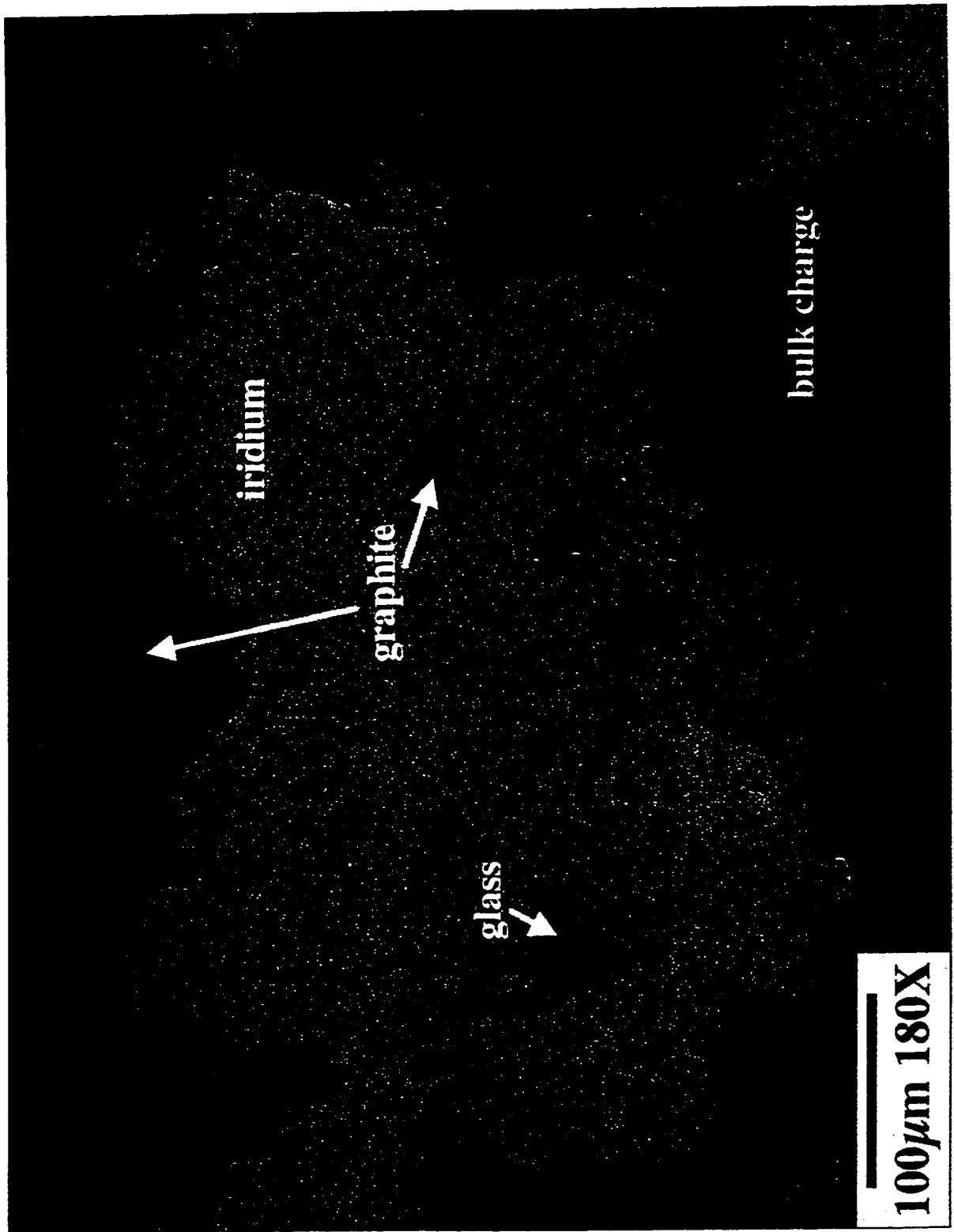
Figure 2-4. Backscattered electron photomicrograph of sample Ir-07, an attempt at using

aggregates of powdered iridium metal to extract melt. Some pore spaces within the

iridium are filled with glass, others with graphite. Note that glass pools appear in cross

section not to be connected by melt tubules to the bulk sample.
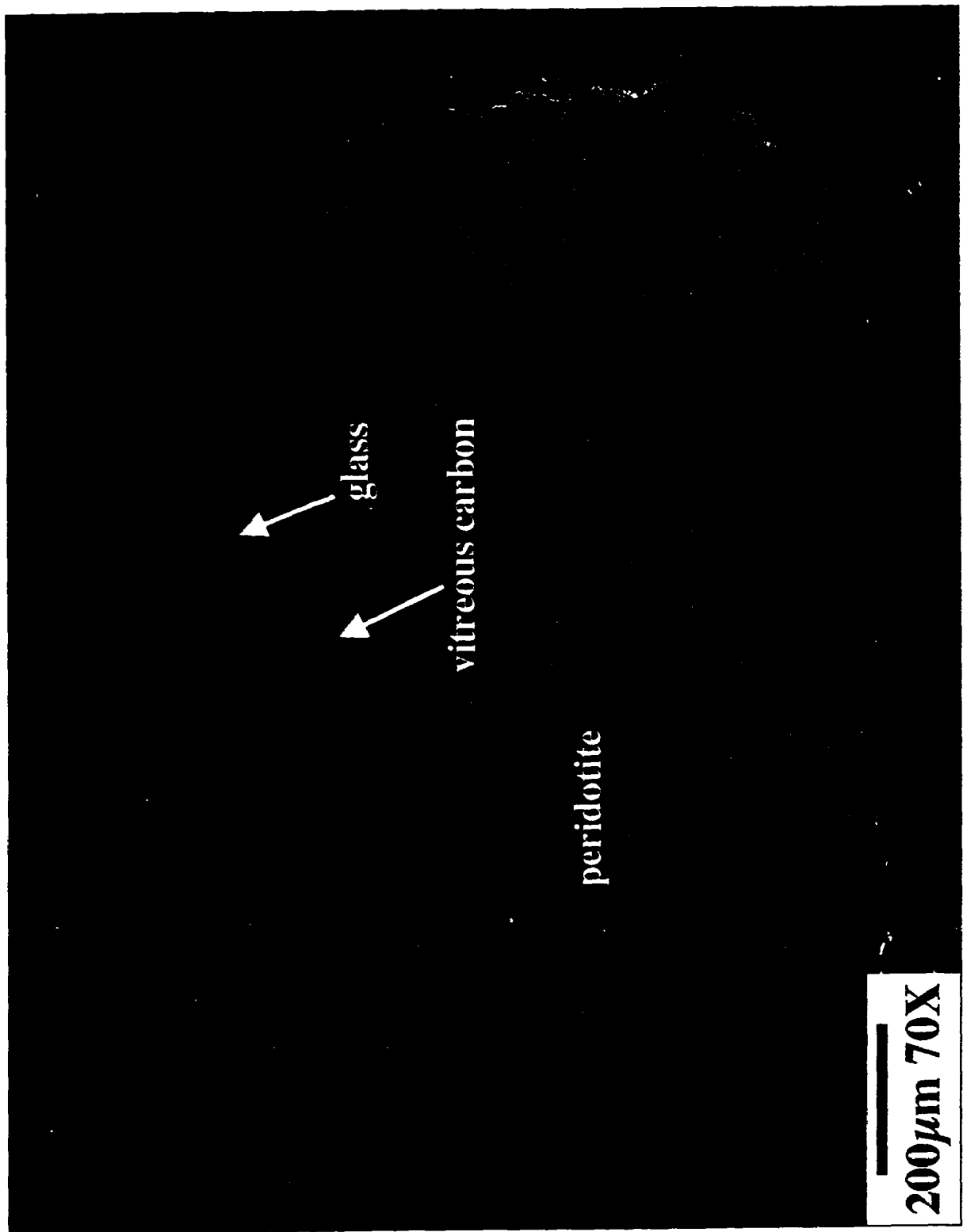
Figure 2-5. Backscattered electron photomicrograph of sample DMM1-49. This charge

was run at 20 kbar and 1390°C for 46 hours. The vitreous carbon has entirely crystallized

to graphite and trapped melt inside. The melt does not appear in cross section to be

connected to the bulk charge, and analyses of the melt pools indicate significant

inhomogeneity, suggesting that different pools of melt became isolated from the bulk

charge at different times during the experiment. The largest sphere is approximately 100

microns in diameter.

graphite after
vitreous carbon

glass

peridotite
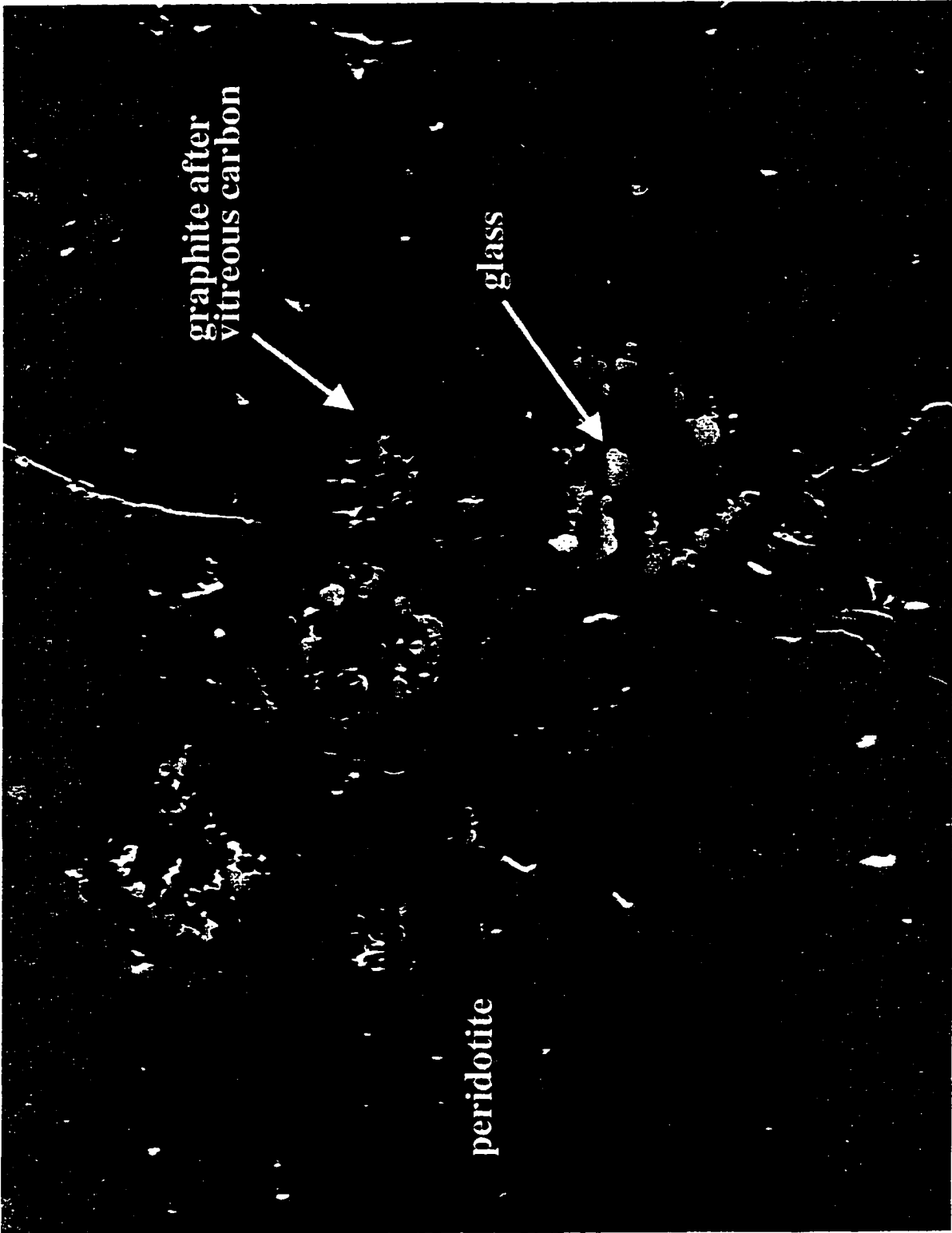
Figure 2-6. Backscattered electron photomicrograph of the aggregate chip in sample

DMM1-28. The vitreous carbon particles are fractured, and melt has filled the cracks. A

crystal is visible in the lower center of the image, but most of the glass is crystal-free.

This glass began as a ferrobasaltic glass with ~12 wt% FeO* (all Fe calculated as FeO),

but now contains 7.54 wt % FeO* and agrees with two-stage, temperature reversal, and

other compositional convergence experiments at this temperature.
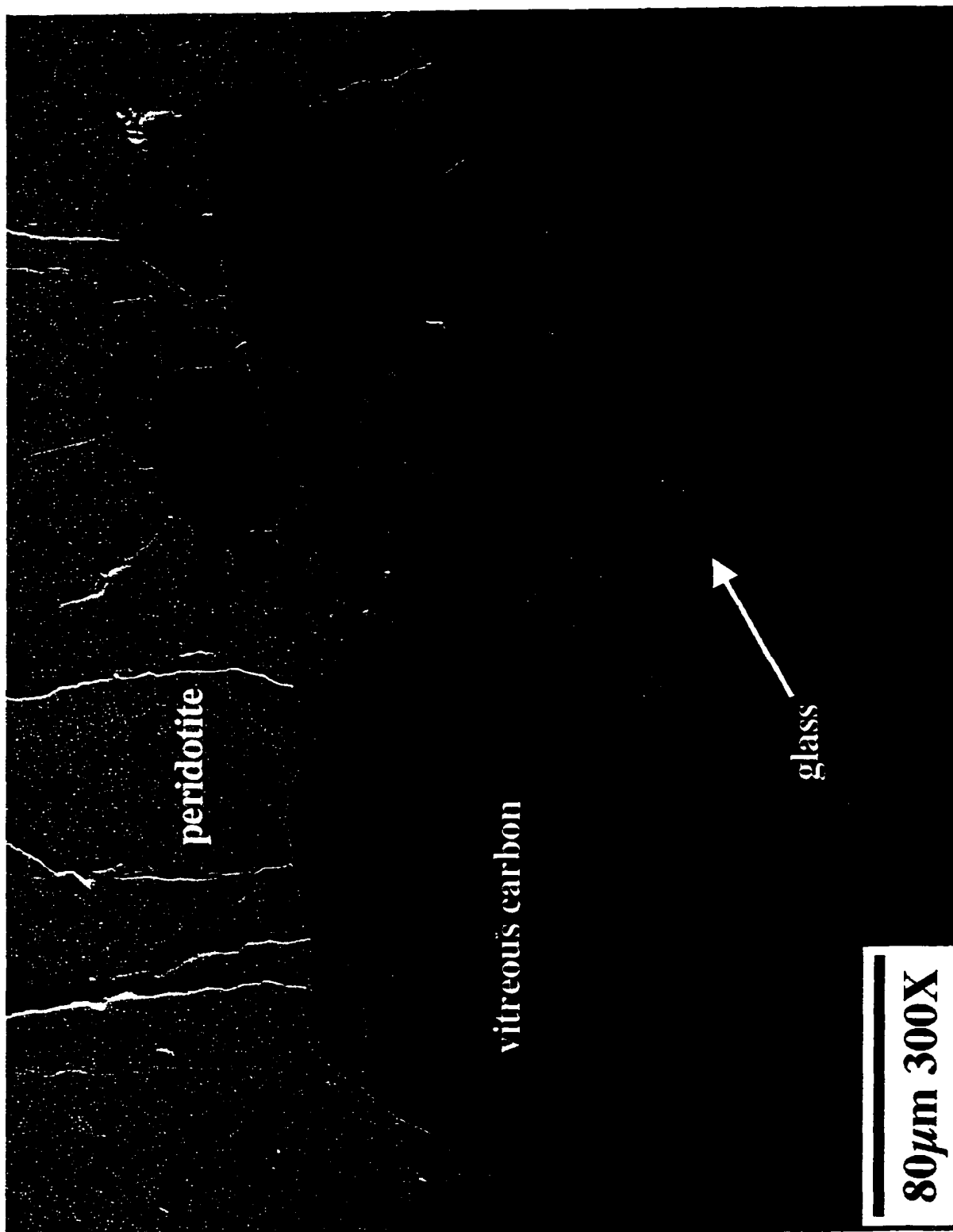
Figure 2-7. Results of compositional convergence experiments. The shaded square represents the initial composition of the ferrobasaltic glass, and the shaded circle shows the initial composition of the rhyolite. Filled diamonds represent liquids coexisting with olivine, orthopyroxene, clinopyroxene, and spinel. Open diamonds are liquids coexisting with olivine and orthopyroxene. Arrows indicate change in composition, which is extreme for some oxides. The glass compositions converged from opposite directions in terms of several oxides.
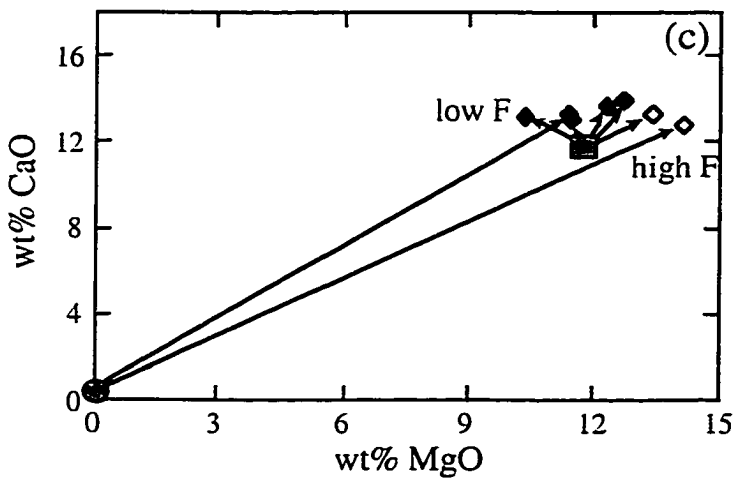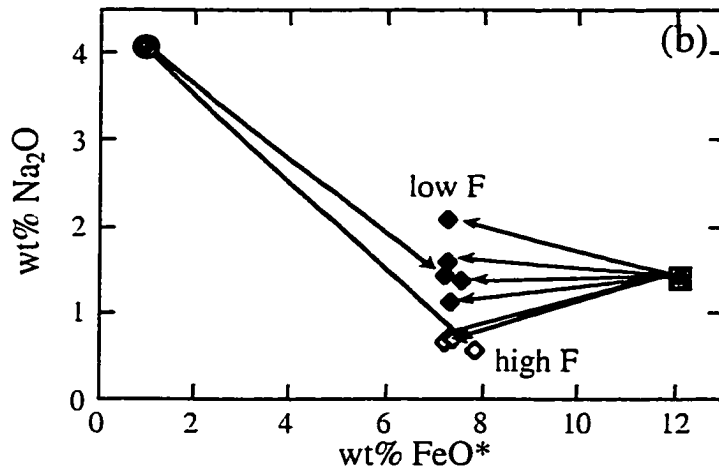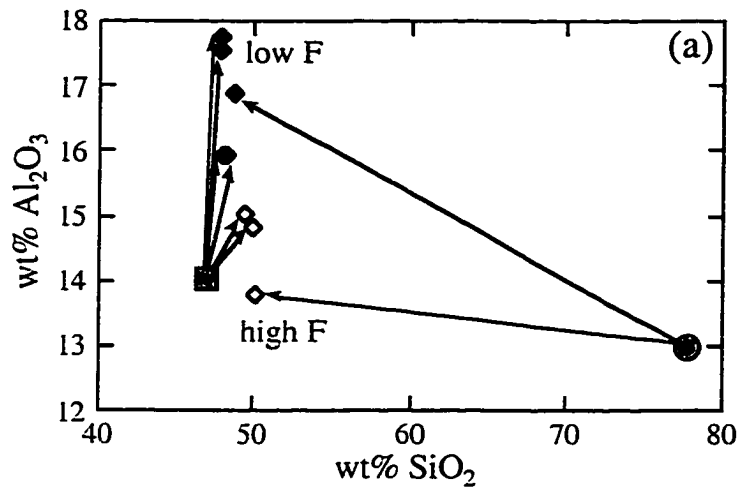
Chapter 3: Partial melting of depleted peridotite at ten kilobars pressure: experimental results

Introduction

In this chapter I present the results of melting experiments on a depleted peridotite composition (DMM1) at ten kilobars and temperatures from 1250° to 1390°C. Although in nature generation of basaltic magmas from partial melting of peridotite is believed to occur by near-fractional fusion over a range of pressures, my experiments represent equilibrium (batch) melting at a single pressure. This is an unfortunate necessity because fractional melting experiments cannot be carried out in any practical way and because most experimental studies in igneous petrology rely on achievement of equilibrium to ensure that results from experiments done on laboratory size and time scales are applicable to processes taking place in the mantle over long periods of time. Thus, while the information provided by experimental studies of partial melting is critical for characterizing primary basaltic liquids, application of experimental data to petrogenesis of magmas is not straightforward and must be done through quantitative modeling of fractional melting processes. Ideally such models of peridotite melting would be calibrated with a large amount of high-quality experimental data over the entire range of relevant compositions, temperatures, pressures, and oxygen fugacities, but the range of compositions and conditions that has been well-studied is limited. This is especially true at low melt fractions, which are most important for investigations of near-fractional melting processes.

Melting of depleted peridotite in particular has seldom been addressed previously: Sen (1982) presented a limited study of batch melting of depleted peridotite at 9 kbar. Jaques and Green (1980), Falloon et al. (1988), and Robinson et al. (1998) reported experimental results on melting of Tinaquillo lherzolite (or Tinaquillo lherzolite - 40%

olivine), which is slightly depleted, but not significantly different from the fertile peridotite compositions studied in the bulk of the experimental mantle melting literature. This study concerns partial melting of a substantially depleted peridotite composition (DMM1). The pressure (10 kbar) was chosen because the DMM1 composition is extremely likely to be relevant to partial melting at that pressure in the upper mantle beneath mid-ocean ridges (see Chapter 4) and in order to facilitate comparison of the results to those of published studies on fertile peridotite also done at 10 kbar. The melt extraction technique has enabled me to examine the products of very low degrees of melting (<10%), in keeping with the objective of this project, which is to provide information about depleted peridotite melting that can be incorporated into models of near-fractional melting in the mantle. I present partial melt and crystal compositions for all of my experiments and use these data to evaluate compositional trends, melt productivity, and melting reactions for a depleted peridotite composition.

Experimental and analytical techniques

Starting materials

Starting material for this study was prepared by mixing mineral separates from a Kilbourne Hole spinel lherzolite nodule (KBH), olivine from a Hawaiian dunite nodule, and synthetic diopside ($CaMgSi_2O_6$). Electron microprobe analyses of the natural minerals are reported in Table 3-1. The crystallinity of the diopside was verified by X-ray diffraction. Minerals were hand-picked from the disaggregated nodule, ground and sieved to 16-28 mesh, cleaned in warm 2.4 N hydrochloric acid, and rinsed in deionized water. They were then crushed to 200-325 mesh size, and again washed in 2.4 N HCl, and deionized water. Finally, the grains were ground and sieved to ≤13 microns. The diopside grains were typically <15 microns, but some grains were as large as 40 microns. The mineral separates were mixed in the proportions 0.432 KBH olivine, 0.202 Hawaiian

olivine, 0.274 KBH orthopyroxene, 0.014 KBH clinopyroxene, 0.060 diopside, and 0.018

KBH spinel by weight to form the depleted peridotite starting material (DMM1). The

mixture was ground by hand for 1 hour under ethanol to ensure homogeneity. The bulk

composition of DMM1 is reported in Table 3-1.

The starting composition (DMM1) was chosen to represent moderately depleted

mantle peridotite. It contains ~42 wt% MgO and lies roughly in the middle of MgO-

oxide trends defined by a large number of reconstructed abyssal peridotite compositions

(Dick, 1989), mantle nodule compositions (Herzberg et al., 1988), and estimates of

primitive mantle composition (Ringwood, 1979; Hart and Zindler, 1986; McDonough

and Frey, 1989). Figure 3-1 compares the concentrations of Na_2O, Al_2O_3, and CaO in

DMM1 and several other experimentally-studied peridotite compositions to estimates of

primitive mantle and calculated abyssal peridotite compositions. The DMM1

composition is significantly depleted in incompatible elements relative to other

compositions that have been used as starting materials in high-pressure experiments,

except for the composition studied by Sen (1982), which is similar to DMM1 in terms of

Na_2O and CaO. When compared to the residues in the 10 kilobar melting experiments of

Baker and Stolper (1994) and Baker et al. (1995), DMM1 is roughly equivalent to the

residue formed by 12-13% batch melting of mm3.

Experimental methods

This study includes three types of melting experiments described in detail below. All

experiments were run in a 1.27 cm piston cylinder apparatus using CaF_2 cells, straight-

walled graphite furnaces and inner pieces of crushable MgO, dried at 1000°C for at least

8 hours. Pressure was applied using the hot-piston-in technique with no friction

correction. Experiments at 1300°C bracketed the Ca-Tschermak breakdown reaction to

lie between 11 and 14 kbar, very close to the experimentally determined value of 13 kbar

at this same temperature (Hays, 1966). $W_{97}Re_3/W_{75}Re_{25}$ thermocouples were used to monitor and control temperature to within ~1°C of the set-point. No emf pressure correction was applied, and temperatures are believed to be accurate to within ±15°C. Run temperatures and durations are reported in Table 3-2. Except in experiments #1, #2, and #3, nitrogen gas was bled into the slot in the thermocouple plate during each experiment to prevent air from migrating down the holes in the thermocouple ceramic and oxidizing the thermocouple wires. At the end of each experiment, the thermocouple wires near the steel base plug were inspected for signs of oxidation; no evidence of significant oxidation was observed on any of the wires. When quenched, samples cooled to below 200°C within several seconds. Each capsule was sliced vertically with a diamond wafering blade, mounted in epoxy and polished for electron microprobe analysis.

The first of the three types of experiments consisted of two stages (see Figure 3-2). For the first stage, 3 to 6 mg of peridotite powder, which had been dried in a vacuum oven at 110°C for a minimum of 2 hours, was loaded into a graphite inner capsule and a 0.15" O.D. platinum outer capsule (Figure 3-2a). The capsule was coned, dried, and then welded shut. The drying procedure varied quite a bit over the course of this study; details are given in Table 3-2. After drying and welding, the capsules were run at temperature and pressure for 52 to 136 hours. For the second stage, each silicate charge was removed from the first-stage capsule and loaded in a new graphite and Pt capsule with a small amount of 80-100 micron diameter vitreous carbon spheres (Figure 3-2b) which had been dried for at least one hour in a 110°C vacuum oven. The mass of vitreous carbon ranged from 2.9% to 9.2% of the mass of the silicate sample and averaged 5.6% (Table 3-2). After drying and welding as above, each sample was then re-run at the same temperature and pressure for 18-135 hours. With the exception of run #21, which was

coarsely ground, all of the first stage peridotite samples were loaded into the second stage

capsules as one-piece plugs.

I also conducted half-temperature reversals (indicated with the letter "R" in Table 3-

2). Dried peridotite powder was loaded into capsules with small amounts of vitreous

carbon spheres (as in Figure 3-2b, but with peridotite in powdered form). As above,

loaded capsules were dried before being welded shut, as described in Table 3-2. Each

sample was run at 10 kbar and an initial temperature as listed in Table 3-2 for 25.5 to

68.4 hours. Following this initial period, the temperature was raised either 15, 30 or

40°C, and the charge was held at this higher temperature for an additional 88 to 117

hours. Initial and final temperatures and run durations at each temperature are given in

Table 3-2. At the end of both the two-stage and temperature reversal experiments, the

charges contained quenched glass within the vitreous carbon region. The glass formed

rinds a few microns thick around the vitreous carbon spheres and occasionally filled

spaces between three or more close-packed carbon spheres (see Figure 2-4).

For the third type of experiment, glass-bearing vitreous carbon aggregates were

prepared in advance by mixing either a powdered oxide mix of ferrobasaltic composition

(FB) or powdered rhyolitic glass from Glass Buttes, Oregon (GBR), with conchoidally-

fractured, vitreous carbon particles (80-147 microns) and running the mixtures in

platinum capsules at 10 kbar and 1350°C. In the case of the rhyolite glass, the charge

was 14% glass and 86% vitreous carbon by weight. Proportions were similar for the FB

aggregate. During the course of these preparatory experiments the silicate liquid

completely impregnated the pore-space within the vitreous carbon layer. The

composition of the ferrobasalt within the aggregate was determined by microprobe

analysis, and the composition of Glass Buttes rhyolite is taken from Ihinger (1991). Both

glass compositions are listed in Table 3-1. Very small pieces (9.8 to 41 micrograms, see

Table 3-2) of these aggregates were loaded into graphite/Pt capsules with DMM1 powder

as shown schematically in Figure 3-2c. The samples were run for 120.0 to 166.0 hours (see Table 3-2; these experiments are marked with a "C"). In one experiment (#20), vitreous carbon spheres were also loaded into the capsule, on the opposite side of the charge from the glass-bearing, vitreous carbon chip.

Oxygen fugacity was not controlled, but the presence of graphite inner capsules constrains fO_2 to below the graphite-C-O vapor buffer. Since coexisting olivine (ol), orthopyroxene (opx), and Fe-Pt alloy can be used to measure fO_2 precisely (Bertka and Holloway, 1988; Gudmundsson et al., 1988), I placed 13 micrograms of platinum wire in the middle of the peridotite powder in experiment #25 (1325°C) in order to determine the fO_2 at a temperature roughly in the middle of the full range studied. The full oxygen fugacity calculations are presented in the appendix to this chapter; the results are summarized here. Based on the compositions of the coexisting Fe-Pt alloy, opx, and ol and using the equations and solution models of Jamieson et al. (1992), the log fO_2 in run #25 was –9.21 or ~2.4 log units below the quartz-fayalite-magnetite buffer (QFM) at 10 kbar (Huebner, 1971). A second method (Gudmundsson and Holloway, 1993) with slightly different activity-composition models than used by Jamieson et al. (1992) yielded a log fO_2 of -8.46, or QFM–1.7. This range of fO_2 values is consistent with estimates for the MORB source region (Christie et al., 1986; Green et al., 1987; O'Neill and Wall, 1987; Mattioli and Wood, 1988; Mattioli et al., 1989).

Analytical techniques

Experimental charges were analyzed with the Caltech JEOL 733 electron microprobe using an accelerating voltage of 15 keV. Crystalline phases and Pt alloys were analyzed with a beam current of 30 nA and a spot beam rastered over a 2-3 micron area. Glasses were analyzed with a 5 or 10 nA beam current and a rastered area of generally ~5 x 5 microns. Data were processed using CITZAF (Armstrong, 1988). Two basaltic glasses,

VG-2 and BGIO, were analyzed during each microprobe session in order to estimate accuracy and precision of the instrument on a long-term basis. Mean analyses and 1σ errors for the two glasses over a three and a half year period at glass analysis conditions (121 and 103 analyses, respectively) and at crystal analysis conditions (55 and 64 analyses) are given in Table 3-3. When crystalline run products were analyzed, Johnstown hypersthene (JHYP) and Natural Bridge diopside (DIOP) were used as secondary standards. The long-term averages (103 and 116 analyses, respectively) and 1σ uncertainties for these two phases are also listed in Table 3-3.

Although a few samples had good analytical totals (>98.5%) on glass analyses, raw oxide sums for the experimental glasses were typically between 95 and 98%, and were occasionally lower, down to 89% in one case. Given the very small size of the individual regions of glass, the low totals probably reflect the inclusion of vitreous carbon in the analysis volume. However, when all of the glass analyses for a given sample are normalized to 100%, I see no systematic difference in any oxide as a function of the raw oxide sum. Average experimental glass compositions are reported in Table 3-3. Detailed microprobe analysis of glasses indicates that liquids were homogeneous within each charge. Glass analyses were made both close to and far from the bulk silicate charge wherever possible, and no systematic variations in glass composition as a function of location within the vitreous carbon aggregates were observed. Standard deviations for multiple analyses are also given in Table 3-3, with the numbers of analyses included in each average in parentheses.

Water contents of the glasses in three charges (#3, #11, #22) were measured using the Cameca IMS-3f ion microprobe at Lawrence Livermore National Laboratories with assistance from A. Kent. A voltage of 12.5 kV was used to accelerate a focused beam of oxygen ions with a beam current of 1-2 nA and a primary beam spot size of ~20 microns. A computer-controlled magnet and data acquisition system were used to repeatedly cycle

the magnet between the H+, ^{16}O+, and ^{30}Si+ mass peaks, using count times of 1-5, 1, and 1 seconds, respectively. Low energy secondary ions of H were filtered by using an energy band of 80±30 eV. In order to counter the effect of sample charging, the energy spectrum of secondary oxygen ions was measured every 5-10 spectrometer scans and the energy offset updated. Background levels of water were minimized by use of a liquid nitrogen-cooled "shroud" surrounding the sample mount in the vacuum chamber. Once in the sample chamber, the background was allowed to drop below H+/^{30}Si+ = 0.10 (on crystalline olivine) before measurement began. A 5-10 nA primary beam was rastered over a 100x100 micron area at each analysis point for 3-5 minutes prior to analysis in order to remove surface-adsorbed water. Water contents were calculated from H+/^{30}Si+ ratios using a calibration curve based on ion microprobe, infrared spectroscopy, and electron microprobe analyses of basaltic glasses from the Marianas back arc basin (Stolper and Newman, 1994) and synthetic MORB glasses (Dixon et al., 1995). Errors on the water contents of the experimental glasses are conservatively estimated at ±15% relative. Water contents are reported in Table 3-3. The small size of the glass regions within vitreous carbon aggregates relative to the size of the ion probe beam leads to two sources of uncertainty in these measurements, since the analysis volume likely includes some vitreous carbon. First, the water content of the vitreous carbon is unknown, but may be substantial (Wasylenki, unpublished results), and can be either higher or lower than the water content of the glass. Thus the reported water contents of the glasses may be either higher or lower than the actual water contents. Second, since vitreous carbon contains no Si, the measured H+/Si+ ratio may be low, leading to overestimation of the water concentration in glass.

Results

Attainment of equilibrium

Although the melt extraction technique used for this study provides a simple way to avoid the quench modification problems encountered in conventional equilibrium melting experiments close to the solidus, the technique must be applied with care. The issue of whether the glasses within the vitreous carbon aggregates (or diamond aggregates, as used by others, e.g., Hirose and Kushiro, 1993; Baker and Stolper, 1994; Baker et al., 1995; Kushiro, 1996) actually represent equilibrium compositions has sparked much debate (Baker et al., 1996; Falloon et al., 1996; Falloon et al., 1997), as discussed in Chapter 2. The controversy concerns the likelihood that liquid initially filling vacant pore spaces is not in equilibrium with the bulk peridotite at the nominal pressure of the experiment. The critical issue, therefore, is whether partial melts can approach equilibrium by diffusive communication with the residual solid phases over the course of the experiment. The run duration must be long enough, and the melt tubules which connect the extracted liquid and the partial melt within the crystalline residue must provide adequate connection for diffusion to overcome the initial disequilibrium state. I present several lines of evidence that show that the liquids in the vitreous carbon aggregates have approached equilibrium closely.

I performed two types of experiments especially designed to demonstrate that liquids in the vitreous carbon layers in the two-stage runs can change their compositions during the course of each experiment. In the first case, I conducted three temperature "half-reversals," labeled "R" in Table 3-2. In each such experiment, after initial run durations of 26-68 hours at 1285° or 1310°C, temperatures were increased either 15, 30, or 40°C and the runs continued for an additional 88 to 117 hours. I expect that during the initial stages of these experiments, liquids in the vitreous carbon layers approached compositions similar to those from the two-stage runs at 1285° or 1310°C. The final liquid compositions in the "half-reversal" experiments are different from those produced in the 1285° and 1310°C two-stage runs and correspond to liquids produced in the higher

temperature two-stage runs. Thus over the course of 88 to 117 hours liquid compositions in the vitreous carbon layers changed in response to the increase in temperature. It is important to note that the final melt fractions in these runs range from 4 to 11 wt%, thus re-equilibration can occur even when the proportion of liquid in the charge is low. I attempted to complete the temperature reversals by lowering the temperature in some experiments, but, as one might expect, this resulted in rather extensive crystallization within the vitreous carbon aggregate.

My "convergence" experiments, labeled "C" in Table 3-2, demonstrate that the liquids in the vitreous carbon layer can change substantially in composition even at temperatures very close to the DMM1 solidus. As described above, these experiments involved placing a very small piece of a vitreous carbon aggregate that had been impregnated with either an Fe-rich, Na-rich basaltic glass or a rhyolite glass in a capsule with DMM1. The very small amount of glass (a few micrograms) added to the system has little or no effect on the bulk composition. For example, the bulk Na_2O content in run #34C is increased from ~0.06 to ~0.07wt% by the addition of the rhyolite-bearing chip. Based on the results of the two-stage experiments, both glass compositions are initially far from equilibrium with DMM1 at 10 kbar and any temperature. At the end of each micro-sandwich experiment, however, the quenched liquid in each vitreous carbon chip has converged to the compositional trend defined by all of the two-stage experiments. Figure 3-3 illustrates the large shifts in composition that these glasses underwent due to diffusive equilibration. It is important to note that the compositions of the liquids in the vitreous carbon chips in these experiments have converged to their final compositions from opposite directions in terms of several oxides. The synthetic ferrobasalt, FB, is low in SiO_2, but high in FeO*, MgO, CaO, TiO_2, and Cr_2O_3, while Glass Buttes rhyolite is extremely high in SiO_2 and alkalis, but quite low in MgO, CaO, Cr_2O_3, and FeO* relative to the final glass compositions in my experiments. Convergence experiments

were successful even very near the solidus of DMM1; three of the convergence

experiments have melt fractions of ~2 to 4 wt%. Note that in these experiments there is

never any open pore space within the vitreous carbon layer and thus no pressure gradient

exists when the charge is first brought to run conditions. That these liquids converge to

compositions that are similar to those produced in the two-stage experiments suggests

that the long run times of the two-stage experiments have allowed initial disequilibrium

liquids to diffusively re-equilibrate with the residual peridotite. One of the experiments,

#20, contained both a chip pre-impregnated with FB basalt and a layer of vitreous carbon

spheres at the opposite end of the charge. The layer of spheres initially contained empty

pore space, as in the one- and two-stage experiments described above. Averages for glass

within both vitreous carbon aggregates are included in Table 3-3 and are well within 2σ

of each other for each oxide (nearly all are within 1σ). Thus initial pore space within

charges does not seem to cause any ill effects for aggregate extraction experiments.

In addition to the experimental tests, I have also carefully examined the compositional

heterogeneity of the residual peridotite minerals in all of the experiments, since

achievement of equilibrium would require homogeneous crystals and no dependence of

mineral composition on distance from either vitreous carbon layers or glass-bearing

chips. In all experiments ol grains were homogeneous within analytical error in each

charge, both from core to rim of individual analyzed grains and from top to bottom of the

residual peridotite.

Orthopyroxene grains with cross-sectional diameters larger than 10 microns often

displayed small, unreacted cores, visible with high gain backscattered electron imaging,

intermediate zones of reacted pyroxene (hereafter referred to as rims), and very thin (<1

micron) outer layers of quench overgrowth. The unreacted cores in all cases comprise

less than 50% (in most cases much less) of the area of the opx grains viewed in the

polished cross section. They therefore occupy a maximum of about 35% (probably much

less) of the volume of opx in the charges. In general, the cores matched the rims in terms of MgO and FeO* content, but cores have higher Al_2O_3 and lower CaO contents. Analyses reported in Table 3-3 are averages of rim analyses. Analyses included in the averages were carefully selected from a large number of analyses in order to exclude those associated with quench growth, which were identified by anomalously low CaO/Al_2O_3 ratios and/or high MgO concentrations or those which included unreacted core material (low CaO/Al_2O_3) within the analysis volume. Opx in experiment #22 appears not to have approached equilibrium as closely as in other charges. Al_2O_3 contents are low relative to the trend defined by opx in other samples. I did not observe any significant differences in opx composition as a function of distance from the vitreous carbon aggregates in any of the experimental charges.

Unreacted cores were not visible in clinopyroxene (cpx) grains, which were typically quite small (<15 microns) or occurred in sinuous, anastomosing forms. Microprobe analyses, however, do indicate that the grains are not homogeneous. In particular, CaO and Al_2O_3 contents vary among the cpx analyses in each charge. As noted by Robinson et al. (1998), cores tend to have lower MgO, higher Al_2O_3, and higher CaO contents than rims. As for opx, a large number of cpx analyses were collected from each charge so that those which clustered toward the low-Al and low-Ca end of the trend in Al_2O_3-CaO-MgO space defined by all analyses could be chosen for averaging in Table 3-3. Again sample #22 has anomalous pyroxene compositions; Al_2O_3 contents in cpx are higher than expected based on the other samples. Variations in cpx composition as a function of distance from the vitreous carbon layer generally were not noted. In a few capsules, however, cpx modal abundance did vary from top to bottom, most likely due to thermal gradients across the capsules during the runs.

Spinel (sp), which occurs in trace amounts below 1310°, is the only phase that did not consistently approach equilibrium compositions. This is most likely due to the slow

diffusion of Al and Cr in spinel (Dieckmann et al., 1978). Spinel grains are extremely small in these experiments (<10 microns in diameter), and only a few spinels are present in each charge. Thus it is not possible to assess the degree of compositional variation within individual spinel grains or as a function of the position of the spinels in the charge. Given the small amount of spinel that is present in even the lowest temperature experiment, disequilibrium spinel compositions should not significantly affect the results.

The observations above strongly indicate that my experimental charges have approached equilibrium closely. In particular the temperature reversals and micro-sandwich experiments clearly show that liquids within vitreous carbon aggregates can reach equilibrium compositions even when equilibrium is approached from different directions in temperature and composition space. Thus the melt extraction technique has been shown to yield valid results from which low degree partial melting behavior of many different source compositions can be characterized.

Phase relations and liquid compositions

I have conducted experiments over the temperature range of 1250 to 1390°C. Partial melt coexists with olivine, orthopyroxene, clinopyroxene, and spinel at temperatures between 1270° and 1300°C. Runs between 1310° and 1390°C contain liquid, olivine, and orthopyroxene, with the exception of experiment #23R (nominally 1325°C), which contains a trace amount of cpx. I interpret these results as indicating that cpx-out and sp-out occur over the temperature interval 1300°-1310°C. The small amount of cpx in run #23R may reflect a deviation from nominal temperature larger than the stated ±15°C error or a failure of the last few cpx nuclei to disappear from the residue. High magnification back-scattered electron images of the 1250°C charge did not appear to contain any indication of glass. Although such determinations are difficult, I tentatively place the solidus for DMM1 between 1250° and 1270°C.

Figure 3-4 shows how selected oxides from my 10 kbar partial melts vary as a

function of liquid MgO content. MgO contents in peridotite partial melts correlate

positively with temperature (e.g., Jaques and Green, 1980; Hirose and Kushiro, 1993;

Baker and Stolper, 1994; Walter, 1998), and I have used MgO as a proxy for temperature

because the oxide-MgO trends are smoother than oxide-temperature variations, due to the

uncertainties associated with the thermocouples. Some of the experiments are nominally

only 5-10°C apart. Based on glass compositions, however, actual temperature differences

were in some cases apparently larger. The plotted glass compositions include results

from two-stage experiments, temperature-reversal runs, and convergence experiments.

Glass compositions vary from basaltic (~10-11 wt% MgO at the lowest temperatures,

1270-1275°C) to picritic (16.5 wt% MgO at 1390°C). Over the entire range of MgO

contents, SiO_2, Cr_2O_3 and FeO* contents all increase monotonically with increasing

MgO (Figure 3-4ade). Silica varies from ~48 to nearly 51 wt% (Figure 3-4a), while

FeO* contents range from ~7.2 to 8.4 wt% (Figure 3-4e). TiO_2, Al_2O_3, and Na_2O

abundances decrease with increasing MgO (Figure 3-4bcg); alumina varies from ~17.5 to

nearly 12 wt%, while Na_2O contents drop from between 1.5 and 2 wt% close to the

solidus to values between 0.3 and 0.4 wt% at the highest temperatures investigated. CaO

contents show a slight concave-downward pattern (Figure 3-4f); abundances increase

slightly with increasing magnesium content to cpx-out at ~13 wt% MgO, and then CaO

contents drop to a value of ~10.6 at 16.6 wt% MgO (at 1390°C). With the exceptions of

SiO_2 and TiO_2, the trends displayed by the other major and minor elements are

qualitatively similar to those produced in near-solidus melting experiments on fertile

mantle compositions at 10 and 15 kbar (Hirose and Kushiro, 1993; Baker and Stolper,

1994; Baker et al., 1995; Kushiro, 1996; Robinson et al., 1998; Hirschmann et al., 1998a;

note Robinson et al. used a modified sandwich technique and not a diamond aggregate

approach). I will return to a more detailed comparison between 10 kbar depleted and fertile peridotite melting trends in Chapter 4.

Two experiments reported in the tables have not been included in the figures or discussion. The glass in experiment #21 has apparently suffered iron loss, as indicated by the low FeO* content of the glass and olivine, very high $K_{D,Fe^*-Mg,ol-liq}$ value ($K_{D,Fe^*-Mg,ol-liq}$=[FeO*ol/FeO*liq]/[MgOol/MgOliq]), and anomalously high SiO_2 content (Falloon and Green, 1987). The glass in experiment #11 also has high SiO_2 and low FeO* and does not fit the trends defined by the other experiments. The value of $K_{D,Fe^*-Mg,ol-liq}$ is not anomalous (0.33), and analysis of the Pt capsule indicates no alloyed Fe, but iron loss may have occurred during the first stage of the experiment. This glass also contains almost 1 wt% H_2O, as determined by ion probe measurement of $H^+/^{30}Si^+$, which may cause slight elevation of $SiO_2/(MgO+FeO)$ (Gaetani and Grove, 1998). In addition, the glass-rimmed vitreous carbon spheres in this charge appear to be quite far away from the bulk silicate charge, suggesting that chemical communication between the extracted glass and bulk charge may have been compromised.

Solid phase compositions

The compositions of crystalline phases also change systematically over the range of investigated temperatures. The Mg# (100Mg/[Mg+Fe], molar) of olivine increases from ~89.8 to 90.8 with increasing liquid MgO content. The average value of $K_{D,Fe^*-Mg,ol-liq}$ for the data set is 0.34, and the range is from 0.28 to 0.36. K_D shows a slight positive correlation with temperature (or liquid MgO content), as shown in Figure 3-5, possibly due to the negative correlation between liquid alkali content and K_D as described in Baker et al. (1995) and Hirschmann et al. (1998a). These data are consistent with prior 10 kbar experimental results on low-alkali liquids (Ulmer, 1989; Baker and Stolper, 1994).

Orthopyroxene compositions vary systematically as a function of run temperature. For the vast majority of cpx-bearing experiments, CaO concentrations in orthopyroxene are nearly constant at ~2.2 wt% (a Wo# of ~4.2; Wo#=Ca/(Ca+Mg+Fe), molar, see Figure 3-6b); following cpx-out, CaO contents drop rapidly and reach a value of 1.3 wt% at 1390°C (Wo# of ~2.5). The average rim composition of orthopyroxenes in run #22 is 1.7 wt% CaO, slightly below the value of 2.2 wt% found in the other cpx-bearing experiments. $D_{Ca}^{opx/liq}$ (CaO in opx/CaO in glass, wt%) is ~0.17 in the cpx-saturated experiments. With increasing temperature and the loss of cpx from the residual assemblage, $D_{Ca}^{opx/liq}$ begins to drop and reaches a value of ~0.12 in the 1390°C experiment. Al_2O_3 contents in the orthopyroxenes decrease with increasing temperature, varying from ~5 wt% at 1275°C to 1.8 wt% at 1390°C. Since liquid Al_2O_3 contents are also inversely correlated with run temperature, $D_{Al}^{opx/liq}$ is nearly independent of temperature; values for all my experiments lie in the range 0.13 to 0.18. $D_{Cr}^{opx/liq}$ drops from ~8 at 1270° to ~5 at 1290°, then gradually drops to ~2 at 1390°. Values of $D_{Na}^{opx/liq}$ appear to be independent of temperature and range from 0.02-0.04 for all experiments except #9 at 1390°, which has $D_{Na}^{opx/liq}$ =0.08. $D_{Ti}^{opx/liq}$ shows significant scatter due to the very small amount of TiO_2 in opx, but $D_{Ti}^{opx/liq}$ appears roughly constant with temperature, averaging ~0.1.

The CaO content of cpx drops slightly from ~18 to 16.82 wt% as temperature increases from 1270° to 1300°C (this corresponds to a drop in Wo# from ~38 to ~36, see Figure 3-6a). This decrease and the nearly constant CaO content in opx are consistent with previous results at 10 kbar on the enstatite-diopside join (Lindsley, 1980); CaO content in cpx coexisting with opx decreases with increasing temperature, while CaO in opx rises very slightly in the simple system. D_{Ca} in cpx drops slightly from 1.36 to 1.26. Al_2O_3 also shows significant scatter, but when viewed as a function of melt fraction, it is clearly decreasing gradually with increasing degree of melting from ~6 to ~5 wt%, with

one anomalous value of 6.27% at 1300° in experiment #22, mentioned above for poorly-equilibrated opx grains. Cr_2O_3 content is roughly constant, with a range from 0.97 to 1.20 wt%. $D_{Cr\,cpx-liq}$ decreases nearly linearly with increasing temperature from 10.76 at 1270° to 5.45 at 1300°. Na_2O content ranges from 0.14 to 0.31 wt% and does not show a strong correlation with temperature. $D_{Na\,cpx-liq}$ gradually increases from ~0.1 to 0.15, although experiment #34 has an anomalous value of 0.22. $D_{Ti\,cpx-liq}$ ranges from 0.14 to 0.30, with a weak suggestion of a positive correlation between temperature and D_{Ti}.

As mentioned above, analyses indicate that spinel grains did not reach equilibrium compositions in some experiments; some charges contain only Cr-rich spinels, some only Al-rich spinels, and some contain a range of compositions with regard to Cr and Al. The Kilbourne Hole spinel in the starting material had an Mg# of 78.3 and a Cr# (Cr/[Cr+Al], molar) of 13.7. Coexisting olivine has an Mg# of 90.6. According to the theoretical and experimental constraints on temperature-dependent exchange equilibria between olivine and spinel examined by Irvine (1965) and Engi (1983), the Kilbourne Hole spinel and olivine last equilibrated with each other at ~900°C. The Mg-Fe and Cr-Al partitioning must adjust in response to the much higher temperatures in the present experiments. There is an expected negative correlation between Mg# and Cr# in spinel. The analyzed spinel grains exhibit a strong such correlation, but neither parameter is correlated with temperature, although it is expected that Mg# will decrease and Cr# increase with increasing temperature. Because of the large proportion of olivine in the charges relative to spinel, it is expected that Mg# of spinel will be controlled by olivine Fo#, but this does not appear to be the case in these experiments, indicating that spinel grains did not equilibrate with other crystalline phases. Fortunately, because the proportion of spinel is very small in all experiments, the lack of equilibration does not cause difficulty in interpretation of these experimental results. The only components likely to be

significantly affected are Cr_2O_3 and Al_2O_3, 43% and 17% of which are hosted by spinel in the lowest temperature experiment.

Phase proportions, melt productivity, and melting reactions

I have calculated phase proportions in each of the experiments using the compositions of the coexisting phases, the bulk composition of DMM1, and the mass balance expressions of Albarède and Provost (1977). Liquid fractions in the two-stage experiments vary from ~0.02 at 1275°C to ~0.17 at 1390°C. At the same temperature, calculated liquid fractions in the half temperature-reversal and micro-sandwich experiments are in general agreement with those calculated for the two-stage runs. Figure 3-7a shows melt fractions plotted as a function of temperature. Although somewhat scattered, projecting the spinel-lherzolite saturated liquid fractions down temperature suggests a solidus temperature of 1260-1265°C. This agrees with my experimental bracket of 1250-1270°C (based on visual inspection of high-magnification SEM images, the 1250°C run appeared not to contain glass). Between the solidus and cpx+sp-out (~1310°C), melt productivity is fairly high (0.11%/°C), but drops to a lower value (0.07%/°C) with the disappearance of cpx and sp. This change in melt productivity with decreasing variance of the system is consistent with thermodynamic evaluations of peridotite melting (Hess, 1992; Asimow et al., 1997). Figure 3-7b shows melt fraction as a function of glass MgO content.

The melting experiments on DMM1 provide both qualitative and quantitative information on the melting reactions in both the spinel lherzolite and harzburgite fields. Projecting the liquid and three silicate phases from normative Spinel onto the pseudoternary Olivine-Clinopyroxene-Quartz (see Baker and Stolper, 1994, for projection coordinates) illustrates that while the solid residue contains a spinel lherzolite assemblage, DMM1 melts via the reaction opx+cpx+sp = liquid+ol. The chemographic

relationships are qualitatively similar to those shown in Kinzler and Grove (1992a) and

Baker and Stolper (1994). My results coupled with those from Kinzler and Grove

(1992a) and Baker and Stolper (1994) on more fertile bulk compositions suggest that the

peritectic-like reaction opx+cpx+sp = liquid+ol is insensitive to bulk composition at 10

kbar. Figure 3-8 shows residual phase proportions plotted as a function of melt fraction.

The lines fit to the spinel lherzolite and harzburgite residues are unweighted least-squares

fits, and, as discussed by Baker and Stolper (1994) and Walter et al. (1995), the slopes of

these lines represent the melting reaction coefficients. In the spinel lherzolite field, the

resulting equation is: 0.57 opx + 0.72 cpx + 0.04 sp = 0.35 ol + 1 liquid, while at

temperatures above cpx+sp-out, DMM1 melts via the reaction 1.25 opx = 0.25 ol + 1

liquid.

In the following chapter, I will compare these results to experimental data on partial

melting of fertile peridotite, emphasizing important differences in the compositions and

amounts of liquid generated from depleted and fertile peridotite at ten kilobars and the

likely causes of these differences. I will quantify the effects of bulk composition on the

10 kbar peridotite solidus, near-solidus melt productivity, and melt fraction at exhaustion

of cpx from the residue. My experimental results will also be compared to calculated

partial melt compositions using three prominent mantle melting models from the current

literature (Kinzler and Grove, 1992a; Langmuir et al., 1992; Ghiorso and Sack, 1995). I

have used two of these models to estimate at what pressures peridotite such as that

studied here is relevant during polybaric, fractional melting beneath mid-ocean ridges. I

also present estimates of the proportion of liquid contributed by depleted peridotite to

primary MORB magmas, further illustrating the importance of depleted peridotite to

MORB petrogenesis.

Table 1. Starting material compositions†.

	SiO₂	TiO₂	Al₂O₃	Cr₂O₃	FeO*	MnO	MgO	CaO	Na₂O	K₂O	NiO	Mg#
KBH ol(10)§	40.76(16)	-	0.01(1)	0.01(1)	9.34(10)	0.12(2)	49.49(21)	0.07(1)	-	-	0.39(2)	90.4(5)
H1801 ol(14)††	40.40(17)	-	0.01(1)	0.02(2)	12.07(71)	0.17(2)	47.55(55)	0.16(2)	-	-	0.39(4)	87.5(15)
KBH opx(8)§	54.99(22)	0.10(2)	4.76(15)	0.50(4)	5.98(6)	0.13(2)	32.79(14)	0.86(2)	0.12(1)	-	0.11(2)	90.7(5)
KBH cpx(15)§	51.99(21)	0.41(5)	6.56(11)	1.00(5)	2.81(4)	0.09(2)	15.24(10)	19.89(11)	1.58(3)	-	0.04(2)	90.6(8)
Diopside†††	55.49	-	-	-	-	-	18.61	25.89	-	-	-	-
KBH sp(11)§	0.11(2)	0.11(2)	54.91(27)	12.96(20)	10.54(11)	0.10(2)	20.95(10)	-	-	-	0.37(2)	78.0(5)
DMM1*	44.91(11)	0.04(1)	2.38(5)	0.39(1)	8.34(15)	0.13(1)	41.59(15)	2.14(2)	0.055(3)	-	0.28(1)	89.9(5)
FB	46.59(8)	0.41(2)	13.78(5)	0.32(1)	12.07(10)	0.10(2)	11.95(3)	12.06(3)	1.39(2)	-	0.01(1)	63.8(3)
GBR**	77.61	0.06	12.92	-	0.36	0.03	0.04	0.52	4.18	4.17	-	16.5

†Abbreviations: ol=olivine, opx=orthopyroxene, cpx=clinopyroxene, sp=spinel; DMM1=bulk composition used in this study; FB=ferrobasalt, GBR=Glass Buttes rhyolite; Mg#=100*Mg/(Mg+Fe) on a molar basis with all Fe as Fe(II).

Numbers in parentheses adjacent to analyses indicate 1 sigma in terms of the least units cited, e.g., 40.4(1) represents 40.4±0.1.

§Minerals separated from a Kilbourne Hole nodule; number of electron microprobe analyses in parentheses, each analysis on a separate grain.

††Olivine separated from a nodule from Hawaiian 1801 flow.

†††Synthetic crystalline diopside, analyzed by X-ray diffraction.

*Bulk composition calculated from constituent mineral compositions and mixing proportions as given in text. Errors are based on Monte Carlo propagations of errors on phase compositions and estimated weighing errors.

**Composition of Glass Buttes rhyolite taken from Ihinger (1991).

Table 2. Experimental results.

Run#†	Temp(°C)	Drying††	1st stage (hr)	2nd stage (hr)	Silicate(mg)	Glassy carbon(mg)†††	Phases present¶	Phase proportions (wt%)§
9	1390	300/4,300/1	51.7	59.4	5.01	0.175	gl,ol,opx	16.6(6),68.1(15),15.4(16)
30	1370	400/1,400/1	69.5	87.5	4.85	0.196	gl,ol,opx	13.6(5),68.1(17),18.3(17)
1	1350	110/12+,110/3	72.1	18.5	4.17	0.261	gl,ol,opx	12.5(6),67.5(15),20.0(16)
2	1330	110/20,300/2	93.4	37.6	4.32	0.238	gl,ol,opx	10.0(5),67.1(15),22.9(16)
20C	1330	110/12+	141.3	-	3.07	0.435 (FB 33.8)	gl,ol,opx	11.7(4),66.9(15),21.4(15)
26C	1325	450/2	166.0	-	4.38	(GBR 9.8)	gl,ol,opx	12.3(5),66.6(14),21.1(15)
25R	1285/1325	110/12+	30.2/92.8	-	3.02	0.277	gl,ol,opx	10.8(5),66.0(15),23.2(17)
23R	1310/1325	300/1	25.5/87.8	-	3.83	0.198	gl,ol,opx,cpx	8.8(5),66.5(7),23.5(8),1.2(4)
3	1310	110/3,110/12+	93.9	39.1	4.36	0.183	gl,ol,opx	10.3(5),66.8(15),22.9(17)
22	1300	300/1,110/3	116.4	114.7	4.61	0.403	gl,ol,opx,cpx,sp	6.6(8),65.0(16),24.0(17),4.2(7),0.3(2)
17R	1285/1300	300/1	68.4/117.2	-	3.56	0.252	gl,ol,opx,cpx,sp	3.2(8),65.5(15),25.3(17),5.8(7),0.3(1)
12	1290	300/1,300/2	92.9	70.5	2.69	0.078	gl,ol,opx,cpx,sp	6.4(7),66.4(14),23.5(16),3.4(7),0.3(1)
27C	1290	450/2	126.8	-	4.82	(FB 21.6)	gl,ol,opx,cpx,sp	5.4(8),64.1(18),26.3(20),3.7(7),0.5(2)
28C	1290	400/2	141.5	-	4.146	(FB 26.9)	gl,ol,opx,cpx,sp	2.6(7),64.5(15),26.8(16),5.8(8),0.4(2)
21	1285	300/1,300/1	136.5	134.9	3.21	0.19	gl,ol,opx,cpx,sp	
11	1275	300/1,300/1	115.7	63.6	3.98	0.258	gl,ol,opx,cpx,sp	
33C	1275	400/4	161.7	-	3.784	(FB 22.0)	gl,ol,opx,cpx,sp	1.6(3),64.7(13),26.5(14),6.8(5),0.5(2)
34C	1275	400/5	188.5	-	4.737	(GBR 40.6)	gl,ol,opx,cpx,sp	4.0(8),64.7(14),26.0(16),5.0(7),0.3(2)
42C	1270	400/4	184.3	-	5.884	(FB 31.8)	gl,ol,opx,cpx,sp	3.3(6),62.6(16),27.9(17),5.4(5),0.8(2)
36	1250	400/4,400/4	142.0	245.5	9.256	-	ol, opx, cpx, sp	§§62.8(17),28.4(19),8.1(5),0.6(2)

†C indicates convergence test; R indicates temperature reversal (see text for explanation).

††Indicates drying procedure for loaded capsule before welding. Temperature and duration in hours (rounded to nearest hour) separated by slash. Drying at 110°C was in vacuum oven, otherwise in air. For two stage runs, drying conditions for both stages are given, separated by a comma.

†††Numbers in parentheses indicate masses, in micrograms, of aggregate chips included with silicate samples in diffusion test runs. "FB" and "GBR" indicate glass used in aggregate chip, either ferrobasaltic glass or Glass Buttes rhyolite.

¶Abbreviations: glass=gl; olivine=ol; orthopyroxene=opx; clinopyroxene=cpx; spinel=sp.

§Calculated by mass balance. Numbers in parentheses indicate uncertainties; e.g., 16.1(1) represents 16.1±0.1% liquid. The silica contents of 17 of the 18 olivine compositions used to calculate the modes have been adjusted using the stoichiometric constraint for ol that Si (cation%) equals 33.333. For each of these analyses, the SiO_2 (wt%) value was iteratively raised or lowered and cation% calculated until the Si value was within 0.005 units of 33.333. All oxides were then normalized to 100wt%; note that this procedure has no effect on the Mg/(Mg+Fe) ratio of the olivines. Although the correction is relatively small (e.g., mean absolute value of the change in silica contents is 0.26wt%), the correlation coefficients for melt fraction (F) vs. ol and F vs. opx increase dramatically (e.g., for F vs. ol, Pearson correlation coefficient increases from 0.05 to 0.58.).

§§Calculated using normalized analyses for opx and cpx.

Table 3. Experimental results.

Run#†	Phase§	SiO$_2$	TiO$_2$	Al$_2$O$_3$	Cr$_2$O$_3$	FeO*	MnO	MgO	CaO	Na$_2$O	K$_2$O	H$_2$O
9	gl(6)	50.94(26)	0.17(11)	12.19(11)	0.38(6)	8.36(18)	0.19(7)	16.58(22)	10.65(24)	0.44(3)	0.08(1)	
	ol(5)§	41.36(18)	0.01(1)	0.05(1)	0.25(2)	8.94(9)	0.13(2)	49.67(26)	0.24(2)	0.00(0)	0.00(0)	
	opx(12)	56.70(24)	0.02(2)	1.83(21)	0.81(6)	5.26(13)	0.11(2)	33.75(21)	1.30(14)	0.02(1)	0.00(0)	
30	gl(5)	50.38(37)	0.25(8)	12.87(15)	0.42(7)	7.93(31)	0.22(6)	15.43(25)	12.18(19)	0.30(3)	0.02(1)	
	ol(8)	40.96(15)	0.00(0)	0.05(1)	0.27(3)	8.96(12)	0.13(2)	49.15(38)	0.27(1)	0.00(0)	0.00(0)	
	opx(11)	55.73(20)	0.03(2)	3.00(26)	0.84(8)	5.62(8)	0.12(2)	32.22(26)	1.82(6)	0.02(1)	0.00(0)	
1	gl(6)	50.21(21)	0.21(4)	14.15(13)	0.36(5)	7.72(17)	0.15(4)	14.35(17)	12.23(19)	0.55(3)	0.07(0)	
	ol(6)	40.92(15)	0.00(0)	0.04(1)	0.24(2)	8.96(9)	0.14(3)	49.23(26)	0.24(2)	0.00(0)	0.00(0)	
	opx(8)	55.39(42)	0.02(1)	2.94(28)	0.94(5)	5.73(20)	0.10(2)	32.55(34)	1.93(17)	0.02(1)	0.00(0)	
2	gl(9)	49.44(21)	0.28(8)	15.43(14)	0.27(5)	7.34(16)	0.16(7)	12.77(20)	13.61(22)	0.60(4)	0.08(1)	
	ol(3)	41.30(15)	0.00(0)	0.04(1)	0.21(2)	9.24(9)	0.12(2)	49.26(26)	0.31(1)	0.00(0)	0.00(0)	
	opx(4)	54.86(38)	0.04(2)	3.58(25)	0.98(6)	5.68(18)	0.10(2)	31.93(34)	2.45(7)	0.02(1)	0.00(0)	
19C	gl(5)	50.02(22)	0.34(5)	14.84(13)	0.25(4)	7.22(23)	0.13(9)	13.29(32)	13.10(21)	0.67(7)	0.10(2)	
	ol(9)	40.97(15)	0.00(0)	0.05(1)	0.15(2)	9.33(9)	0.14(3)	48.99(40)	0.27(1)	0.00(0)	0.00(0)	
	opx(4)	55.68(20)	0.02(2)	2.98(13)	0.91(6)	5.50(20)	0.11(2)	33.06(21)	2.24(10)	0.02(1)	0.00(0)	
20C	gl in chip(4)	49.50(24)	0.33(8)	14.92(13)	0.31(5)	7.34(16)	0.10(3)	13.49(16)	13.23(21)	0.67(5)	0.10(1)	
	gl in vit.C(4)	49.37(21)	0.32(9)	15.15(14)	0.30(5)	7.37(16)	0.11(4)	13.32(16)	13.25(21)	0.70(1)	0.09(1)	
	ol(9)	40.88(18)	0.00(0)	0.05(1)	0.21(2)	9.21(10)	0.13(2)	48.98(26)	0.30(1)	0.00(0)	0.00(0)	
	opx(6)	56.12(20)	0.03(1)	2.53(16)	0.78(5)	5.69(9)	0.13(2)	32.97(18)	2.18(6)	0.02(1)	0.00(0)	
26C	gl(6)	50.16(28)	0.27(4)	13.77(14)	0.27(4)	7.81(21)	0.15(7)	14.09(33)	12.80(20)	0.56(3)	0.07(2)	
	ol(8)	40.62(15)	0.00(0)	0.06(2)	0.16(1)	9.32(11)	0.14(3)	49.36(30)	0.27(1)	0.00(0)	0.00(0)	
	opx(7)	55.95(22)	0.02(2)	2.56(26)	0.91(7)	5.79(8)	0.10(2)	32.79(29)	1.81(9)	0.02(1)	0.00(0)	
25R	gl(7)	49.20(24)	0.30(4)	14.16(14)	0.23(3)	7.61(17)	0.11(4)	14.18(17)	13.55(21)	0.56(3)	0.07(1)	
	ol(4)	41.11(29)	0.00(0)	0.05(2)	0.19(2)	9.13(19)	0.13(2)	49.24(29)	0.30(1)	0.00(0)	0.00(0)	
	opx(4)	55.94(20)	0.02(2)	2.78(30)	0.74(9)	5.66(14)	0.13(2)	32.59(18)	2.10(9)	0.02(1)	0.00(0)	
23R	gl(7)	48.99(24)	0.28(9)	15.37(17)	0.22(6)	7.91(17)	0.09(5)	12.60(29)	13.66(22)	0.81(10)	0.07(1)	
	ol(8)	40.84(15)	0.00(0)	0.05(1)	0.17(3)	9.44(10)	0.14(3)	49.60(26)	0.29(3)	0.00(0)	0.00(0)	
	opx(6)	54.86(20)	0.05(2)	3.65(22)	0.98(5)	5.82(7)	0.12(2)	32.07(27)	2.32(7)	0.03(1)	0.00(0)	
	cpx(6)	52.10(28)	0.03(2)	5.10(19)	1.34(8)	3.80(11)	0.11(2)	20.02(26)	17.04(30)	0.12(2)	0.00(0)	

Table 3, continued. Experimental results.

Run#†	Phase§	SiO₂	TiO₂	Al₂O₃	Cr₂O₃	FeO*	MnO	MgO	CaO	Na₂O	K₂O	H₂O
3	gl(11)	49.64(21)	0.28(4)	15.12(14)	0.29(4)	7.41(16)	0.13(3)	13.32(16)	13.12(21)	0.60(3)	0.08(1)	1.2(2)
	ol(9)	41.13(15)	0.00(0)	0.04(1)	0.19(4)	9.25(11)	0.13(2)	49.07(26)	0.28(1)	0.00(0)	0.00(0)	
	opx(2)	55.30(52)	0.05(1)	3.24(10)	0.79(4)	5.63(15)	0.10(2)	31.69(17)	2.54(13)	0.03(1)	0.00(0)	
22	gl(7)	48.05(51)	0.39(6)	17.72(20)	0.17(3)	7.07(16)	0.18(5)	12.01(30)	13.31(21)	0.96(5)	0.08(1)	0.3(1)
	ol(5)	39.58(21)	0.00(0)	0.07(4)	0.18(5)	9.45(9)	0.14(3)	49.67(26)	0.27(2)	0.00(0)	0.00(0)	
	opx(4)	55.22(45)	0.01(1)	2.44(23)	0.83(10)	5.85(7)	0.10(2)	33.35(18)	1.68(13)	0.02(1)	0.00(0)	
	cpx(4)	50.89(30)	0.12(3)	6.27(36)	1.00(5)	3.91(12)	0.10(2)	19.95(38)	16.82(22)	0.14(2)	0.00(0)	
	sp(2)	0.29(2)	0.11(2)	34.19(32)	35.95(54)	10.35(10)	0.14(3)	18.66(10)	0.02(1)	0.01(1)	0.00(0)	
17R	gl(11)	48.79(35)	0.39(18)	16.88(15)	0.19(7)	7.28(24)	0.14(9)	12.14(14)	12.84(20)	1.14(5)	0.17(2)	
	ol(10)	40.81(15)	0.00(0)	0.05(1)	0.13(1)	9.60(14)	0.14(3)	48.71(26)	0.27(1)	0.00(0)	0.00(0)	
	opx(5)	54.24(54)	0.08(2)	4.83(46)	0.79(7)	5.84(7)	0.13(2)	31.57(39)	2.18(11)	0.05(2)	0.00(0)	
	cpx(4)	52.07(39)	0.11(3)	5.47(16)	1.02(7)	3.83(13)	0.11(2)	20.03(38)	17.39(38)	0.21(3)	0.00(0)	
	sp(3)	0.60(52)	0.09(2)	47.62(43)	21.89(23)	8.92(9)	0.11(2)	20.35(37)	0.05(1)	0.00(0)	0.00(0)	
12	gl(11)	48.86(20)	0.41(10)	17.60(16)	0.19(5)	6.84(15)	0.16(5)	11.72(16)	13.20(21)	0.84(4)	0.14(2)	
	ol(8)	40.83(15)	0.00(0)	0.03(1)	0.11(1)	9.42(13)	0.14(3)	49.15(26)	0.25(1)	0.00(0)	0.00(0)	
	opx(4)	55.30(20)	0.04(2)	3.49(26)	0.92(9)	5.78(7)	0.12(2)	32.27(39)	2.25(21)	0.02(1)	0.00(0)	
	cpx(4)	52.46(34)	0.08(2)	5.23(51)	1.15(5)	3.80(8)	0.12(2)	20.00(36)	17.80(41)	0.15(2)	0.00(0)	
	sp(2)	0.26(7)	0.06(3)	44.60(95)	25.11(1.14)	9.32(42)	0.12(4)	20.06(11)	0.02(1)	0.00(0)	0.00(0)	
27C	gl(13)	48.20(20)	0.48(7)	15.94(16)	0.12(4)	7.30(21)	0.09(6)	12.74(26)	13.88(22)	1.12(6)	0.09(2)	
	ol(5)	40.82(30)	0.00(0)	0.05(1)	0.08(1)	9.56(9)	0.13(2)	49.07(44)	0.24(1)	0.00(0)	0.00(0)	
	opx(8)	55.02(48)	0.05(1)	3.70(14)	0.88(15)	5.98(11)	0.12(2)	31.66(17)	2.21(10)	0.04(2)	0.00(0)	
	cpx(10)	52.17(46)	0.09(2)	5.15(54)	1.20(12)	3.82(9)	0.10(2)	18.72(24)	18.04(33)	0.18(3)	0.00(0)	
	sp(2)	0.39(32)	0.09(2)	39.81(1.53)	30.11(2.09)	10.51(17)	0.13(2)	19.73(60)	0.04(1)	0.00(0)	0.00(0)	
28C	gl(6)	48.07(20)	0.58(25)	15.92(25)	0.15(6)	7.54(18)	0.15(6)	12.35(19)	13.72(22)	1.38(10)	0.14(2)	
	ol(4)	41.01(15)	0.00(0)	0.07(1)	0.09(3)	9.65(13)	0.13(2)	48.44(29)	0.30(3)	0.00(0)	0.00(0)	
	opx(6)	53.76(27)	0.07(2)	5.01(36)	0.80(5)	6.05(11)	0.12(2)	31.35(17)	2.26(10)	0.04(2)	0.00(0)	
	cpx(4)	51.72(37)	0.11(5)	5.61(42)	1.01(5)	3.88(15)	0.11(2)	19.07(65)	17.60(65)	0.28(3)	0.00(0)	
	sp(4)	0.84(17)	0.10(2)	48.76(1.02)	19.82(87)	9.29(17)	0.12(2)	20.90(15)	0.07(2)	0.00(0)	0.00(0)	

Table 3, continued. Experimental results.

Run#†	Phase§	SiO₂	TiO₂	Al₂O₃	Cr₂O₃	FeO*	MnO	MgO	CaO	Na₂O	K₂O	H₂O
21	gl(11)	51.34(40)	0.55(8)	17.34(16)	0.12(4)	5.54(15)	0.10(6)	10.19(23)	13.23(21)	1.45(8)	0.12(4)	
	ol(10)	40.57(15)	0.00(0)	0.06(2)	0.10(1)	9.76(10)	0.11(2)	49.04(26)	0.25(1)	0.00(0)	0.00(0)	
	opx(7)	54.74(23)	0.04(1)	4.15(48)	0.74(8)	5.87(9)	0.13(2)	31.74(29)	2.15(25)	0.03(1)	0.00(0)	
	cpx(3)	52.34(19)	0.08(2)	4.27(10)	1.20(6)	3.91(6)	0.12(2)	19.96(24)	17.39(47)	0.22(4)	0.00(0)	
	sp(3)	0.26(9)	0.10(2)	43.46(77)	26.58(29)	9.58(9)	0.15(3)	19.63(23)	0.03(1)	0.00(0)	0.00(0)	
11	gl(15)	50.58(42)	0.46(8)	18.36(16)	0.07(3)	5.94(26)	0.13(4)	9.81(18)	12.41(22)	1.93(10)	0.30(2)	0.9(1)
	ol(6)	40.69(15)	0.00(0)	0.07(4)	0.08(2)	9.74(10)	0.13(2)	49.22(26)	0.26(3)	0.00(0)	0.00(0)	
	opx(5)	55.14(38)	0.06(2)	4.16(21)	0.84(20)	5.81(12)	0.12(2)	32.35(60)	1.84(34)	0.03(1)	0.00(0)	
	cpx(4)	51.92(28)	0.07(3)	4.43(24)	1.31(7)	3.58(8)	0.12(2)	19.38(29)	18.23(27)	0.17(2)	0.00(0)	
	sp(3)	0.73(31)	0.12(3)	37.91(97)	31.96(20)	10.28(39)	0.14(3)	18.82(16)	0.06(3)	0.00(0)	nd	
33C	gl(10)	47.96(20)	0.63(8)	17.77(16)	0.09(3)	7.29(16)	0.13(4)	10.35(12)	13.19(21)	2.08(10)	0.51(1)	
	ol(6)	40.99(15)	0.00(0)	0.05(2)	0.08(2)	9.61(15)	0.12(3)	48.42(26)	0.24(1)	0.00(0)	nd	
	opx(6)	54.28(20)	0.08(2)	5.04(22)	0.73(5)	5.99(7)	0.13(2)	31.19(17)	2.28(11)	0.04(1)	nd	
	cpx(4)	51.21(24)	0.16(3)	5.90(38)	0.97(5)	3.90(12)	0.10(2)	19.08(25)	17.84(14)	0.27(2)	nd	
	sp(2)	0.75(61)	0.12(3)	49.34(56)	19.22(1.12)	9.66(35)	0.14(5)	20.36(1.03)	0.07(4)	0.00(0)	nd	
34C	gl(7)	48.83(20)	0.50(7)	16.87(15)	0.11(3)	7.19(16)	0.18(5)	11.51(22)	13.04(21)	1.43(7)	0.33(2)	
	ol(4)	40.83(15)	0.00(0)	0.04(1)	0.10(2)	9.72(20)	0.14(3)	48.08(26)	0.25(2)	0.00(0)	nd	
	opx(8)	54.27(20)	0.04(1)	4.58(29)	0.88(12)	5.97(7)	0.12(2)	31.02(25)	2.18(9)	0.04(2)	nd	
	cpx(3)	51.75(54)	0.11(6)	4.74(24)	1.16(18)	3.89(9)	0.12(2)	19.30(30)	17.60(38)	0.31(14)	nd	
	sp(3)	0.82(42)	0.08(2)	48.15(1.46)	20.83(1.72)	9.58(9)	0.12(2)	19.92(18)	0.06(3)	0.00(0)	nd	
42C	gl(7)	47.91(20)	0.59(7)	17.54(16)	0.11(3)	7.28(17)	0.13(4)	11.42(17)	13.25(21)	1.60(8)	nd	
	ol(9)	40.59(15)	0.00(0)	0.05(1)	0.08(2)	9.74(15)	0.13(2)	49.44(26)	0.23(1)	0.00(0)	nd	
	opx(4)	54.17(40)	0.06(2)	3.93(12)	0.93(21)	5.91(16)	0.13(2)	32.45(50)	2.19(6)	0.04(2)	nd	
	cpx(6)	51.83(19)	0.09(2)	4.87(37)	1.21(5)	3.76(9)	0.11(2)	19.71(40)	18.07(25)	0.17(3)	nd	
	sp(3)	0.49(23)	0.11(2)	42.35(1.72)	28.49(1.83)	10.19(13)	0.14(3)	19.73(24)	0.05(3)	0.00(0)	nd	
36	ol(9)	40.84(18)	0.00(0)	0.07(5)	0.06(2)	9.70(11)	0.13(2)	49.07(30)	0.14(4)	0.00(0)	nd	
	opx(7)††	54.03(65)	0.07(2)	4.80(25)	0.71(8)	6.09(15)	0.13(2)	32.17(52)	1.95(11)	0.05(2)	nd	
	cpx(16)††	51.71(40)	0.19(6)	5.74(32)	0.98(8)	3.67(15)	0.10(2)	18.67(60)	18.52(33)	0.42(15)	nd	
	sp(3)	1.21(1.03)	0.10(1)	47.74(74)	20.37(93)	10.24(21)	0.13(2)	19.30(24)	0.11(14)	0.01(1)	nd	

Table 3, continued. Experimental results.

Run††	Phase§	SiO$_2$	TiO$_2$	Al$_2$O$_3$	Cr$_2$O$_3$	FeO*	MnO	MgO	CaO	Na$_2$O	K$_2$O	H$_2$O
VG2(gl)	(121)‡	50.35(50)	1.79(14)	13.92(20)	0.02(3)	11.57(23)	0.19(5)	6.88(11)	10.88(14)	2.78(9)	0.21(2)	
VG2(xtl)	(55)	50.52(26)	1.82(9)	13.94(19)	0.02(2)	11.51(15)	0.21(3)	6.90(10)	10.87(17)	2.81(6)	0.20(2)	
BGIO(gl)	(103)	51.20(57)	1.28(12)	15.15(24)	0.05(4)	9.01(25)	0.16(5)	8.04(15)	11.13(20)	2.76(14)	0.09(2)	
BGIO(xtl)	(64)	51.37(35)	1.29(9)	15.22(25)	0.05(2)	8.97(16)	0.16(3)	8.03(13)	11.15(19)	2.79(14)	0.09(2)	
JHYP	(103)‡	54.46(46)	0.08(2)	0.85(4)	0.78(4)	14.72(25)	0.48(3)	27.33(22)	1.16(5)	0.01(1)	0.01(1)	
DIOP	(116)‡	55.60(52)	0.02(2)	0.20(10)	0.02(2)	0.29(3)	0.03(2)	18.06(21)	25.69(37)	0.17(6)	0.01(1)	

† C indicates convergence test; R indicates temperature reversal run (see text for explanation).

¶Abbreviations: glass=gl; olivine=ol; orthopyroxene=opx; clinopyroxene=cpx; spinel=sp.

§Reported olivine analyses are unadjusted. Numbers in parentheses after phase name are number of averaged analyses.

††Reported analyses have been normalized to 100 wt%. Repeated attempts to analyze the silicate phases in this charge consistently produced low analytical totals. The opx and cpx analyses reported here have nominal sums of 98.6 and 98.9 wt%, respectively. Following the calculations outlined in Cameron and Papike (1981), both compositions have acceptable pyroxene stoichiometries.

‡Number of averaged analyses of secondary standard. VG2=basaltic glass, BGIO=Indian Ocean basaltic glass, averages reported at glass analysis conditions and crystal conditions; JHYP=Johnstown hypersthene; DIOP=Natural Bridge diopside. Numbers in parentheses indicate uncertainties; e.g. 16.1(1) represents 16.1±0.1; nd=not determined.

Figure 3-1. Oxide-MgO variation diagrams showing comparing the composition of

moderately depleted peridotite composition DMM1 used in this study (filled square) to

estimates of primitive upper mantle (diagonally-hachured field; Ringwood, 1979; Hart

and Zindler, 1986; McDonough and Frey, 1989); reconstructed abyssal peridotite

compositions (horizontally-dashed field; Baker and Beckett, 1998); and starting

compositions used in other high-pressure experimental studies (circles; HPy=pyrolite,

HPy-40=pyrolite-40% ol, TL=Tinaquillo lherzolite, TL-40=Tinaquillo lherzolite-40% ol,

Jaques and Green, 1980, Falloon and Green, 1987, and Robinson et al., 1998; 77PAII-1,

Sen, 1982; HK-66 and KLB-1, Hirose and Kushiro, 1993; mm3, Baker and Stolper, 1994,

Baker et al., 1995, and Hirschmann et al., 1998a; PHN1611, Kushiro, 1996). (a) Na_2O

vs. MgO, (b) Al_2O_3 vs. MgO, (c) CaO vs. MgO.
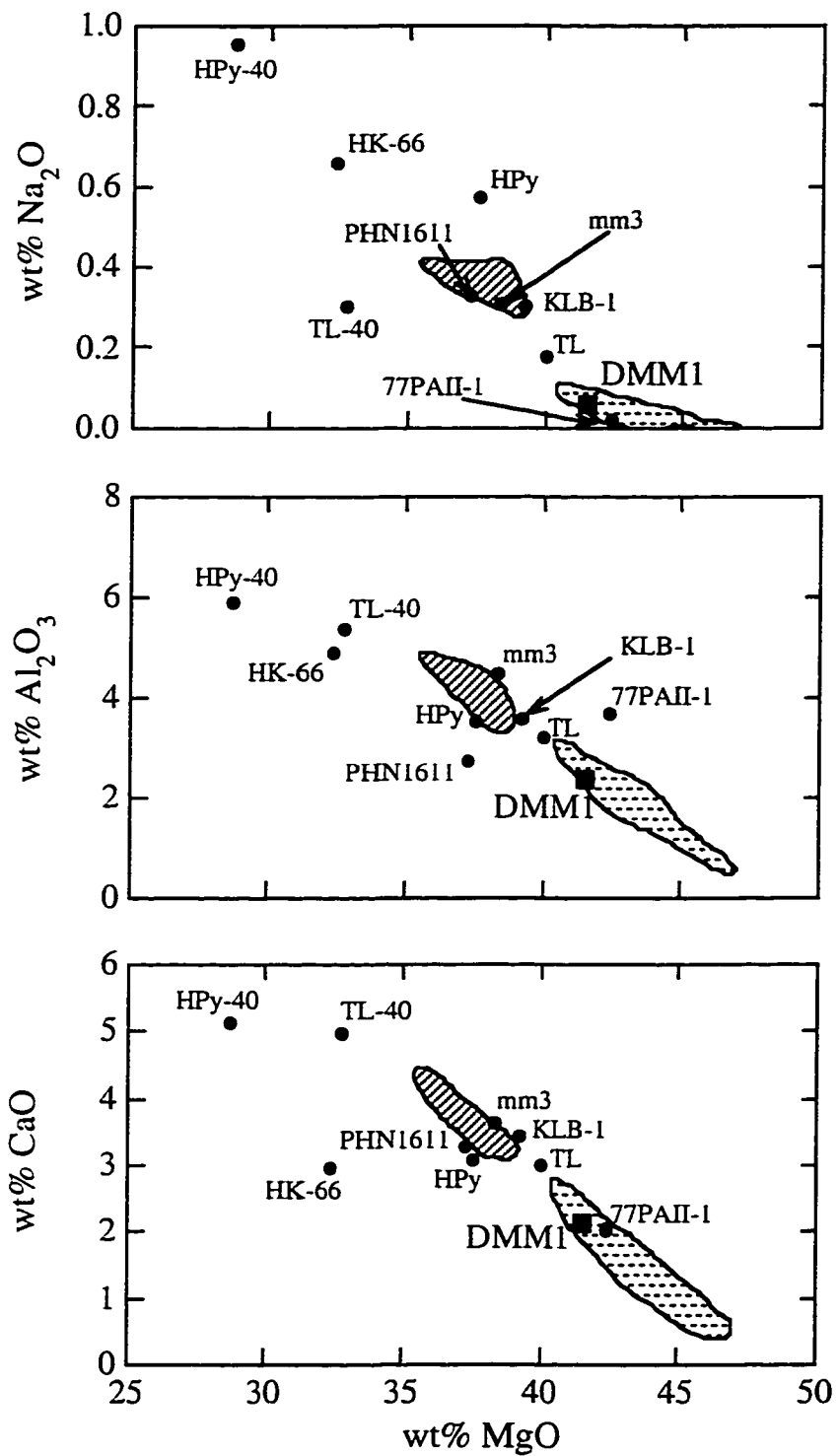
Figure 3-2. Cross sections of different capsule configurations used in this study. (a) First

stage run starts with peridotite powder. (b) Second stage, run at the same temperature,

contains the peridotite plug from the first stage run and several layers of 80-100 µm

vitreous carbon spheres. In some cases the spheres were placed directly on the bottom,

inner surface of the graphite crucible, and in other cases a small hole was drilled into the

bottom of the graphite crucible and filled with spheres. The vitreous carbon spheres are

not drawn to scale. For the temperature reversal experiments, powdered peridotite was

packed atop the carbon spheres. Each capsule was inverted before being placed into the

piston cylinder assembly. (c) Configuration of the single-stage compositional

convergence experiments. Chip of glass-filled vitreous carbon aggregate is

approximately 50 microns across and initially contains ~15% by mass of either the Fe-

rich basaltic glass (FB) or Glass Buttes rhyolite (GBR).

(a)

(b)

(c)
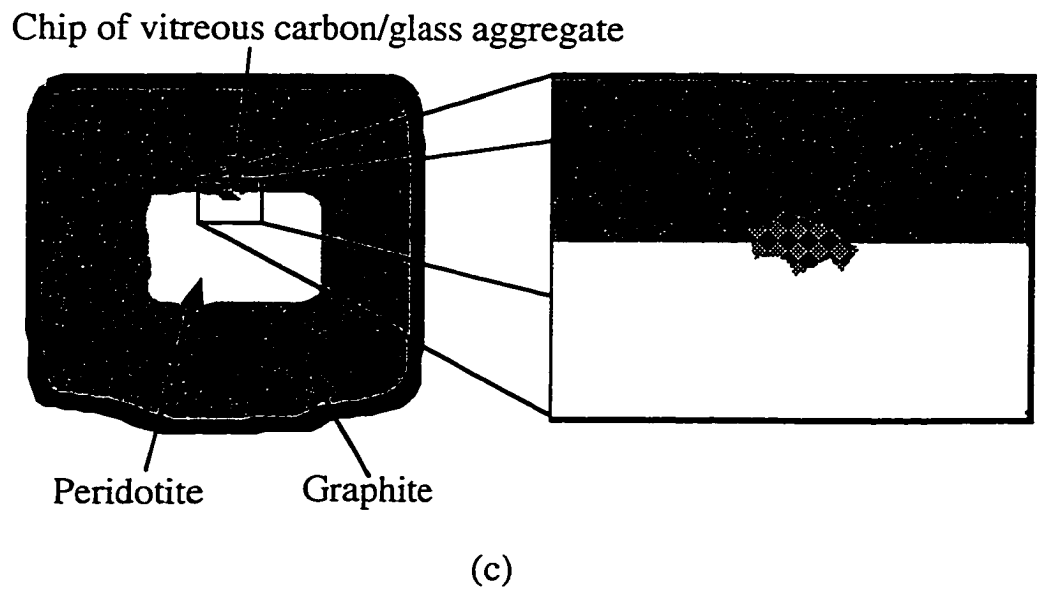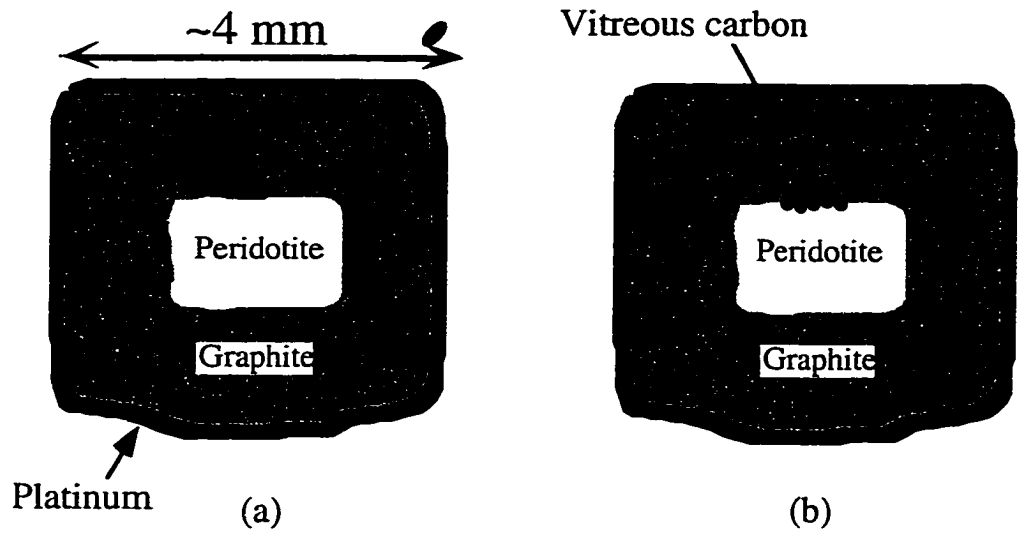
Figure 3-3. Results of compositional convergence experiments. Shaded square is initial

composition of Fe-rich basalt (FB). Shaded circle is initial composition of Glass Buttes

rhyolite (GBR). Arrows indicate change in composition of glass within aggregate chip.

Filled diamonds represent glasses coexisting with ol, opx, cpx, sp; open symbols are

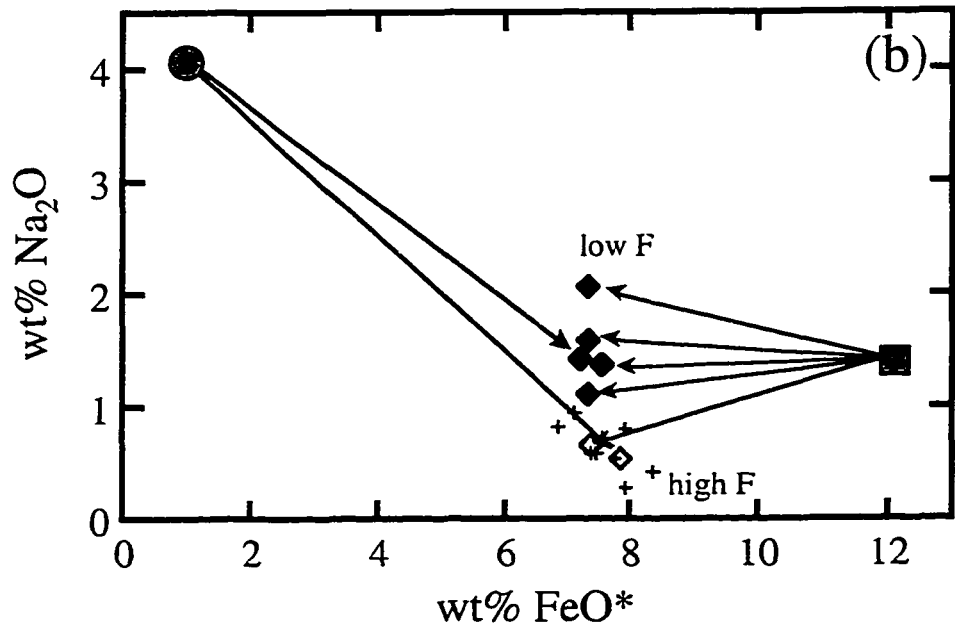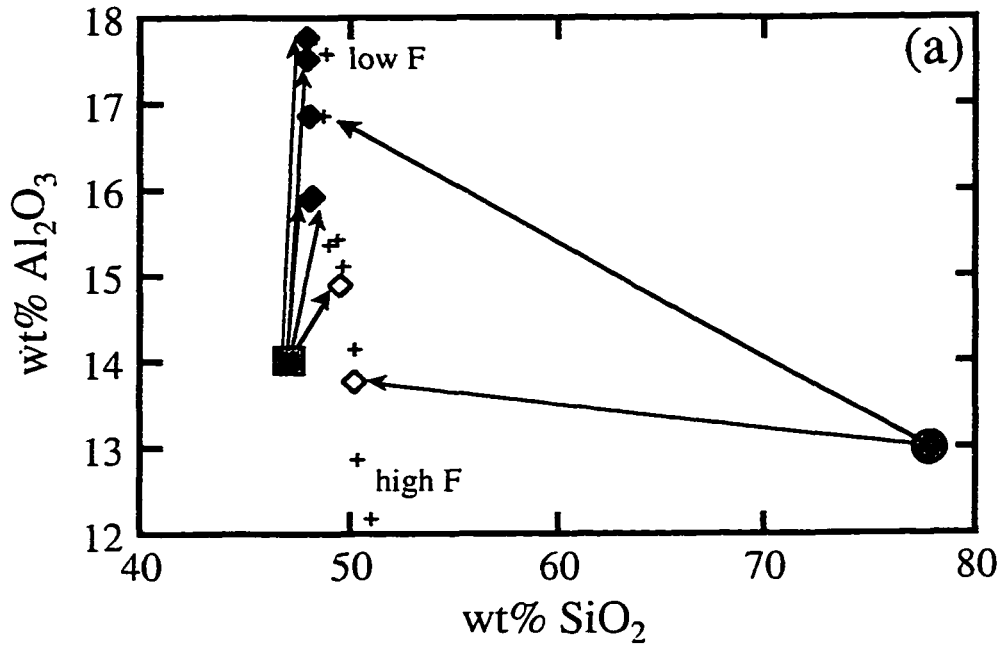glasses coexisting with ol, opx. Crosses are two-stage and temperature reversal

experiments.

Figure 3-4. Variation diagrams showing oxide concentrations in the experimental glasses

as a function of MgO content of the glasses. Circles represent glass compositions from

the two-stage experiments; triangles represent glass compositions from the temperature

reversal runs; diamonds show the compositions of glasses from the compositional

convergence experiments (see Tables 3-2 and 3-3). Error bars are 1σ; if not shown, error

bars are smaller than the symbols. Here and in the following figures, filled symbols

represent glass coexisting with ol, opx, cpx, and sp; open symbols represent glass

coexisting with ol and opx. (a) SiO_2, (b) TiO_2, (c) Al_2O_3, (d) Cr_2O_3, (e) FeO^*, (f) CaO,

(g) Na_2O.
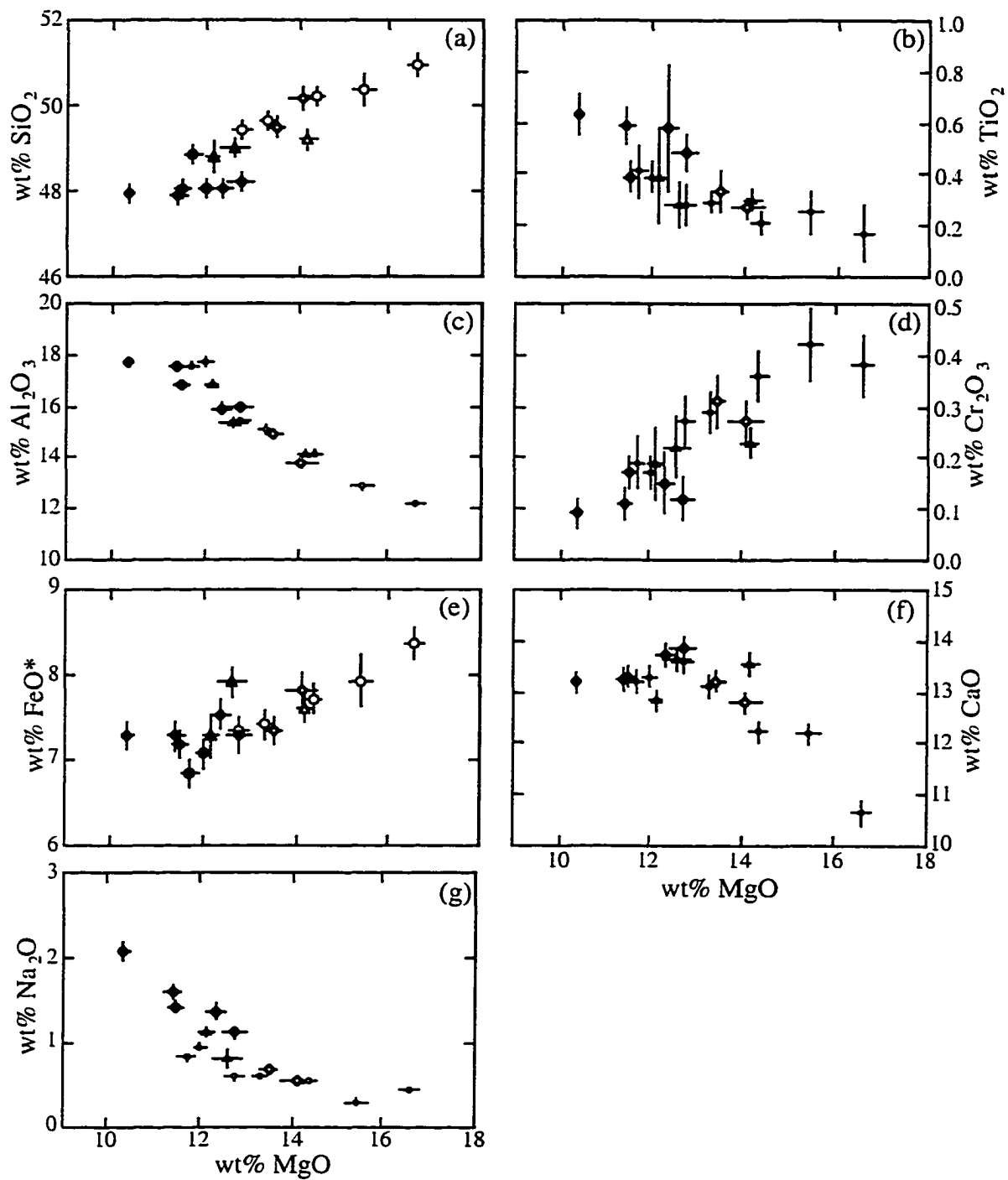
Figure 3-5. Calculated K_{D,Fe^*-Mg}^{ol-liq} vs. glass MgO content from the two-stage, temperature

reversal, and compositional convergence experiments; same symbols as in Figure 3-4.

Uncertainties on the ol-liq K_D values are calculated by propagating uncertainties in the
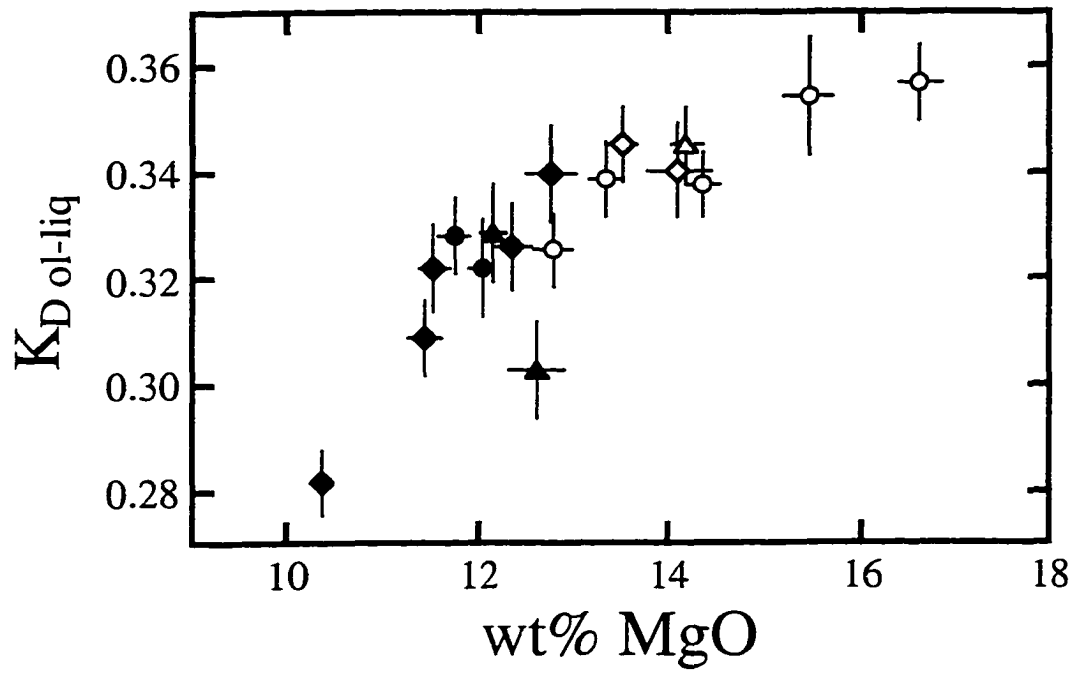
FeO* and MgO values for both olivine and glass.

Figure 3-6. Wollastonite contents (Ca/[Ca+Mg+Fe*], molar) in (a) cpx and (b) opx rim

compositions from the two-stage, temperature reversal, and compositional convergence

experiments versus MgO contents of glasses; same symbols as in Figure 3-4. Error bars

represent 1σ and for Wo-contents are calculated by propagating uncertainties in the three

oxide concentrations. Filled symbols represent opx and cpx coexisting with ol and sp;
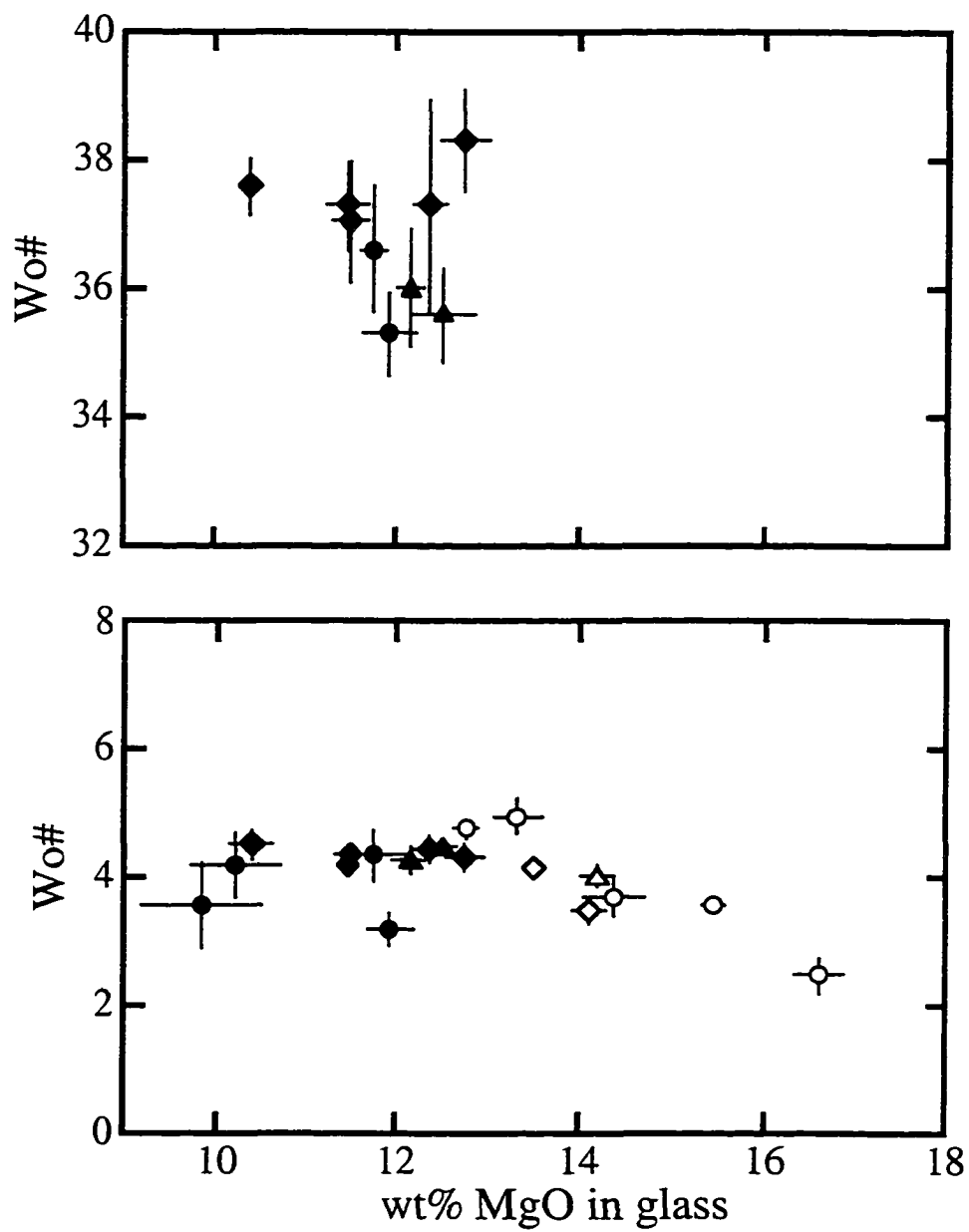
open symbols represent opx coexisting with ol.

Figure 3-7. Melt fraction (by weight) from the two-stage, temperature reversal, and

compositional convergence experiments as a function of (a) run temperature and (b) MgO

content of the glass from each experiment. Proportions of glass and residual crystals in

each run were determined by mass balance. The calculations were made using the non-

linear regression algorithms of Albarède and Provost (1977) and require uncertainties on

the bulk composition and all phase compositions; only rim compositions of pyroxenes

were used in the fits (Table 3-3). Symbols as in Figure 3-4; filled or open symbols

indicate the presence or absence of cpx and sp in the residual assemblage.
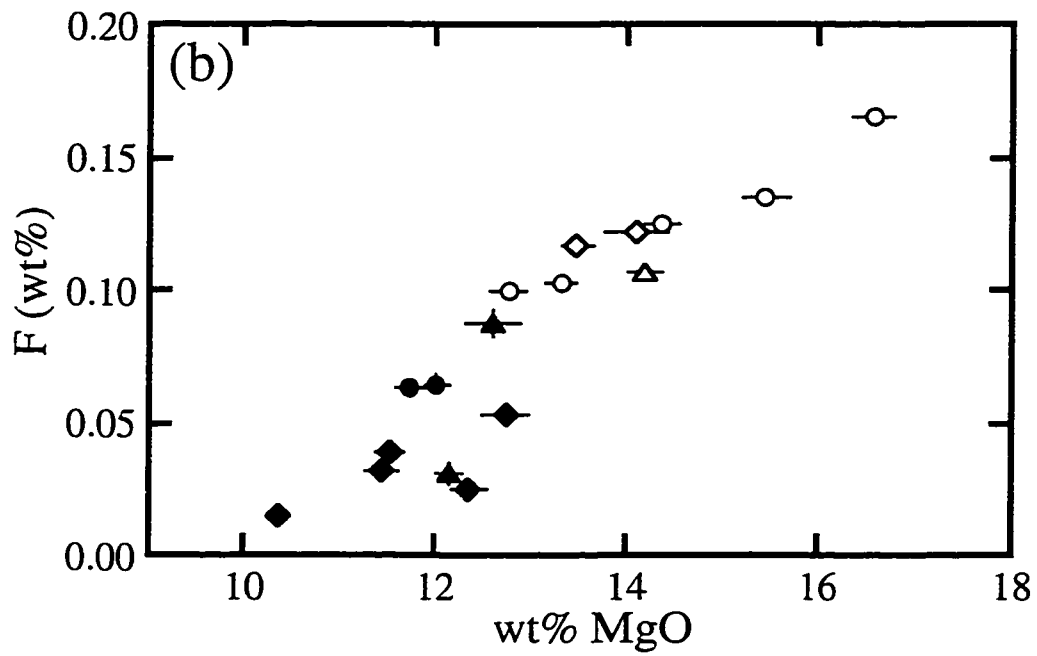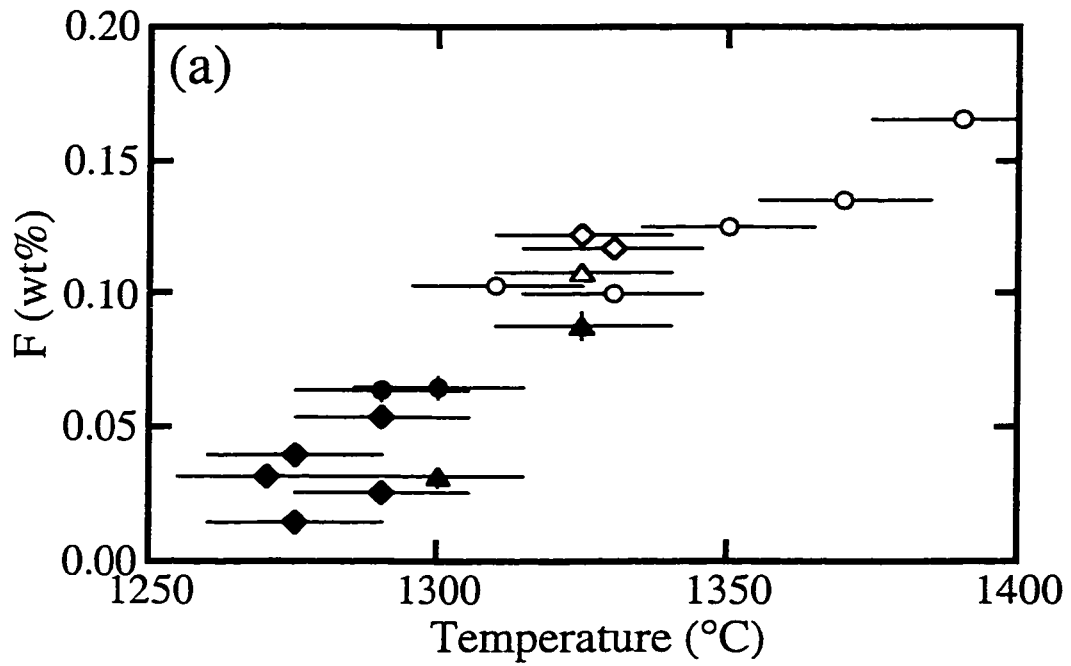
Figure 3-8. Weight fractions of residual crystalline phases as a function of glass weight fraction in experiments from this study. For each experiment, the weight fraction of all phases (crystals and glass) equals 1.0 (see Table 3-2). Filled symbols represent spinel lherzolite assemblages, while open symbols represent harzburgite residual assemblages. Circles are olivine, squares are opx, triangles are cpx, diamonds are sp. Error bars on all phases are 2σ, and for several experiments are smaller than the symbols. The solid lines are unweighted least-squares fits to the phase proportions in the super-solidus and subsolidus experiments (F was set to zero in the subsolidus run, #36). For the spinel lherzolite assemblages, the equations of the fits are ol = 0.632 + 0.348*F; opx = 0.282 - 0.570*F; cpx = 0.079 - 0.717*F; sp = 0.006 - 0.045*F. Equations in the residual harzburgite field are ol = 0.641 + 0.246*F; opx = 0.359 - 1.245*F. Thus melting reactions are 0.35 opx + 0.72 cpx + 0.04 sp = 0.35 ol + 1 liquid and 1.25 opx = 0.25 ol + 1 liquid, respectively.
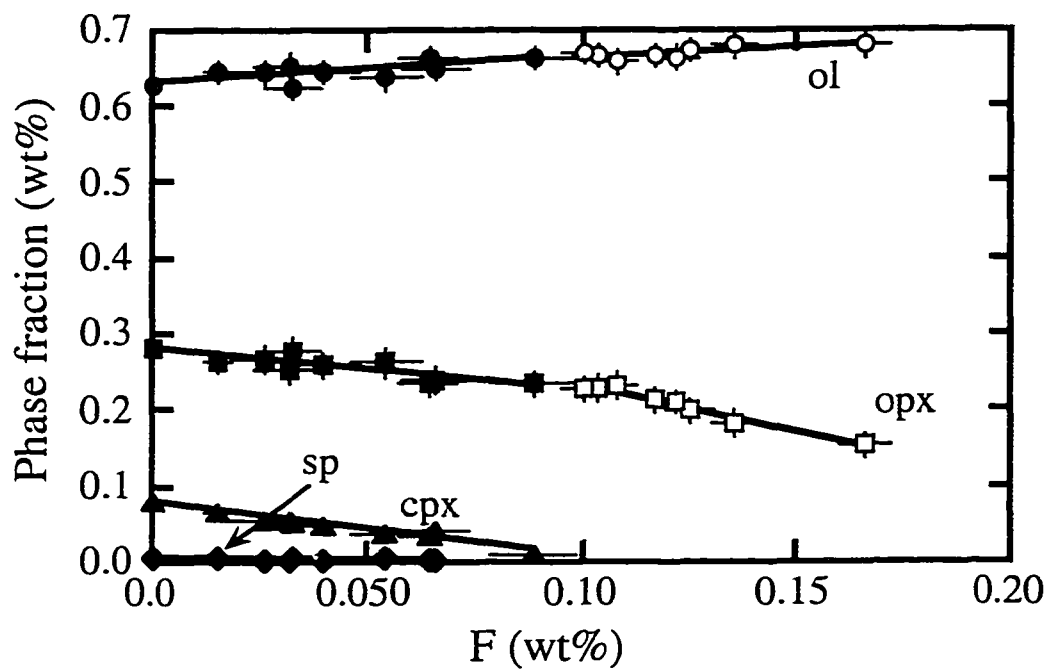
Appendix to Chapter 3: Oxygen fugacity in experimental charges

Although oxygen fugacity was not controlled in any of the experiments presented in this thesis, each sample was contained within a graphite inner capsule. This configuration ensures that oxygen fugacity is held below the carbon-CO-CO$_2$ oxygen buffer. I have measured the oxygen fugacity within one of the charges more precisely in order to assess whether the experiments match well with estimates of oxygen fugacity in the relevant part of the upper mantle.

In order to make the oxygen fugacity (fO$_2$) measurement, I included a very small (13 microgram) piece of Pt wire within the peridotite portion of the capsule for experiment #25, which, at 1325°C, is roughly in the middle of the temperature range covered by all of the 10 kbar experiments. During the experiment, some Fe alloyed with the Pt to form an Fe-Pt alloy coexisting with Fe-bearing olivine (ol) and orthopyroxene (opx). The compositions of these three phases can be measured to determine oxygen fugacity via the following equilibrium reaction (Bertka and Holloway, 1988; Gudmundsson et al., 1988):

$$2Fe_2SiO_4 = Fe_2Si_2O_6 + 2Fe + O_2. \tag{1}$$

For this reaction,

$$\Delta G^0 = -RT \ln K$$

$$K = \frac{\left(a_{Fe_2Si_2O_6}^{opx}\right)\left(a_{Fe}^{alloy}\right)^2 \left(f O_2\right)}{\left(a_{Fe_2SiO_4}^{ol}\right)^2}, \tag{2}$$

where ΔG^0 is the Gibbs free energy of the reaction for pure phases at the temperature and pressure of the experiment, R is the gas constant, T is the Kelvin temperature, a_i^j is the activity of endmember i in phase j, and fO$_2$ is the oxygen fugacity. Rearranging to solve for log fO$_2$:

$$\ln fO_2 = -\frac{\Delta G^0}{RT} + 2\ln a^{ol}_{Fe_2SiO_4} - \ln a^{opx}_{Fe_2Si_2O_6} - \ln a^{alloy}_{Fe}$$

$$\log fO_2 = \log\left(e^{\ln fO_2}\right)$$

$$(3)$$

In order to solve this equation for $\log fO_2$, it is necessary to (1) measure the compositions of ol, opx, and Fe-Pt alloy, (2) employ an activity model which relates the concentrations of Fe-bearing components in ol, opx, and Fe-Pt alloy to activities of Fe-bearing components, and (3) determine a value for ΔG^0 by finding appropriate values for the molar Gibbs free energies of pure Fe-bearing phases at the relevant conditions. I present two methods of solving for $\log fO_2$ below. The first is the method of Jamieson et al. (1992). The second uses the formula developed by Gudmundsson and Holloway (1993). Both groups have developed equations relating oxygen fugacity to the activities of Fe-bearing components in ol, opx, and Fe-Pt alloy from thermodynamic data and tested their formulas by conducting controlled fO_2 experiments. The difference between the two methods lies in slightly different choices of solution models for ol, opx, and Fe-Pt alloy. Answers from the two methods differ slightly and are both compared to estimates of upper mantle oxygen fugacity at the end of this appendix.

Compositions of ol and opx in experiment #25 were measured by electron microprobe as described in the analytical techniques section of Chapter 3. Fe-Pt alloy was also analyzed by electron microprobe, using a beam current of 50 nA and pure Fe and Pt metal standards. Ol and opx grains immediately adjacent to the Fe-Pt wire had slightly higher FeO* (all Fe calculated as FeO) concentrations than grains farther away from the wire. This is most likely because experiment #25 was a temperature half-reversal as described above in Chapter 3; the temperature was held at 1285°C initially and then raised to 1325°C for the latter part of the run. When the temperature was raised, some of the Fe which had alloyed with the Pt recombined with oxygen and dissolved in ol or opx. There was not sufficient time for the FeO* gradient in ol and opx to disappear

before the run was quenched. The difference in composition is slight, however; when log

fO_2 is calculated using the compositions of grains neighboring the Fe-Pt wire and with

compositions of distant ol and opx grains using the second method below, the answers

differ by only 0.08 log units. The compositions of ol, opx, and Fe-Pt alloy are as follows:

Fayalite mole fraction in olivine near Fe-Pt alloy............................. 0.098
Fayalite mole fraction in olivine far from Fe-Pt alloy (used in fO_2
  calculations)... 0.093
Ferrosilite mole fraction in opx near Fe-Pt alloy............................. 0.092
Ferrosilite mole fraction in opx far from Fe-Pt alloy (used in fO_2
  calculations)... 0.088
Fe mole fraction in Fe-Pt alloy.. 0.403

Inclusion of the Pt wire within the experimental charge does not remove enough Fe from

the peridotite to affect phase relations or compositions; initially 13 micrograms and now

40.3% Fe (by moles), the alloy contains approximately 2.51 micrograms of Fe, 0.001% of

the Fe originally in the peridotite.

Calculation of oxygen fugacity using the method of Jamieson et al. (1992)

I calculated the fO_2 in experiment #25 with the method of Jamieson et al. (1992),

who used a compilation of thermodynamic data to develop an equation for oxygen

fugacity as a function of T, P, and the activities of Fe endmembers in coexisting olivine,

opx, and Fe-Pt alloy. They then conducted experiments with controlled oxygen fugacity

to verify the applicability of their equation for pressures between 1 bar and 10 kilobars

and 1300-1450°C. The equation is:

$$\log fO_2 = 5.50 - \frac{26716.6}{T} + \frac{0.0656(P-1)}{T} + 2\log a^{ol}_{Fe_2SiO_4} - 2\log a^{alloy}_{Fe} - 2\log a^{opx}_{FeSiO_3}, (4)$$

where T is the Kelvin temperature and P the pressure in bars.

Jamieson et al. (1992) use an ideal mixing model for the activity of ferrosilite in opx, such that

$$a^{opx}_{FeSiO_3} = X^{opx}_{FeSiO_3} = 0.088$$

$$\log a^{opx}_{FeSiO_3} = -1.056. \tag{5}$$

The activity-composition relations for Fe in Fe-Pt alloy is taken from the experimental work of Heald (1967), as above, thus

$$\log a^{alloy}_{Fe} = -1.532. \tag{6}$$

For olivine, Jamieson et al. (1992) assume a regular solution model with $W^{ol}_{Mg-Fe} = 5000 J / g \cdot atom$ for $(Mg,Fe)Si_{0.5}O_2$ or $10000 J / g \cdot atom$ for

$(Mg,Fe)_2SiO_4$.

For symmetric, regular solutions with mixing on two sites,

$$a^{ol}_{Fe_2SiO_4} = \left(X^{ol}_{Fe_2SiO_4} \gamma^{ol}_{Fe_2SiO_4} \right)^2. \tag{7}$$

To determine the value of γ, the expression for the chemical potential of pure fayalite in olivine is:

$$\mu^{ol}_{Fe_2SiO_4} = \mu^{o\,ol}_{Fe_2SiO_4} + \mu_{ideal} + \mu_{excess}, \tag{8}$$

which for a regular solution with mixing on two sites is equivalent to

$$\mu^{ol}_{Fe_2SiO_4} = \mu^{o\,ol}_{Fe_2SiO_4} + 2RT \ln X^{ol}_{Fe_2SiO_4} + 2RT \ln \gamma^{ol}_{Fe_2SiO_4}, \tag{9}$$

where $2RT \ln \gamma^{ol}_{Fe_2SiO_4} = \left(1 - X^{ol}_{Fe_2SiO_4} \right)^2 2W^{(Mg,Fe)Si_{0.5}O_2}_{Mg-Fe}. \tag{10}$

Solving for γ,

$$\gamma^{ol}_{Fe_2SiO_4} = e^{\left[\frac{\left(1 - X^{ol}_{Fe_2SiO_4}\right)^2 2W}{2RT} \right]} = 1.36. \tag{11}$$

Now $a^{ol}_{Fe_2SiO_4} = \left(X^{ol}_{Fe_2SiO_4} \gamma^{ol}_{Fe_2SiO_4} \right)^2 = 0.0162$ and $\log a^{ol}_{Fe_2SiO_4} = -1.79.$ (12)

Plugging the values from equations (5),(6), and (12) into equation (4) yields

$$\log fO_2 = 5.50 - \frac{26716.6}{1598} + \frac{0.0656(10000-1)}{1598} + 2\log a^{ol}_{Fe_2SiO_4} - 2\log a^{alloy}_{Fe} - 2\log a^{opx}_{Fe_2SiO_6}$$

$$= -9.21.$$

To compare to standard oxygen buffers, I calculated $\log fO_2$ at the quartz-magnetite-fayalite buffer (QFM) according to the formula given by Huebner (1971):

$$\log fO_2 = 9.00 - \frac{25738}{T} + 0.050\left(\frac{P-1}{T}\right) = -6.79 \tag{13}$$

So according to this method, experiment #25 had an oxygen fugacity approximately equivalent to QFM-2.4 log units.

Calculation of oxygen fugacity following Gudmundsson and Holloway (1993)

The second method of fO_2 calculation is quite similar to the first, but the authors developed their own activity-composition model for Fe-Pt alloy and chose slightly different solution models for ol and opx, namely the activity expression for ol from Wiser and Wood (1991) and the slightly non-ideal mixing model for opx from Ghiorso et al. (1983). The relevant equation is Equation 17 in their paper:

$$\log fO_2 = 7.644 - \frac{29874}{T} + 0.051\left(\frac{P-1}{T}\right) + 4\log a^{ol}_{FeSi_{0.5}O_2} - 2\log a^{opx}_{FeSiO_3} - 2\log a^{Fe-Pt}_{Fe} \tag{14}$$

For olivine Wiser and Wood (1991) recommend a regular solution model to relate activities to compositions in the binary $MgSi_{0.5}O_2$-$FeSi_{0.5}O_2$ with mixing on one site and a value for W of 3.7 kJ/mol.

For a regular solution with mixing on one site,

$$a^{ol}_{FeSi_{0.5}O_2} = X^{ol}_{FeSi_{0.5}O_2}\, \gamma^{ol}_{FeSi_{0.5}O_2}. \tag{15}$$

The expression for the chemical potential of pure fayalite in olivine is:

$$\mu^{ol}_{FeSi_{0.5}O_2} = \mu^{\circ ol}_{FeSi_{0.5}O_2} + \mu_{ideal} + \mu_{excess}, \tag{16}$$

which for a regular solution with mixing on one site is

$$\mu^{ol}_{FeSi_{0.5}O_2} = \mu^{\circ ol}_{FeSi_{0.5}O_2} + RT\ln X^{ol}_{FeSi_{0.5}O_2} + RT\ln \gamma^{ol}_{FeSi_{0.5}O_2}, \tag{17}$$

where $RT\ln \gamma^{ol}_{FeSi_{0.5}O_2} = \left(1 - X^{ol}_{FeSi_{0.5}O_2}\right)^2 W^{(Mg,Fe)Si_{0.5}O_2}_{Mg-Fe}.$ (18)

Solving for γ,

$$\gamma^{ol}_{FeSi_{0.5}O_2} = e^{\left[\frac{\left(1-X^{ol}_{FeSi_{0.5}O_2}\right)^2 W}{RT}\right]} = 1.26. \tag{19}$$

Now $a^{ol}_{FeSi_{0.5}O_2} = X^{ol}_{FeSi_{0.5}O_2} \gamma^{ol}_{FeSi_{0.5}O_2} = 0.117$ and $\log a^{ol}_{FeSi_{0.5}O_2} = -0.931$.   (20)

For opx, Ghiorso et al. (1983) use a slightly non-ideal mixing model which takes into account the distribution of Mg, Fe, and other cations in the three possible sites in opx. Using their equations, which are not reproduced here, I calculated an activity of $FeSiO_3$ in the opx of experiment #25 of 0.079. This is somewhat less than the ideal mixing activity of 0.088 calculated above. $\log a^{opx}_{FeSiO3} = -1.102$.   (21)

Gudmundsson and Holloway (1993) provide an equation for computing the activity of Fe in Fe-Pt alloy based on experiments they conducted at 1300° and 1400°C and at 1 atm and 20 kbar:

$$\log \gamma^{Fe-Pt}_{Fe} = (1 - X_{Fe})^2 [B + C(4X_{Fe} - 1)]$$ (22)

Values are given for the coefficients B and C at 1300° and 1400°C, which I used to estimate values for B and C at 1325°C by linear interpolation. I determined that use of the values of B and C at 1300° and 1400°C would have resulted in a value of $\log fO_2$ higher by 0.13 or lower by 0.39, respectively. Using B=-4.046 and C=-0.2803,

$\log \gamma^{Fe-Pt}_{Fe} = -1.503$ and $\log a^{Fe-Pt}_{Fe} = -1.898$.   (23)

Now equation (14) can be solved for $\log fO_2$:

$$\log fO_2 = 7.644 - \frac{29874}{1598} + 0.051\left(\frac{10000-1}{1598}\right) + 4(-0.931) - 2(-1.102) - 2(-1.898)$$

$$= -8.46, \text{ or approximately QFM-1.7.}$$ (24)

Comparison with estimates of oxygen fugacity in the MORB source region

The estimated oxygen fugacity in my 1325°C experiment compares favorably with estimates of mantle fO_2 in several published studies (e.g., Eggler, 1983; Christie et al., 1986; O'Neill and Wall, 1987; Mattioli and Wood, 1988; Mattioli et al., 1989; Bryndzia and Wood, 1990). For example, O'Neill and Wall (1987) calculated mantle oxygen fugacity based on coexisting olivine, orthopyroxene, and spinel in peridotite xenoliths from Western Europe. They estimated that fO_2 lies between the QFM and wüstite-

magnetite buffer curves and that the absence of nickel metal in upper mantle samples indicates that fO_2 must be more oxidizing than the iron-wüstite buffer, which coincides with the nickel metal precipitation curve at relevant conditions. Similarly, Mattioli et al. (1989) calculated oxygen fugacity for a worldwide suite of peridotite xenoliths based on the coexistence of olivine, orthopyroxene, and spinel, using a slightly different solution model for Fe^{3+} in spinel than that used by O'Neill and Wall (1987). They estimated mantle fugacity at 15 kbar to be QFM±2 log units. Bryndzia and Wood (1990) carried out a similar exercise for abyssal peridotite samples and calculated an average value of QFM-0.9 log units. In contrast to the studies mentioned thus far, Christie et al. (1986) measured oxygen fugacity in fresh MORB glasses by determining the Fe^{3+}/Fe^{2+} ratio with a combination of analytical techniques and found that the oxygen fugacity recorded in MORB glasses is slightly below (1 or 2 log units) the QFM buffer. Cores of pillow lava samples and whole rocks yielded slightly more oxidizing results, which the authors attributed to hydrogen loss just before or after eruption. They note that MORB lavas appear to be more reduced than samples from other terrestrial volcanic environments. They consider their measured oxygen fugacity to be a maximum value for the MORB source region. The last two studies cited here are likely to be most relevant for determining the oxygen fugacity where MORB primary magmas form. Figure 3A-1 shows a summary of the results from those studies with the two values of oxygen fugacity calculated for sample #25. In summary, the calculated oxygen fugacity in my experimental charge at 1325°C is in good agreement with multiple estimates of the redox state of the upper mantle where partial melting of depleted peridotite occurs.

Figure 3A-1. Bar graph showing distribution of calculated oxygen fugacities from Bryndzia and Wood (1990) for abyssal peridotites and Christie et al. (1986) for MORB glasses. The plot shows number of samples versus deviation from the QFM buffer. The values for sample #25 are slightly lower than the average values for the two published studies, but since those values are considered to be maxima, sample #25 is considered to be in good agreement with oxygen fugacity estimates for the MORB source region.
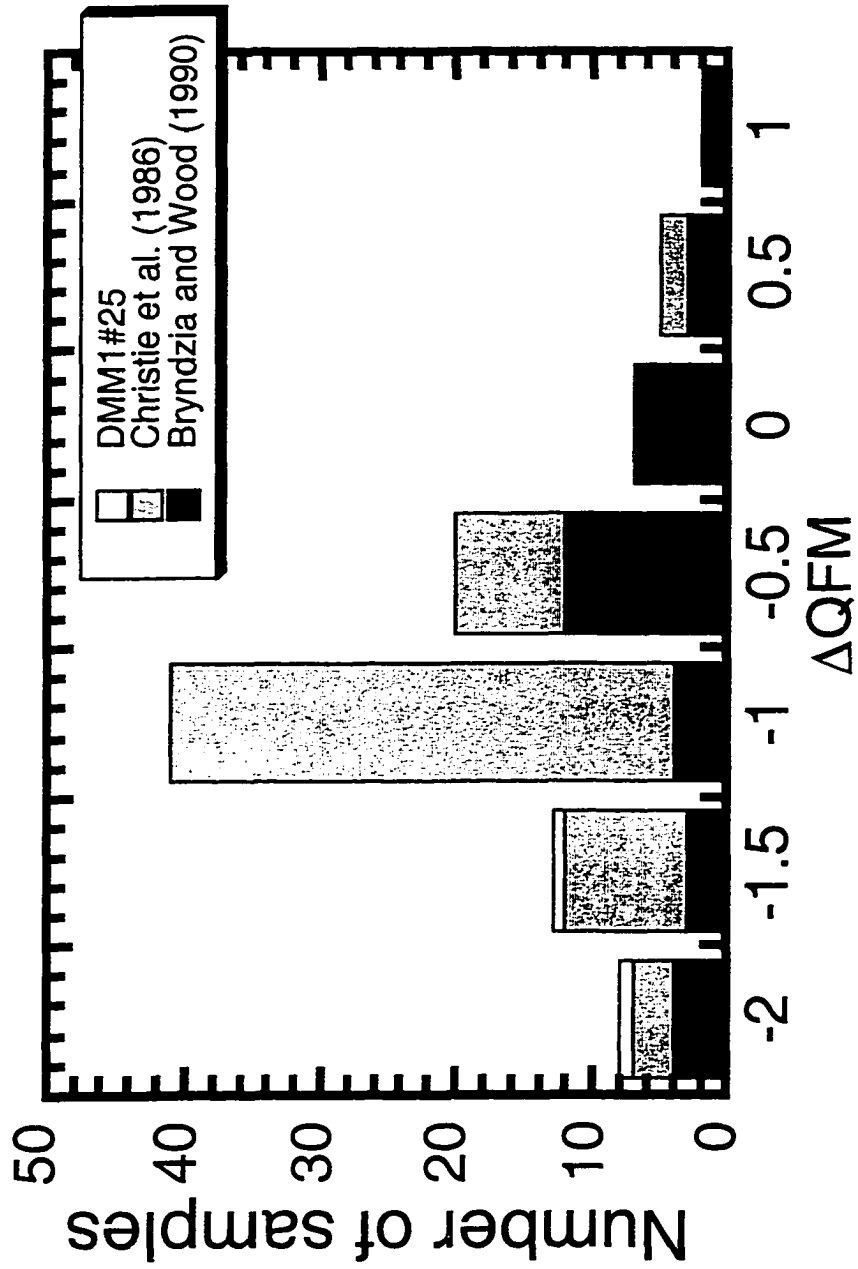
Chapter 4: Discussion of results and implications for MORB petrogenesis

The effects of bulk composition on 10 kbar near-solidus peridotite partial melts

Partial melts generated from depleted peridotite differ in several important ways from partial melts of fertile peridotite. Figure 4-1 illustrates some of these differences by comparing liquid compositions from this study to experimental results on more fertile peridotite compositions, including the 10 kbar partial melts of mm3 (Baker and Stolper, 1994; Baker et al., 1995; Hirschmann et al., 1998a), Hawaiian pyrolite and Tinaquillo lherzolite (Jaques and Green, 1980), KLB-1 and HK-66 (Hirose and Kushiro, 1993), and PHN1611 (Kushiro, 1996). All of the data are plotted as a function of melt fraction.

Figure 4-1a compares Na_2O contents in the experimental glasses as a function of melt fraction. The alkali contents of glasses in the DMM1 experiments are quite low when compared to partial melts of more fertile peridotite. Even at very low degrees of melting (<4%), the Na_2O concentration is only ~2 wt% and K_2O contents (not shown, consult Table 3-3) remain well below 1 wt%. This is in marked contrast to partial melts of more fertile peridotite, whose alkali contents at low melt fractions are high enough in some cases to cause significant changes in melt chemistry, such as high SiO_2 contents, compatible behavior of Ti in pyroxenes, low K_D $_{Fe-Mg}$ $_{ol-liq}$ (Baker et al., 1995; Hirschmann et al., 1998a), and other effects as described below.

Between 10 and 20% melting, SiO_2 contents of the experimental glasses are all ~50 wt%. However, with decreasing melt fraction, partial melts of the fertile peridotites display an increase in silica contents, while the silica values in the DMM1 liquids and partial melts of Tinaquillo lherzolite, also depleted in alkalis relative to the other compositions, decrease with decreasing temperature (Figure 4-1b). This striking difference in silica contents of

near-solidus 10 kbar melts of fertile versus depleted peridotite reflects a substantial decrease in the activity coefficient of SiO_2 in the liquid when the alkali content is high (>5 wt%) and a corresponding increase in SiO_2 concentration in order to maintain constant SiO_2 activity and saturation with olivine and orthopyroxene (Hirschmann et al., 1998a).

Alumina contents in partial melts from all seven mantle compositions decrease with increasing melt fraction (Figure 4-1c). Close to the solidus (F<0.1), liquids produced from DMM1 contain 1-2 wt% less Al_2O_3 than melts from the more fertile bulk compositions. This difference increases to ~3 wt% Al_2O_3 at a melt fraction of ~0.17. The elevated abundances of FeO* (not shown) and MgO (Figure 4-1d) in the DMM1 melts relative to the partial melts of fertile peridotite (at the same melt fraction) are also probably due to the effects of alkalis on the relative stabilities of olivine and orthopyroxene (Kushiro, 1975; Ryerson, 1985). As illustrated in the figure, this effect occurs to a lesser extent for partial melts of Tinaquillo lherzolite.

Figure 4-1e shows the difference in CaO contents of low degree melts of depleted and fertile peridotite. Although glass CaO contents from DMM1 and the three fertile peridotite compositions define concave-downward trends, the maximum CaO values occur at very different melt fractions, corresponding to the exhaustion of cpx. As discussed above, the maximum CaO content occurs at a melt fraction between 0.08 and 0.10 for DMM1, while for the fertile peridotites the maximum CaO values occur at melt fractions greater than 0.10. Also, the maximum CaO contents in the DMM1 partial melts are 1-2 wt% higher than the maximum values displayed by the more fertile compositions, even though DMM1 has between 1 and 1.5 wt% less CaO than the fertile mantle compositions. This difference in CaO contents is most dramatic near the solidus; at F~0.02, the partial melt of DMM1 contains ~13 wt% CaO compared to ~6.5 wt% for mm3. A likely explanation for this significant difference again lies in the large difference in Na_2O contents between near-solidus depleted and fertile peridotite partial melts. At low melt fractions in a depleted

peridotite system (below cpx-out), the alkali content of the melt is low, so a relatively large proportion of Ca in the melt resides within aluminate complexes (e.g., Merzbacher and White, 1991). Since much of the Ca in the melt is bonded to aluminate groups, the activity coefficient of CaO in the melt is low, so a high concentration of CaO in the melt is required for saturation with cpx. In a fertile peridotite system, however, the alkali content of the melt is high at low melt fractions. Since Na is preferred over Ca in complexes with aluminate molecules (Navrotsky et al., 1982; Ryerson, 1985; McMillan and Wolf, 1995), relatively less Ca is bound with aluminate groups, and the activity coefficient of CaO in the melt is higher. Therefore, a smaller concentration of CaO in the melt is needed for cpx saturation.

The ratio of CaO to Al_2O_3 in the partial melts is plotted in Figure 4-1f. This ratio has often been cited as an indication of melt fraction (Niu and Batiza, 1991; Langmuir et al., 1992), but this figure clearly demonstrates that CaO/Al_2O_3 is a strong function of source peridotite composition as well as melt fraction (Hirschmann et al., 1996; Wasylenki et al., 1996).

Variations in solidus temperature, melt productivity, and melt fraction at cpx-out as functions of peridotite bulk composition

Figure 4-2 shows estimated solidus temperatures (T_s) for DMM1 and various fertile mantle compositions plotted as a function of bulk Ti+Na+K+P content (in cation %). All four of these elements are incompatible during mantle partial melting (Schairer, 1954; Anderson and Greenland, 1969; Walter and Presnall, 1994), and the ability of alkalis to substantially lower the melting point of bulk compositions in, for example, the system $CaO-MgO-Al_2O_3-SiO_2$ is well known (Walter and Presnall, 1994). For the natural compositions, T_s varies by ~110°C (1260°C, DMM1 to ~1150°C, Hawaiian pyrolite-40% olivine), while the alkali contents (Na_2O+K_2O) vary from 0.06 wt% (DMM1) to 1.17 wt%

(Hawaiian pyrolite-40% olivine). The linear relationship between incompatible oxide content and solidus temperature is consistent with a simple freezing point depression model as expressed by Denbigh (1981) and applied to a two-component system by Hirschmann et al. (1998, submitted). Applying this model to the data in Figure 4-2, the solidus temperature of a given peridotite composition at 10 kbar would be $T_s = T_0 - C_0/k$, where C_0 is $Ti+Na+K+P$, T_0 is the intercept on Figure 4-2, representing the solidus temperature of a peridotite with $C_0 = 0$ (1263°C in this case), and k is the proportionality constant (or 1/slope of the fitted line), 0.026. Based on this relationship, abyssal peridotites, which have extremely low values of C_0, might be expected to have solidus temperatures near 1263°C at 10 kbar.

An extremely important issue for modeling of MORB petrogenesis is the amount of liquid produced by partial melting of peridotite. The results from this study can be used to quantify melt productivity for depleted peridotite and, along with other experimental data from the literature, to characterize melt productivity as a function of bulk composition. Figure 4-3 shows near-solidus, isobaric melt productivity (wt% liquid/°C, or dF/dT, where F is melt fraction) for lherzolite-saturated, low-pressure partial melting of DMM1 and other experimentally-studied peridotite compositions. The independent variable in this plot is F^2/C_0, where C_0 is $TiO_2+Na_2O+K_2O+P_2O_5$ (wt%) in each bulk peridotite composition. In studies not reporting K_2O or P_2O_5 contents, these are taken to be zero. For DMM1 and the two 15 kbar points (MORB pyrolite [MPy] and Tinaquillo lherzolite[TL], Robinson et al., 1998), a linear, unweighted, least-squares fit was applied to the melt fraction-temperature data. The bars on either side of the point indicate the melt fraction interval included in the fit (in terms of F^2/C_0). Only two points each are available to calculate melt productivities for TL and TL-40 (TL-40% ol) at 10 kbar (Jaques and Green, 1980), and for PHN1611 (Kushiro, 1996) only the two lowest temperature points were used. For mm3, separate fits were made to melt fraction-temperature data from mass balance calculations

using pyroxene rim compositions and those using pyroxene core compositions. Melt

fraction-temperature data based on rim compositions were fit to an unweighted, second-

order polynomial: $F = -24.989 + 0.0368 * T - 1.345 \times 10^{-5} * T^2$, and the resulting dF/dT

points 1250°, 1270°, 1290°, 1310°, and 1330°C (plotted in the figure as diamond symbols

joined by solid line segments) are inversely correlated with F^2/C_0. Data based on pyroxene

core compositions yielded a nearly linear dF/dT relationship, whose slope is represented by

the triangle in Figure 4-3.

The experimental data described thus far define an overall negative correlation between

isobaric melt productivity and F^2/C_0. This trend suggests that melt productivity is

enhanced either by increased source fertility (C_0) or very near the solidus (low values of

F). These relationships are counter to predictions from simple thermodynamic analysis and

from calculations using MELTS (Asimow et al., 1997). For example, the dashed line in

Figure 4-3 shows MELTS calculations of melt productivity for mm3 at 10 kbar, a trend

dramatically at odds with the experimental results.

For a simple, two-component system, the theoretical relationship between near-solidus

melt productivity for isobaric batch melting, or dF/dT, and F^2/C_0 is derived by Hirschmann

et al. (1998, submitted) by combining the equation for freezing point depression above

with the batch melting equation of Shaw (1970):

$$\frac{dF}{dT} = \frac{k\left[(1 - D_o)F + D_o\right]^2}{C_o(1 - D_o)},$$ where D_0 is the bulk partition coefficient between solid and

liquid of a component present in dilute quantities. Since k, D_0, F, and C_0 are all positive

numbers, this expression clearly leads to a positive correlation between melt productivity

and F^2/C_0, as illustrated by the MELTS calculation for mm3 (dotted line in Figure 4-3). To

the extent that this simple system analysis can be applied to multi-component peridotite

melting in a qualitative fashion, Figure 4-3 indicates striking disagreement between

experimental results and theoretical or MELTS-based predictions.

The cause of the discrepancy between experimental results and calculations may be the methods by which melt fractions are determined in experimental partial melting studies. As described in Chapter 3, melt fractions in this study and in studies on the mm3 composition were determined by mass balance calculations in which a linear combination of the compositions of coexisting glass, ol, opx, cpx, and sp was sought so as to fit the bulk composition of the starting material. Rim compositions of pyroxenes are normally used for these calculations, as they most closely represent equilibrium compositions, but a consequence of this is that the mass balance equation is not truly "balanced" because the bulk starting composition includes the material within the partially-equilibrated pyroxene cores. Since cores are normally richer in incompatible elements such as Na and Ti, the mass balance calculations will result in overestimates of melt fractions. At higher melt fractions, the magnitude of the overestimation decreases because the crystalline phases within experimental charges homogenize and approach equilibrium more readily with increasing temperature and because the proportion of pyroxenes in the charges decreases. The "permissible" fit for mm3 in Figure 4-3 was constructed by drawing a smooth, concave-upward curve through melt fraction-temperature data that included results based on both rim and core pyroxene analyses on a plot of melt fraction versus temperature. The squares with crosses in Figure 4-3 represent the slopes of tangents to this curve at various melt fractions, and they define a trend that is consistent with theoretical and MELTS-based predictions.

For fertile mantle compositions, cpx-out occurs at melt fractions of ~0.2. However, for DMM1, cpx-out occurs at a much lower melt fraction (0.08-0.10). Figure 4-4 compares melt fractions at cpx-out to the normative cpx content in the bulk compositions of eight peridotites. With the exception of HK-66, which plots above the trend defined by the remaining seven compositions, the data display a positive correlation between the amount of melting required to exhaust cpx at 10 kbar and the normative amount of cpx in the

source. This is not an unexpected result and is entirely consistent with the results of

MELTS calculations as shown by the two dashed lines in Figure 4-4. To construct these

dashed lines, increments of cpx were added or subtracted from the compositions of mm3

(KBH cpx, Table 3-1, Baker and Stolper, 1994) and DMM1 (subsolidus cpx composition

from run #36, Table 3-3). The melt fraction at cpx-out at 10 kbar for each of the new bulk

compositions was then determined using MELTS (individual points are not plotted because

correlation coefficients are >0.99). Note that the three fitted lines all indicate normative cpx

of ~0.04 at a melt fraction of zero. This reflects the dissolution of a small amount of

normative cpx in residual opx. The large suite of abyssal peridotites whose compositions

were determined by Baker and Beckett (1998) have normative cpx contents ranging from

0.02 to 0.10. The correlation illustrated in Figure 4-4 suggests that if these rocks remained

in an appropriate upper mantle thermal regime, they could experience an additional amount

of melting from 0 to 13% before the exhaustion of cpx. Beyond the exhaustion of cpx,

very little additional melting would be expected, since melt productivity is estimated to

decrease by a factor of about four once cpx is gone (Hirschmann et al., 1998, submitted).

Comparison of experiments and models/calculations

In the past several years several different approaches to calculating the compositions

and amounts of partial melts of peridotite have appeared in the literature (e.g., McKenzie

and Bickle, 1988; Niu and Batiza, 1991; Kinzler and Grove, 1992ab; Langmuir et al.,

1992; Ghiorso and Sack, 1995). These methods were calibrated with experimental data on

fertile peridotite melting, and it was not known how well the models perform in areas of

composition space other than those where previous experimental data exists. The present

experiments can be used to evaluate how well the various models can predict the

compositions and amounts of liquids produced by partial melting of depleted peridotite.

Figure 4-5 shows a comparison of liquid compositions calculated by some of the models

and those produced in the actual experiments. Concentrations of selected oxides are plotted as a function of melt fraction.

The MELTS program (Ghiorso and Sack, 1995) calculates equilibrium phase assemblages and compositions of liquids and solids that will coexist at conditions relevant to mantle melting by minimizing thermodynamic energy functions. Because the experiments reported in this study were not used in the calibration of MELTS, the program gives an independent prediction of the amounts and compositions of liquids which will result from isobaric batch melting of the DMM1 composition at 10 kbar. Absolute concentrations of some oxides, particularly MgO and SiO_2, are offset by as much as 2 to 3 wt% due to the overstabilization of opx by MELTS, but the shapes of trends for all oxides except FeO* are remarkably similar. The increase in FeO* following cpx- and sp-out is overestimated. MELTS predicts that the drop in TiO_2 and rise in SiO_2 seen in the near-solidus experiments of Baker and Stolper (1994) and Baker et al. (1995) will occur in this system at extremely low melt fractions (F~0.005), when alkali concentrations reach appropriate levels to cause such effects (Baker et al., 1995; Hirschmann et al., 1998a). MELTS predicts CaO contents of melts near cpx-out higher than those found in the experiments, up to a maximum of 15.3%, compared to 13.9% for DMM1 experiments. The melt fraction at which cpx-out and the CaO maximum is slightly higher in the MELTS calculation (F=0.07, instead of ~0.09).

The model of Kinzler and Grove (1992a) uses data from many experiments on partial melting of fertile peridotite to calculate a melting reaction for spinel lherzolite. The major element compositions of partial melts can be predicted, given an initial peridotite composition, pressure, melt fraction, and Mg# of the partial melts. The model applies to melting only below cpx-out. An updated version of the Kinzler and Grove (1992a) program (Kinzler, 1997) was used to calculate partial melt compositions for batch melting of DMM1 at 10 kbar; these compositions are plotted in Figure 4-5. The melting reaction

determined in Chapter 3 for DMM1 at 10 kbar as well as the mode from the subsolidus run were entered into the program, and partial melt compositions for melting at 10 kbar from 0.5% to 12.5% melting were calculated. At melt fractions greater than ~4%, the predicted trends for major element oxides are close to the experimental results. Some oxides match extremely well, such as Cr_2O_3 and CaO. Others have curves which match the experiments in shape, but are offset in value. Specifically, MgO and FeO* are slightly overestimated, and Na_2O and TiO_2 are slightly underestimated compared to the experimental trends. Below 4% melting, the model calculations deviate substantially from the experimentally determined melt compositions, predicting a dramatic rise in SiO_2 and Al_2O_3 (51% and 23% at 2% melting, respectively) and decrease in FeO* and MgO (4.6% and 7.4% at 2%, respectively), indicating that the model is not well-calibrated for near-solidus partial melting of peridotite that is significantly different from the compositions used in the parameterization. It is in part the goal of this study to provide experimental data on depleted peridotite melting that can be incorporated into models such as developed by Kinzler and Grove (1992a) and Kinzler (1997) in order to increase the models' flexibility and accuracy in predicting partial melt compositions.

Langmuir et al. (1992) predict liquid compositions for melting above and below cpx-out in terms of Na_2O, MgO, TiO_2, and FeO* by using constraints on distribution coefficients from a large experimental data set. The advantage of this approach is that it can be applied to a wider range of source peridotite compositions. The calculated trends are shown in Figure 4-5. The curves match the experiments very well for all oxides modeled. Na_2O is slightly underestimated, as in all the models discussed, but is very close, given the uncertainties on the composition of DMM1. There is a slight offset towards higher TiO_2. This model gives the best match to both the abundances and shapes of the trends for FeO and MgO, but does not predict the rise in Na_2O and drop in TiO_2 predicted at extremely low melt fractions by MELTS.

Implications for MORB petrogenesis

An important issue to consider is where in the upper mantle the composition of DMM1 is relevant to generation of MORB primary magmas. In order to constrain the pressures at which upper mantle peridotite undergoing decompression melting might resemble DMM1, I used two of the models discussed above to calculate the amounts of melt and compositions of residue from polybaric, fractional melting of the primitive upper mantle composition of McDonough and Sun (1995). The first set of calculations, using the program of Langmuir et al. (1992), is presented in Figure 4-6. Since the depth at which melting begins is believed to vary from place to place beneath ridges (Klein and Langmuir, 1987; Langmuir, et al., 1992), I performed a series of calculations with different pressures at the solidus, ranging from 30 kbar to 15 kbar. The productivity function in the Langmuir et al. (1992) model is taken to be linear, so the cumulative amount of melt produced as a function of decreasing pressure is linear in Figure 4-6. I inspected the calculated residue compositions for each starting pressure to determine where the residue is most similar to DMM1. While there is no perfect match to DMM1 in the calculated residue compositions, the Na_2O, TiO_2, and SiO_2 contents generally matched DMM1 best at similar pressures; thus Na_2O was chosen as the criterion for determining the pressure where the residue most closely matched DMM1. If MgO were chosen instead, the pressures at which DMM1-like residue occurs would be somewhat lower, ranging from 16 kbar for a 30 kbar onset of melting to 2 kbar for a 15 kbar onset. Diamond symbols in Figure 4-6 indicate the pressures and cumulative melt fractions where the solid residues resemble DMM1 for the different solidus pressures; these values range from 9.4% melting at 22 kbar for a 30 kbar solidus to 7.0% melting at 8.5 kbar for a 15 kbar solidus. The total amount of liquid produced ranges from 30% to 13% (melting is assumed to cease at a pressure of 3 kbar), thus the liquid produced by polybaric, fractional melting comprises a substantial contribution (as much as one-half or

two-thirds of the total liquid) from peridotite as depleted as DMM1 or more so,

emphasizing the importance of partial melts from depleted peridotite in generation of

MORB primary liquids.

The model of Asimow et al. (1997) was used to perform a similar calculation based on

MELTS (Ghiorso and Sack, 1995). In this case the onset of melting is determined by the

entropy of the system, or the mantle potential temperature (McKenzie, 1984). The melt

productivity function is not assumed to be linear, but is calculated by enthalpy minimization

at constant system entropy. The results of these calculations are illustrated in Figure 4-7.

Figure 4-7a is a plot of cumulative melt fraction versus pressure with curves for different

mantle potential temperatures ranging from 1396° to 1300°C. Diamond symbols indicate

where the residues of polybaric, fractional melting most closely match DMM1. Again the

calculated residues do not perfectly match the composition of DMM1, but CaO content,

TiO_2 content, and cpx mode match DMM1 at similar pressures, so TiO_2 was chosen as the

matching criterion. The cumulative melt fractions at which DMM1-like peridotite occurs

are just slightly higher (~12-14%) than those in the Langmuir et al. (1992) calculation, but

the corresponding pressures are quite different. This is due to the long, low-productivity

"tails" near the solidus in the model of Asimow et al. (1997). Figure 4-7b shows

instantaneous melt fraction produced at each decrement in pressure as a function of

pressure. As concluded in Asimow et al. (1997), the amount of melt generated at each step

is not constant or decreasing with decreasing pressure, but increasing until cpx is

exhausted, at which point productivity drops dramatically. Residue compositions

resembling DMM1 occur very near the crest of the instantaneous melt fraction curves for all

mantle potential temperatures, implying that regardless of the mantle potential temperature,

DMM1-like peridotite can be expected to contribute a relatively large amount of liquid to an

aggregate primary liquid. Indeed the model calculations predict that ~45% of the total

liquid generated between solidus and 3 kbar will be partial melt generated from peridotite as depleted as DMM1 or more so, regardless of mantle potential temperature.
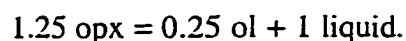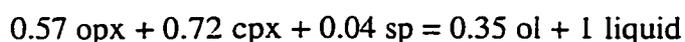
That partial melts of depleted peridotite make a substantial contribution to MORB primary magmas is apparent from Figure 4-8. Low degree partial melts of fertile peridotite at high pressures (Kushiro, 1996; Walter, 1998) and low degree partial melts of depleted peridotite at low pressure (this study) are plotted in oxide variation diagrams. The fields in the figure represent primitive MORB (Elthon, 1990) and primitive MORB compositions corrected for low pressure fractionation of olivine and spinel (Presnall and Hoover, 1978). Arrows indicate the direction in which the compositions move with addition of olivine and spinel. MORB primary magmas are most likely formed by mixing of low degree melts generated over a range of pressures (e.g., Klein and Langmuir, 1987; McKenzie and Bickle, 1988; Kinzler and Grove, 1992; Langmuir et al., 1992). From these plots the mixing proportions required to generate the corrected MORB compositions can be roughly estimated. The corrected MORB compositions, expected to be similar to primary MORB liquids, lie generally between the 25 kbar partial melts of fertile peridotite and 10 kbar partial melts of depleted peridotite, suggesting that a large proportion of aggregate liquids is contributed by melting of depleted peridotite at relatively low pressures. This is consistent with the productivity patterns calculated by Asimow et al. (1997).

Conclusions

I have presented an experimental study of partial melting of peridotite depleted in incompatible major elements at 10 kbar pressure and temperatures from 1250° to 1390°C. The chosen peridotite composition is substantially more depleted in incompatible components than peridotites in previous experimental studies. I have made use of aggregates of vitreous carbon, which extract or segregate melt from the bulk sample and enable quenching of the partial melt to a glass free of quench crystals. Aggregate extraction

experiments have been somewhat controversial in the literature, but I have demonstrated

that our experiments have approached equilibrium closely with reversals and excellent

reproducibility in a large number of experiments using several variants of the extraction

technique.

The compositions of our experimental glasses define smooth trends in major oxide

variation diagrams; TiO_2, Al_2O_3, and Na_2O concentrations decrease with increasing degree

of melting while MgO, SiO_2, Cr_2O_3, and FeO* concentrations increase. CaO content

increases while clinopyroxene is present in the residue, then decreases at temperatures

above cpx exhaustion, which occurs between 1300° and 1310°C. Spinel-out also occurs

within this temperature interval. Phase proportions calculated by mass balance indicate that

melt productivity is ~0.11%/°C while cpx and spinel are still present, then somewhat lower

(0.07%/°C). Extrapolation of the melt fraction versus temperature curve to a melt fraction

of zero yields an estimated solidus of 1260°C. Melting reactions were determined by linear

fit to crystalline phase proportions as a function of melt fraction both below and above cpx-

out to be as follows:

0.57 opx + 0.72 cpx + 0.04 sp = 0.35 ol + 1 liquid

1.25 opx = 0.25 ol + 1 liquid.

When compared to results of partial melting experiments on fertile peridotite, our results

show that alkali contents are significantly lower in partial melts of depleted peridotite. Even

at 2-3% melting, Na_2O content is only about 2 wt%. As a result of the low alkali contents

of partial melts of DMM1, SiO_2 contents of those melts are lower at low melt fractions than

in partial melts of fertile peridotite. In addition, CaO contents of partial melts of depleted

peridotite are higher, even though fertile source peridotites usually have substantially more

CaO than depleted source rocks. CaO/Al_2O_3 is also higher at a given melt fraction for

depleted peridotite melting, implying that this ratio is a function not only of melt fraction,

but of source composition as well.

Our results indicate that the bulk compositions of peridotite affect peridotite solidus temperatures, melt productivity, and melting reactions. Solidus temperatures of various peridotite compositions studied at 10 kbar define a strong, linear correlation with Ti+Na+K+P. Isobaric melt productivity appears from experimental studies to be negatively correlated with melt fraction and positively correlated with source fertility, in contrast to theoretical expectations and calculations using the MELTS algorithm of Ghiorso and Sack (1995). The discrepancy is likely due to the procedure used to determine melt fraction in partial melting experiments. Results also indicate that the melt fraction at which cpx is exhausted from the residue during partial melting is linearly correlated with normative cpx content of the source peridotite. This is corroborated by MELTS calculations of cpx-out for the DMM1 and mm3 (Baker and Stolper, 1994) compositions with increments of cpx added or subtracted.

The results of our experiments allow assessment of how various methods of calculating partial melt compositions perform when the source peridotite is depleted. While offset in temperature, MgO, and SiO_2, the MELTS program reproduces the shapes of oxide trends defined by our experiments quite well. MELTS predicts that the chemical effects caused by high alkali contents in previous low degree melting experiments on fertile peridotite will occur only below 0.5% melting in this system. The model of Kinzler and Grove (1992a) also reproduces the trends well at melt fractions >4%, but deviates from the experimental results at lower melt fractions. The algorithm of Langmuir et al. (1992) successfully reproduces the experimentally-determined trends quite well.

The models of Langmuir et al. (1992) and Asimow et al. (1997) can be used to predict the pressures at which an initially fertile source peridotite reaches a composition similar to that of DMM1, given different pressures of onset of melting or different mantle potential temperatures. Both models predict that about half of the liquid produced in the melting column will be small degree partial melts of peridotite as depleted or more depleted than

DMM1. In addition, the algorithm of Asimow et al. (1997) predicts extremely high melt productivity at the pressures where compositions similar to that of DMM1 are the relevant source rock. Thus partial melts of depleted peridotite make a large and potentially important contribution to liquids parental to MORB, as demonstrated by comparing the compositions of partial melts of depleted peridotite and high pressure melts of fertile peridotite to MORB compositions corrected for low-pressure fractionation.

Figure 4-1. Glass compositions from DMM1 experiments (this study) and from

experimental studies on fertile mantle compositions versus calculated melt fraction (F). All

experiments were conducted at a nominal pressure of 10 kbar. Circles represent glass

compositions from the two-stage experiments; triangles represent glass compositions from

the temperature reversal runs; diamonds are compositional convergence experiments (see

Chapter 3 for explanation of these different types of experiments). Error bars are 1σ; if not

shown, error bars are smaller than the symbols. Filled symbols represent glass coexisting

with ol, opx, cpx, and sp; open symbols represent glass coexisting with ol and opx. The

melting trends for the fertile peridotite compositions are represented by smooth curves

through the data points of each study: dotted line is mm3 (Baker and Stolper, 1994; Baker

et al., 1995; Hirschmann et al., 1998a); solid line is Hawaiian pyrolite (HPy), and long

dash is Tinaquillo lherzolite (Jaques and Green, 1980); medium dash is KLB-1, and short

dash is HK-66 (Hirose and Kushiro, 1993); dot-dash is PHN1611 (Kushiro, 1996). (a)

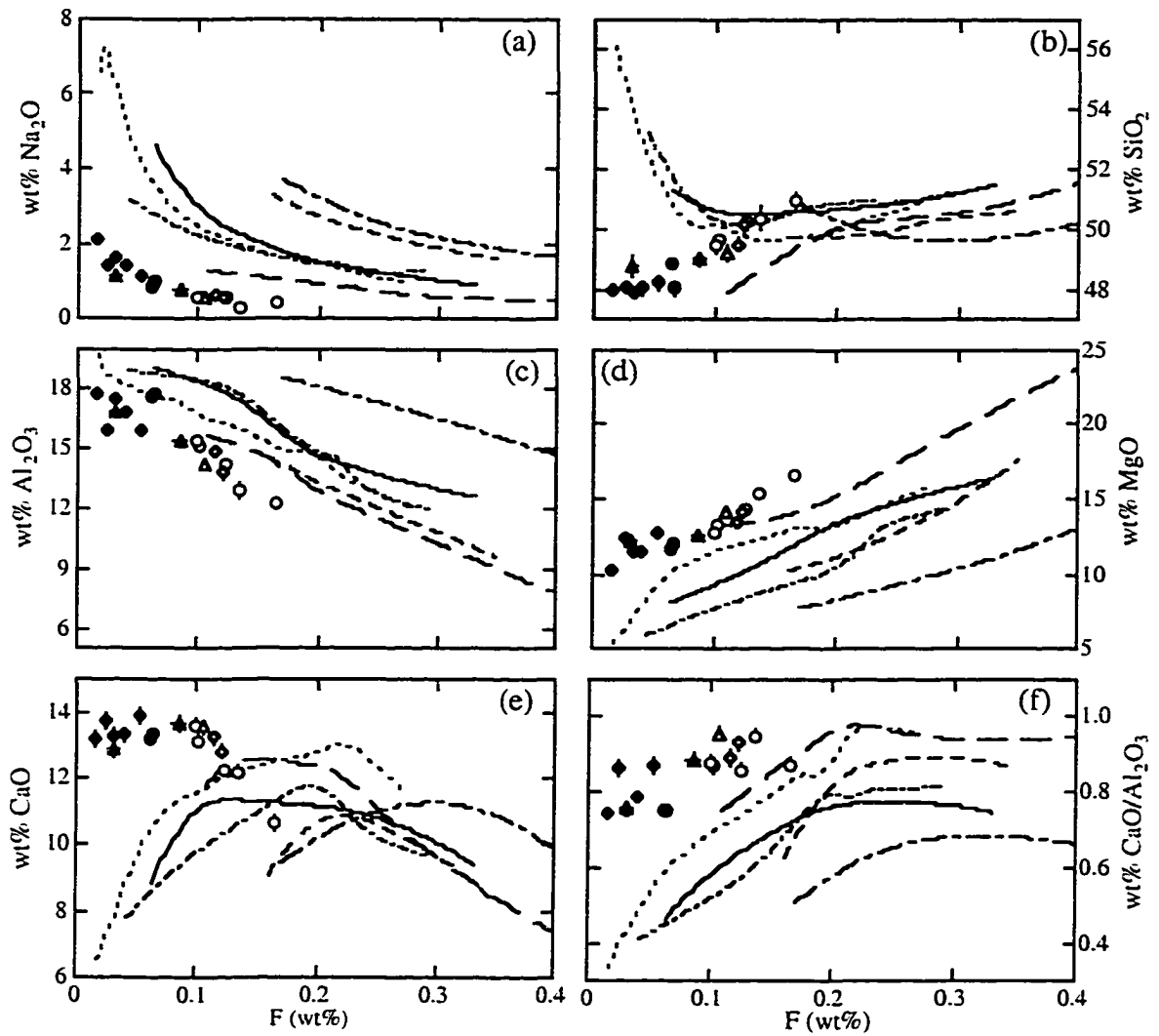Na_2O-F, (b) SiO_2-F, (c) Al_2O_3-F, (d) MgO-F, (e) CaO-F, (f) CaO/Al_2O_3-F.

Figure 4-2. Solidus temperature (T_S) versus bulk Ti+Na+K+P in cation% for various

peridotite compositions at 10 kbar: DMM1 (this study), mm3 (Baker and Stolper, 1994),

KLB-1 (Takahashi, 1986), HK-66 (Takahashi and Kushiro, 1983), TL=Tinaquillo

lherzolite, and HPy=pyrolite (Jaques and Green, 1980), PHN1611 (Kushiro, 1996). For

DMM1, KLB-1, and HK-66, the solidus temperatures are taken to lie midway between

liquid-absent and liquid-present experiments, and the error bars denote this temperature

range for each bulk composition. For mm3 and PHN1611, the solidus temperature was

calculated by extrapolating a linear fit to temperature-melt fraction data; here the error bars

represent an estimate of the uncertainty associated with the extrapolation. For the

remaining compositions, the 10 kbar solidus temperatures are taken from published P-T

phase diagrams (T_S for Tinaquillo lherzolite is not well-constrained). The solid line is an

unweighted least-squares fit to the data; T_S for PHN1611 was not included in the fit. At the

same melt fractions, the 15 and 30 kbar data of Kushiro (1996) are at much lower

temperatures than high pressure experimental data of Wendlandt and Mysen (1980) and

Harrison (1981) on the same bulk composition. Although the temperatures reported by

Kushiro (1996) appear to be internally consistent, they may be 50-100°C low compared to
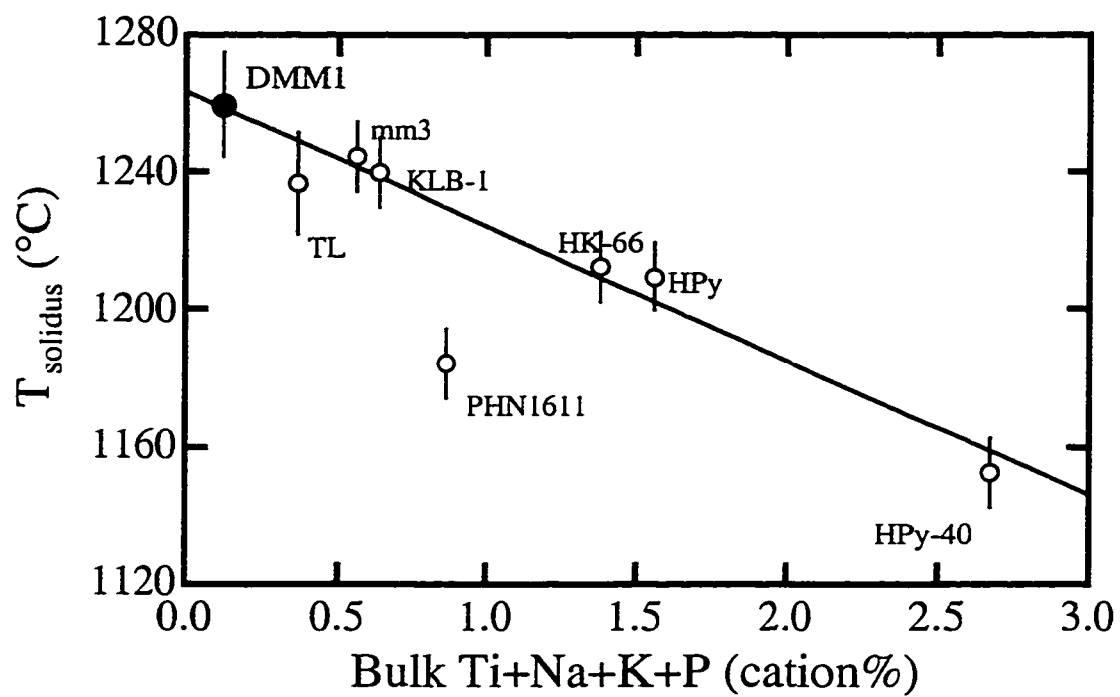
other experimental data on PHN1611.

Figure 4-3. Isobaric melt productivity (wt% melt generated per °C) for DMM1 and several

fertile mantle compositions plotted against F^2/C_o, where F is melt fraction and C_o is

$TiO_2+Na_2O+K_2O+P_2O_5$ (wt%) in the bulk peridotite. Where not reported, K_2O and P_2O_5

are taken to be zero. All liquids are ol+opx+cpx±sp±plag-saturated. For DMM1 and the

two 15 kbar points (MORB pyrolite [MPy] and Tinaquillo lherzolite[TL], Robinson et al.,

1998), a linear, unweighted, least-squares fit was applied to the temperature-melt fraction

data. The bars on either side of the point indicate the melt fraction interval included in the

fit (in terms of F^2/C_o). Only two points each are available to calculate melt productivities

for TL and TL-40 (TL-40% ol) at 10 kbar (Jaques and Green, 1980), and only the two

lowest temperature points were used for PHN1611 (Kushiro, 1996). For mm3, separate

fits were made to melt fraction-temperature data from mass balances using pyroxene rim

compositions and those using pyroxene core compositions. Melt fraction-temperature data

based on rim compositions were fit to an unweighted, second-order polynomial: F =

$-24.989 + 0.0368 * T - 1.345 \times 10^{-5} * T^2$, and the resulting dF/dT points (plotted in the

figure as diamond symbols joined by solid line segments) are inversely correlated with

F^2/C_o. Data based on pyroxene core compositions yielded a linear dF/dT relationship

(triangle). The "permissible" fit was constructed by drawing a smooth, concave-upward

curve through melt fraction-temperature data for rim and core pyroxene analyses on a plot

of melt fraction versus temperature. The points plotted on this figure represent the slopes

of tangents to this curve at various melt fractions. The dashed line shows the calculated
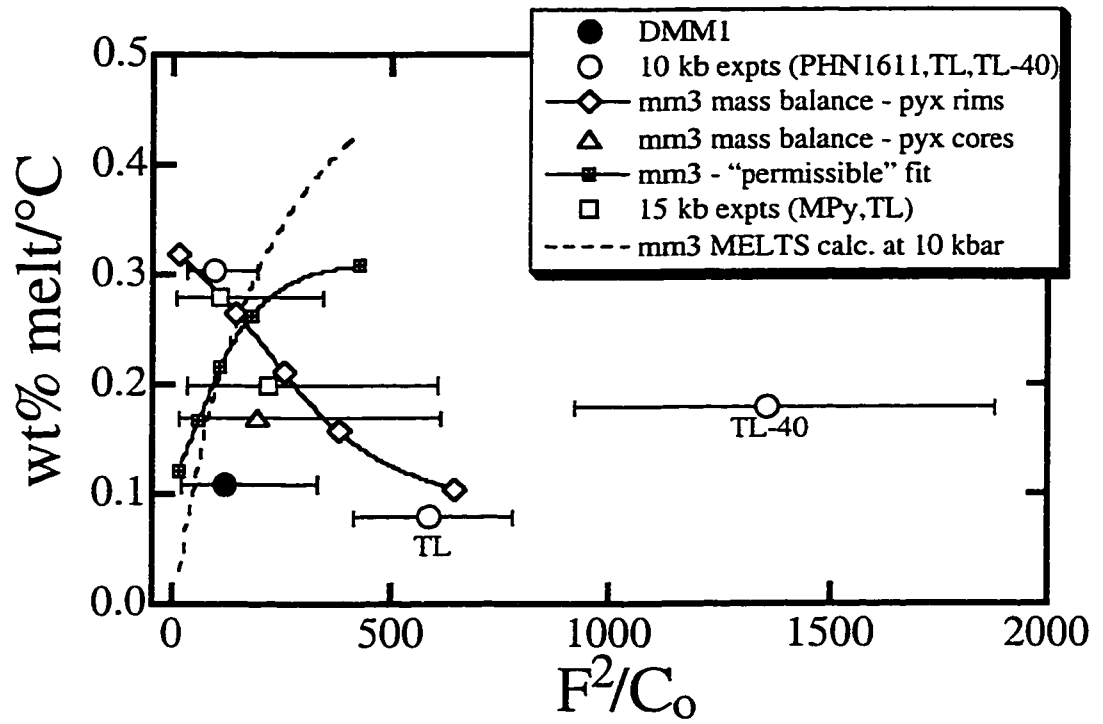
dF/dT for mm3 from MELTS (10 kbar).

Figure 4-4. Melt fraction at cpx-out (by weight) versus normative cpx in the bulk

compositions. Filled circle is DMM1 (this study); other labels are HK-66 and KLB-1

(Hirose and Kushiro, 1993), mm3 (Baker and Stolper, 1994; Baker et al., 1995;

Hirschmann et al., 1998a), MPy (Robinson et al., 1998), TL-40 and HPy-40 (Jaques and

Green, 1980), PHN1611 (Kushiro, 1996). Triangles represent studies conducted at 5

kbar, circles 10 kbar, and squares 15 kbar. For a given bulk composition, the error bars

denote the difference in melt fraction between cpx-present and cpx-absent experiments;

where not shown, this difference is smaller than the symbol. Heavy solid line is an

unweighted, least-squares fit to the data (the 10 kbar HK-66 point was excluded from the

fit). The long dash shows the result of MELTS calculations on mm3 with increments of

cpx (KBH cpx, see Table 3-1) added or subtracted from the bulk composition. The short

dash shows result for MELTS calculations on DMM1±cpx (cpx from subsolidus
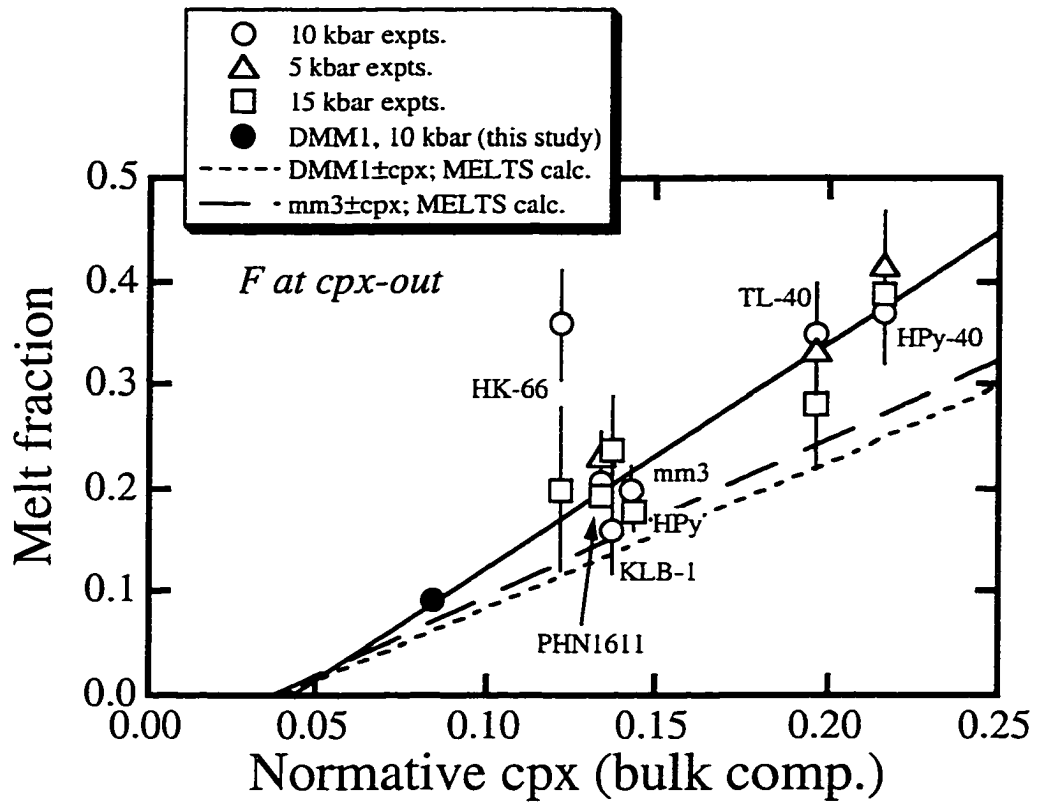
experiment #36, see Table 3-3).

Figure 4-5. Comparison of experimental results to model calculations. Point symbols as in Figure 1 with 1σ error bars. Solid line is MELTS calculation (Ghiorso and Sack, 1995). A similar comparison between MELTS calculations and a subset of these experimental data was previously presented by Hirschmann et al. (1998b). Long dash is Kinzler and Grove (1992). Short dash is Langmuir et al. (1992).
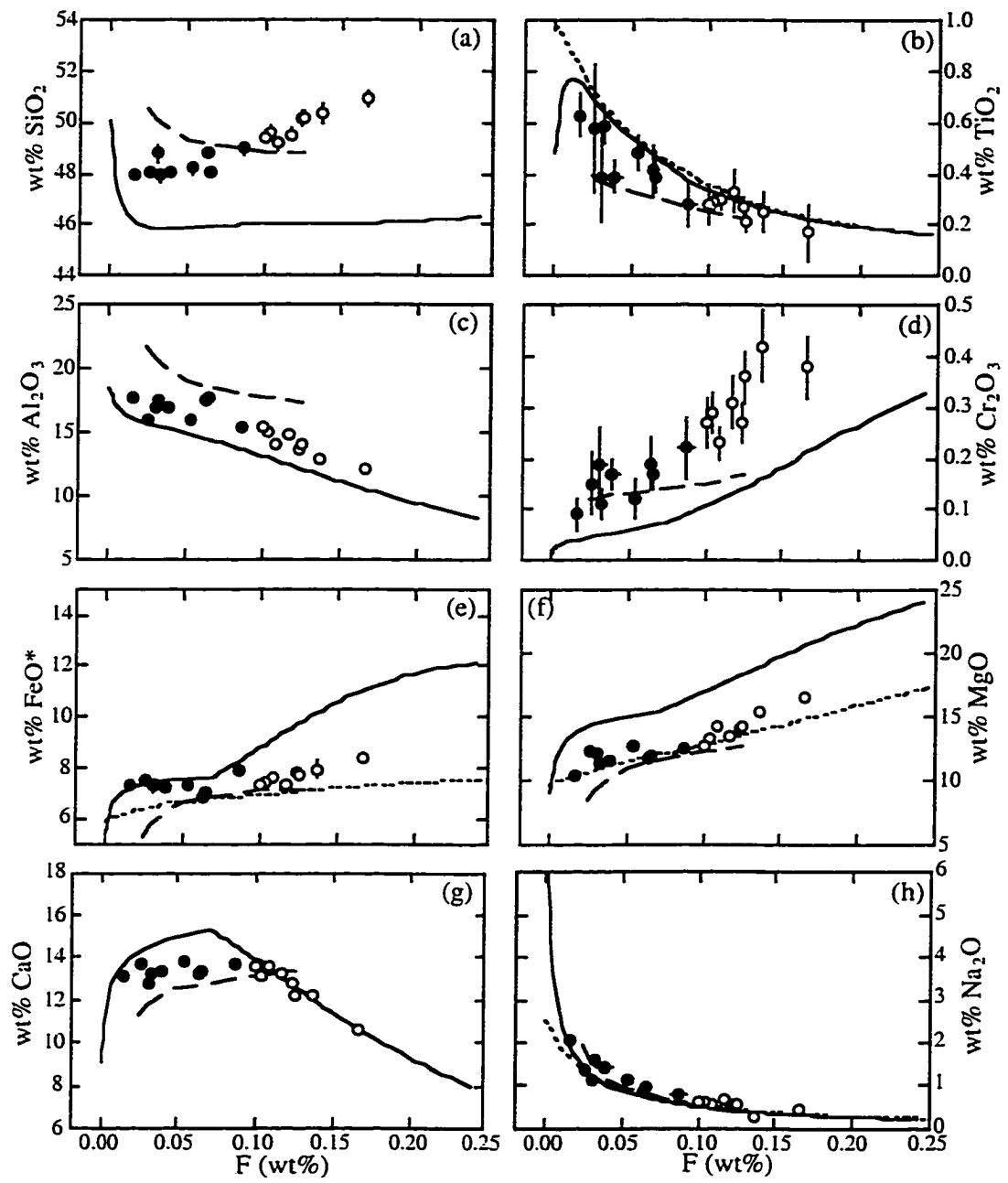
Figure 4-6. Calculations using the algorithm of Langmuir (1992) of the pressures and melt

fractions at which residues from polybaric, fractional melting of fertile peridotite most

closely resemble the composition of DMM1. The initial composition is the primitive mantle

estimate of McDonough and Sun (1995), and the pressures at which the solidus is

encountered are 30 kbar (solid line), 25 kbar (long dash), 20 kbar (medium dash), and 15

kbar (short dash). Diamonds indicate the melt fraction and pressure at which the residue

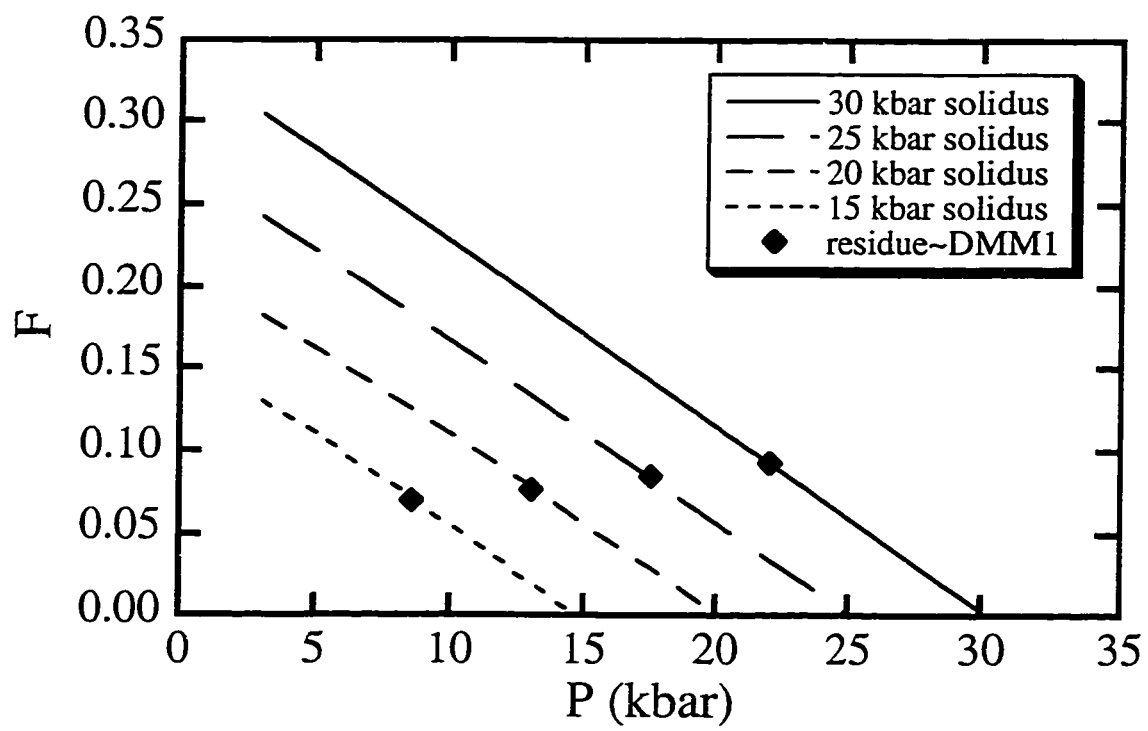most closely matches DMM1 in terms of Na_2O content.

Figure 4-7. Calculations using the MELTS-based algorithm of Asimow (1997) of the

pressures and melt fractions at which residues from polybaric, fractional melting of fertile

peridotite most closely resemble the composition of DMM1. As in Figure 4-6, initial

composition is that of McDonough and Sun (1995). Calculations are presented for mantle

potential temperatures of 1396°C (dot-dashed line), 1377°C (medium dash), 1358°C (dotted

line), 1339°C (long dash), 1320°C (short dash), and 1300°C (solid line). Diamonds

indicate the pressures and melt fractions at which the residue most closely matches DMM1

in terms of TiO_2 content. (a) Cumulative melt fraction versus pressure, (b) Instantaneous
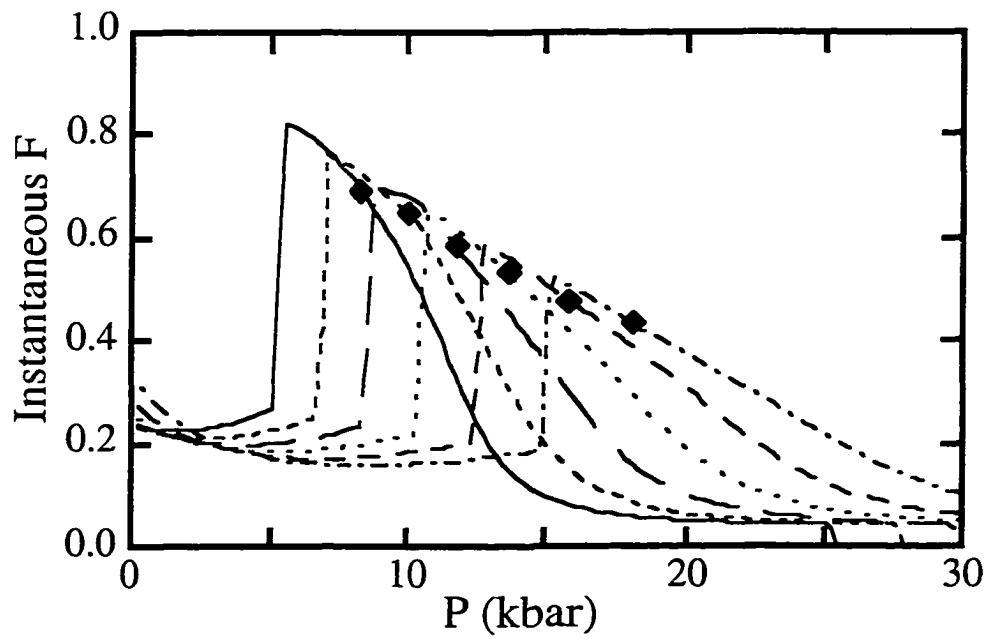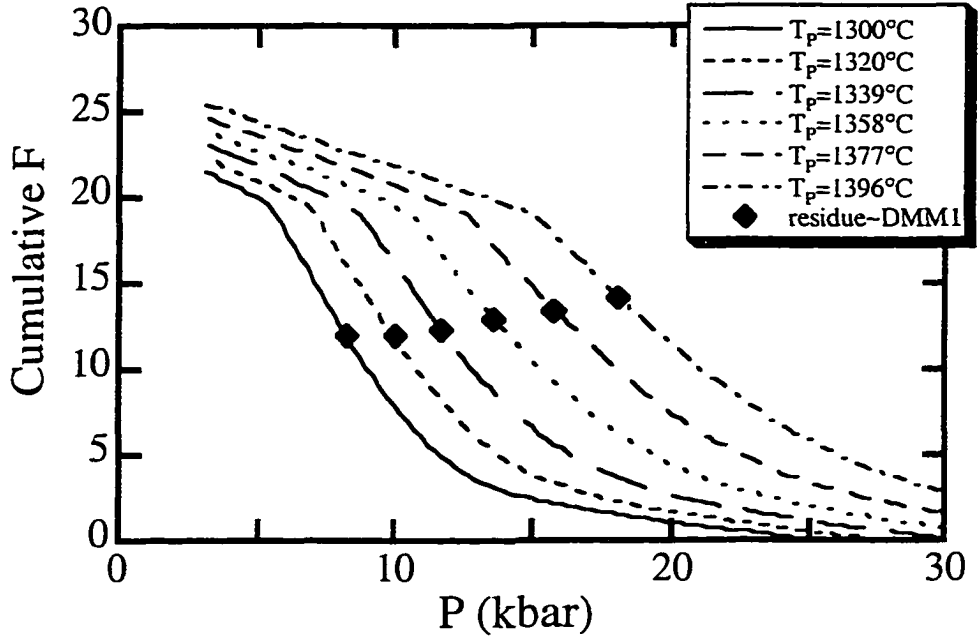
melt fraction versus pressure.

Figure 4-8. Comparison of experimentally-produced partial melts and MORB compositions. Squares represent the lowest melt fraction experiments at 30 kbar of Walter (1998). Triangle is lowest melt fraction experiment at 25 kbar on KLB-1 of Hirose and Kushiro (1993). Circles are lowest melt fraction partial melts of DMM1 (this study). Dashed field contains primitive MORB compositions (Elthon, 1990). Diagonally-hachured field contains MORB compositions corrected for low-pressure crystallization by olivine and spinel addition (Presnall and Hoover, 1978). Arrows indicate vector of olivine and spinel addition. (a) Na_2O vs. MgO, (b) SiO_2 vs. MgO, (c) FeO* vs. MgO.
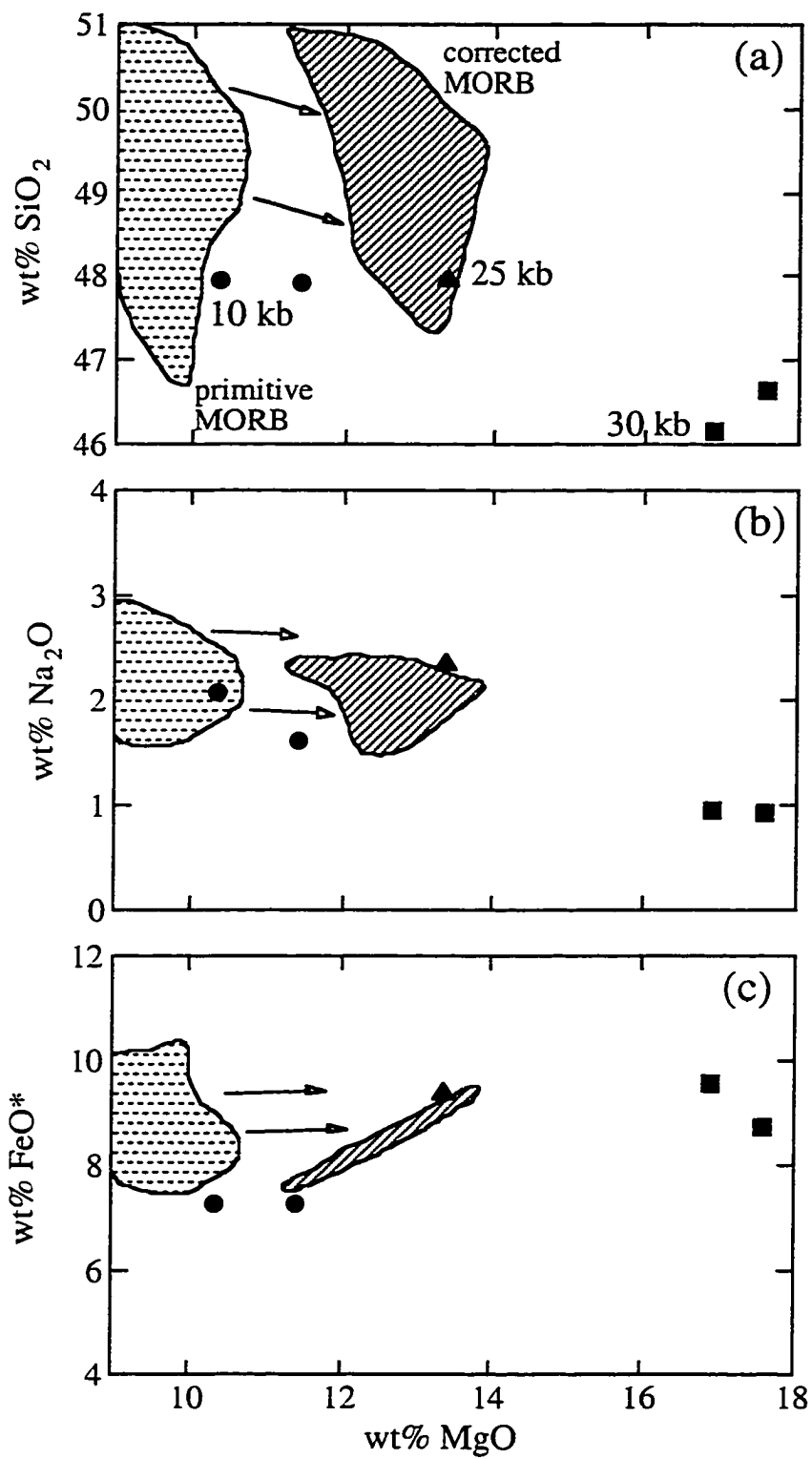
Chapter 5: Summary and future work

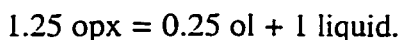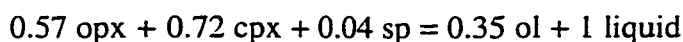As explained in Chapter 1, mid-ocean ridge basalts (MORB), which cover more than two-thirds of the earth's surface, are produced by fractional melting of peridotite in the earth's upper mantle. An important and necessary consequence of fractional melting is depletion of the source peridotite in incompatible major and trace elements. Those components which are incompatible within the peridotite's constituent minerals will preferentially enter the liquid phase as partial melting occurs, and as liquid continually separates and migrates away from the solid residue, the concentrations of incompatible components in the residue will drop markedly. As a result the peridotite becomes increasingly refractory, and the amounts and composition of liquids produced from it also change. The shallow parts of the melting zone beneath mid-ocean ridges are likely dominated by depleted peridotite, which thus plays a substantial role in determining the compositions of MORB magmas. Indeed, the models of Langmuir et al. (1992) and Asimow et al. (1997) predict that about half of the liquid produced in the melting column will be small degree partial melts of peridotite similar to the depleted composition studied in this thesis project (see Chapter 4).

Very little information about the melting behavior of depleted peridotite was available prior to the work presented in this thesis. The data reported here represent the first thorough study of partial melting of depleted peridotite, especially at very low melt fractions (<10%), which are particularly important for models of the fractional melting processes which produce MORB. To do this I used a new experimental technique involving aggregates of vitreous carbon which extract or segregate melt from the bulk sample and enable the partial melt to quench to a glass free of quench crystals and the associated compositional modifications that have plagued partial melting experiments in the past. Aggregate extraction experiments have been somewhat controversial in the literature,

but I have demonstrated that our experiments have approached equilibrium closely with partial reversals and excellent reproducibility in a large number of experiments using several variants of the extraction technique.

In Chapter 3, I presented a quantitative characterization of partial melting of depleted peridotite composition DMM1 at 10 kbar, briefly summarized here. TiO_2, Al_2O_3, and Na_2O concentrations in the liquid decrease with increasing degree of melting while MgO, SiO_2, Cr_2O_3, and FeO* concentrations increase. CaO content increases while clinopyroxene (cpx) is present in the residue, then decreases at temperatures above cpx exhaustion, which occurs between 1300° and 1310°C. Spinel-out also occurs within this temperature interval. Phase proportions calculated by mass balance indicate that melt productivity is ~0.11%/°C while cpx and spinel are still present, then somewhat lower (0.07%/°C). Extrapolation of the melt fraction versus temperature curve to a melt fraction of zero yields an estimated solidus of 1260°C. Melting reactions were determined by linear fit to crystalline phase proportions as a function of melt fraction both below and above cpx-out to be as follows:

0.57 opx + 0.72 cpx + 0.04 sp = 0.35 ol + 1 liquid

1.25 opx = 0.25 ol + 1 liquid.

These results make possible evaluation of the effects of source depletion on partial melting of mantle peridotite. When compared to results of partial melting experiments on fertile peridotite, our results show that alkali contents are significantly lower in partial melts of depleted peridotite. Even at 2-3% melting, Na_2O content is only about 2 wt%. As a consequence of the low alkali contents of partial melts of DMM1, SiO_2 contents of those melts are lower at low melt fractions than in partial melts of fertile peridotite. In addition, CaO contents of partial melts of depleted peridotite are higher, even though fertile source peridotites usually have substantially more CaO than depleted source rocks. CaO/Al_2O_3 is

also higher at a given melt fraction for depleted peridotite melting, implying that this ratio is

a function not only of melt fraction, but of source composition as well.

The results of this study also indicate that the bulk compositions of peridotite affect

peridotite solidus temperatures, melt productivity, and melting reactions. Solidus

temperatures of various peridotite compositions studied at 10 kbar define a strong, linear

correlation with Ti+Na+K+P, an index of source fertility. Isobaric melt productivity

appears from experimental studies to be negatively correlated with melt fraction and

positively correlated with source fertility, in contrast to theoretical expectations and

calculations using the MELTS algorithm of Ghiorso and Sack (1995). The discrepancy is

likely due to the procedure used to determine melt fraction in partial melting experiments.

Results also indicate that the melt fraction at which cpx is exhausted from the residue

during partial melting is linearly correlated with normative cpx content of the source

peridotite. This is corroborated by MELTS calculations of cpx-out for the DMM1 and

mm3 (Baker and Stolper, 1994) compositions with increments of cpx added or subtracted.

The data from experiments presented here allow assessment of how various methods of

calculating partial melt compositions perform when the source peridotite is depleted in

incompatible components. While offset in temperature, MgO, and SiO_2, the MELTS

program reproduces the shapes of oxide trends defined by our experiments quite well.

MELTS predicts that the chemical effects caused by high alkali contents in previous low

degree melting experiments on fertile peridotite (Baker et al., 1995; Hirschmann et al.,

1998a) will occur only below 0.5% melting in this system. The model of Kinzler and

Grove (1992a) also reproduces the trends well at melt fractions >4%, but deviates from the

experimental results at lower melt fractions. The algorithm of Langmuir et al. (1992)

successfully reproduces the experimentally-determined trends well. The importance of

these comparisons between experimental and calculated results is that MORB form by

fractional melting, which cannot be practically reproduced experimentally. Therefore,

models which use data from batch melting experiments for calibration, but calculate polybaric, fractional melting processes, are absolutely critical to our eventual understanding of how MORB primary magmas form and how the observed compositional differences in MORB can be explained. The better and more extensive the body of experimental data upon which these models are based, the more accurately they will be able to predict how peridotite of varying composition melts over the range of relevant temperatures and pressures, and the better they will be able to model realistically the petrogenesis of MORB.

The next step toward full characterization of depleted peridotite melting is to study low degree partial melts at pressures other than 10 kbar. I have attempted to conduct experiments at 20 kbar, but have encountered difficulties due to the rapid crystallization of vitreous carbon to graphite. A preliminary attempt to use aggregates of graphite pre-impregnated with glass was unsuccessful, but I believe that the technical problems involved with higher pressures can be overcome. Study of peridotite even more depleted than the moderately depleted composition DMM1 may also be useful. Experiments and calculations (see Chapter 4 for more information) indicate that as long as cpx is present and peridotite remains hot enough, melting will continue at a high rate. Thus in particularly cold areas of the mantle, very depleted peridotite may make a significant contribution to liquids destined to become MORB. Most importantly, the information gained through this work must be incorporated into quantitative models of MORB genesis. Depleted peridotite has melting behavior substantially different from the compositions studied previously, and until the models are able to accurately predict the amounts and compositions of melt generated from the full range of relevant source compositions, they cannot be expected to account for the chemical properties of MORB magmas and their causes realistically.

References

Albarede, F. and Provost, A. (1977) Petrological and geochemical mass-balance equations: An algorithm for least-square fitting and general error analysis. *Computers & Geosciences* 3:309-326.

Anderson, A.T. and Greenland, L.P. (1969) Phosphorus fractionation diagram as a quantitative indicator of crystallization differentiation of basaltic liquids. *Geochim. Cosmochim. Acta* 33:493-505.

Armstrong, J.T. (1988) Quantitative analysis of silicate and oxide minerals: comparison of Monte Carlo, ZAF and $\phi(\rho z)$ procedures. In *Microbeam Analysis*. (ed. D. E. Newbury) 239-246. San Francisco, San Francisco Press.

Asimow, P.D. (1997) A thermodynamic model of adiabatic melting of the mantle. California Institute of Technology Ph.D. thesis.

Asimow, P.D., Hirschmann, M.M. and Stolper, E.M. (1997) An analysis of variations in isentropic melt productivity. *Phil. Trans. R. Soc. London A* 355:255-281.

Baker, M.B. and Beckett, J.R. (1998, submitted) The origin of abyssal peridotites: a reinterpretation of constraints based on primary bulk compositions. *Earth Planet. Sci. Lett.*

Baker, M.B., Hirschmann, M.M., Ghiorso, M.S. and Stolper, E.M. (1995) Compositions of near-solidus peridotite melts from experiments and thermodynamic calculations. *Nature* 375:308-311.

Baker, M.B., Hirschmann, M.M., Wasylenki, L.E., Stolper, E.M. and Ghiorso, M.S. (1996) Reply to: Quest for low degree mantle melts. *Nature* 381:286.

Baker, M.B., Newman, S., Beckett, J.R. and Stolper, E.M. (1992) Separating liquid from crystals in high-pressure melting experiments using diamond aggregates. *GSA Abstracts with Program* 24:A256.

Baker, M.B. and Stolper, E.M. (1994) Determining the composition of high-pressure mantle melts using diamond aggregates. *Geochim. Cosmochim. Acta* 58(13):2811-2827.

Basaltic Volcanism Study Project (1981) *Basaltic Volcanism on the Terrestrial Planets.* New York, Pergamon Press.

Ben Othman, D. and Allegre, C.J. (1990) U-Th isotopic systematics at 13°N East Pacific Ridge segment. *Earth Planet. Sci. Lett.* 98:129-137.

Bertka, C.M. and Holloway, J.R. (1988) Martian mantle melts: An experimental study of iron-rich garnet lherzolite minimum melt composition. *18th Lunar and Planetary Science Conference*, Houston.

Bryan, W.B., Thompson, G., Frey, F.A. and Dickey, J.S. (1976) Inferred geological settings and differentiation in basalts from the Deep Sea Drilling Project. *J. Geophys. Res.* **81**:4285-4304.

Bryndzia, L.T. and Wood, B.J. (1990) Oxygen thermobarometry of abyssal spinel peridotites: the redox state and C-O-H volatile composition of the earth's sub-oceanic upper mantle. *Am. J. Sci.* **290**:1093-1116.

Bucher (1957) The crust of the earth. In *The Planet Earth*. 58-80. New York, Scientific American/Simon and Schuster.

Cameron, M. and Papike, J.J. (1981) Structural and chemical variations in pyroxenes. *Am. Mineral.* **66**:1-50.

Cawthorn, R.G., Ford, C.E., Biggar, G.M., Bravo, M.S. and Clarke, D.B. (1973) Determination of the liquid composition in experimental samples: discrepancies between microprobe analyses and other methods. *Earth Planet. Sci. Lett.* **21**:1-5.

Christie, D.M., Carmichael, I.S.E. and Langmuir, C.H. (1986) Oxidation states of mid-ocean ridge basalt glasses. *Earth Planet. Sci. Lett.* **79**:397-411.

Daines, M.J. and Richter, F.M. (1988) An experimental method for directly determining the interconnectivity of melt in a partially molten system. *Geophys. Res. Lett.* **15**(13):1459-1462.

Denbigh, K. (1981) *The principles of chemical equilibrium*. Cambridge, Cambridge University Press.

Dick, H.J.B. (1989) Abyssal peridotites, very slow spreading ridges and ocean ridge magmatism. In *Magmatism in the Ocean Basins*. (ed. A. D. Saunders and M. J. Norry) 71-105.

Dick, H.J.B. and Fisher, R.L. (1984) Mineralogic studies of the residues of mantle melting: abyssal and alpine-type peridotites. *Conf. Proc.: Kimberlites. II. The mantle and crust-mantle relationships*, Elsevier.

Dieckmann, R., Mason, T.O., Hodge, J.D. and Schmalzried, H. (1978) Defects and cation diffusion in magnetite (III.) Tracerdiffusion of foreign tracer cations as a function of temperature and oxygen potential. *Ber. Bunsenges. Phys. Chem.* **82**:778-783.

Dixon, J.E., Stolper, E.M. and Holloway, J.R. (1995) An experimental study of water and carbon-dioxide solubilities in mid-ocean ridge basaltic liquids. 1.Calibration and solubility models. *J. Petrol.* **36**(6):1607-1631.

Eggler, D.H. (1983) Upper mantle oxidation state: evidence from olivine-orthopyroxene-ilmenite assemblages. *Geophys. Res. Lett.* **10**:365-368.

Elthon, D. (1990) The petrogenesis of primary mid-ocean ridge basalts. *Reviews in Aquatic Sciences* **2**(1):27-53.

Engel, A.E.J. and Engel, C.G. (1964) Composition of basalts from the Mid-Atlantic Ridge. *Science* **144**:1-4.

Engel, A.E.J., Engel, C.G. and Havens, R.G. (1965) Chemical characteristics of oceanic basalts and the upper mantle. *GSA Bull.* **76**:719-734.

Engi, M. (1983) Equilibria involving Al-Cr spinel: Mg-Fe exchange with olivine. Experiments, thermodynamic analyses, and consequences for geothermometry. *Am. J. Sci.* **283-A**:29-71.

Falloon, T.J. and Green, D.H. (1987) Anhydrous partial melting of MORB pyrolite and other peridotite compositions at 10 kbar: Implications for the origin of primitive MORB glasses. *Mineralogy and Petrology* **37**:181-219.

Falloon, T.J. and Green, D.H. (1988) Anhydrous partial melting of peridotite from 8 to 35kb and the petrogenesis of MORB. *J.of Petrology* :379-414.

Falloon, T.J., Green, D.H., Hatton, C.J. and Harris, K.L. (1988) Anhydrous partial melting of a fertile and depleted peridotite from 2 to 30 kb and application to basalt petrogenesis. *J. Petrol.* **29**:1257-1282.

Falloon, T.J., Green, D.H., O'Neill, H.S.C. and Ballhaus, C.G. (1996) Quest for low degree mantle melts. *Nature* **381**:285.

Falloon, T.J., Green, D.H., O'Neill, H.S.C. and Hibberson, W.O. (1997) Experimental tests of low degree peridotite partial melt compositions: implications for the nature of anhydrous near-solidus peridotite melts at 1 GPa. *Earth Planet. Sci. Lett.* **152**:149-162.

Fujii, T. and Kushiro, I. (1977) Melting relations and viscosity of an abyssal tholeiite. *Carnegie Inst. Wash. Yearb.* **76**:461-465.

Gaetani, G.A. and Grove, T.L. (1998) The influence of water on melting of mantle peridotite. *Contrib. Mineral. Petrol.* **131**:323-346.

Gazis, C. and Ahrens, T.J. (1991) Solution and shock-induced exsolution of argon in vitreous carbon. *Earth Planet. Sci. Lett.* **104**:337-349.

Ghiorso, M.S., Carmichael, I.S.E., Rivers, M.L. and Sack, R.O. (1983) The Gibbs free energy of mixing of natural silicate liquids; an expanded regular solution approximation for the calculation of magmatic intensive variables. *Contrib. Mineral. Petrol.* **84**:107-145.

Ghiorso, M.S. and Sack, R.O. (1995) Chemical mass-transfer in magmatic processes 4. A revised and internally consistent thermodynamic model for the interpolation and extrapolation of liquid-solid equilibria in magmatic systems at elevated temperatures and pressures. *Contrib. Mineral. Petrol.* **119**:197-212.

Green, D.H. (1973) Experimental melting studies on a model upper mantle composition at high pressure under water-saturated and water-undersaturated conditions. *Earth Planet. Sci. Lett.* **19**:37-53.

Green, D.H., Falloon, T.J. and Taylor, W.R. (1987) Mantle derived magmas: role of variable source peridotite and variable C-H-O fluid compositions. In *Magmatic*

processes: physicochemical principles. (ed. B. O. Mysen) 139-154. Geochemical Society.

Grove, T., Kinzler, R. and Bryan, W. (1992) Fractionation of mid-ocean ridge basalt (MORB). In *Mantle Flow and Melt Generation at Mid-Ocean Ridges*. (ed. J. P. Morgan, D. Blackman and J. Sinton) 281-310. American Geophysical Union.

Grove, T.L. and Bryan, W.F. (1983) Fractionation of pyroxene-phyric MORB at low pressure: an experimental study. *Contrib. Mineral. Petrol.* **84**:293-309.

Gudfinnsson, G.H. and Presnall, D.C. (1995) Melting relations of model lherzolite in the CaO-MgO-Al₂O₃-SiO₂-FeO system at 7 to 28 kbar. *EOS, Transactions, AGU* **76**(46):696.

Gudmundsson, G. and Holloway, J.R. (1993) Activity -composition relationships in the system Fe-Pt at 1300 and 1400°C and at 1 atm and 20 kbar. *Am. Mineral.* **78**:178-186.

Gudmundsson, G., Holloway, J.R. and Carmichael, I.S.E. (1988) Pressure effect on the ferric/ferrous ratio in basaltic liquids. *EOS, Transactions, AGU* **69**:1511.

Harrison, W.J. (1981) Partitioning of REE between minerals and coexisting melts during partial melting of a garnet lherzolite. *Am. Mineral.* **66**:242-259.

Hart, S.R. and Zindler, A. (1986) In search of a bulk-earth composition. *Chem. Geol.* **57**:247-267.

Hays, J.F. (1966) Lime-alumina-silica. *Carnegie Inst. Wash. Yearb.* **65**:234-239.

Heald, E.F. (1967) Thermodynamics of iron-platinum alloy. *Trans. Metall. Soc. AIME* **239**:1337-1340.

Heezen, B.C. (1960) The rift in the ocean floor. *Scientific American* **203**(10):98-110.

Herzberg, C., Feigenson, M., Skuba, C. and Ohtani, E. (1988) Majorite fractionation recorded in the geochemistry of peridotites from South Africa. *Nature* **332**:823-826.

Hess, H.H. (1962) History of ocean basins. In *Petrologic Studies: A Volume to Honor A.F. Buddington*. 599-620. New York, Geological Society of America.

Hess, P.C. (1992) Phase equilibria constraints on the origin of ocean floor basalt. In *Mantle Flow and Melt Generation at Mid-Ocean Ridges*. (ed. J. P. Morgan, D. Blackman and J. Sinton) 67-102. American Geophysical Union.

Hirose, K. and Kawamoto, T. (1995) Hydrous partial melting of lherzolite at 1 GPa; the effect of H₂O on the genesis of basaltic magmas. *Earth Planet. Sci. Lett.* **133**:463-473.

Hirose, K. and Kawamura, K. (1994) A new experimental approach for incremental batch melting of peridotite at 1.5 GPa. *Geophys. Res. Lett.* **21**(19):2139-2142.

Hirose, K. and Kushiro, I. (1992) Partial melting of dry peridotites at high pressure: determination of compositions of melts segregated from peridotite using aggregates of diamonds. *EOS* **73**:615.

Hirose, K. and Kushiro, I. (1993) Partial melting of dry peridotites at high pressures: Determination of compositions of melts segregated from peridotite using aggregates of diamond. *Earth Planet. Sci. Lett.* **114**:477-489.

Hirschmann, M.M. (1991) Thermodynamics of multicomponent olivines and the solution properties of $(Ni,Mg,Fe)_2SiO_4$ and $(Ca,Mg,Fe)_2SiO_4$. *Am. Mineral.* **76**:1232-1248.

Hirschmann, M.M., Asimow, P.D., Ghiorso, M.S. and Stolper, E.M. (1998, submitted) Calculation of peridotite partial melting from thermodynamic models of minerals and melts. III. Controls on isobaric melt production and the effect of water of melt production. *J. Petrol.*

Hirschmann, M.M., Baker, M.B. and Stolper, E.M. (1998a) The effect of alkalis on the silica content of mantle-derived melts. *Geochim. Cosmochim. Acta* **62**:883-902.

Hirschmann, M.M., Ghiorso, M.S., Wasylenki, L.E., Asimow, P.D. and Stolper, E.M. (1998b) Calculation of peridotite partial melting from thermodynamic models of minerals and melts. I. Review of methods and comparison with experiments. *J. Petrol.* **39**(6):1091-1115.

Hirschmann, M.M., Wasylenki, L.E. and Stolper, E.M. (1996) Effect of peridotite major element heterogeneity on mantle melts. *EOS Trans. AGU* **77**(46):F847.

Holmes, A. (1928) Radioactivity and continental drift. *Geological Magazine* **65**:236-8.

Huebner, J.S. (1971) Buffering techniques for hydrostatic systems at elevated pressures. In *Research techniques for high pressure and high temperature.* (ed. G. C. Ulmer) 123-177. New York, Springer-Verlag.

Ihinger, P.D. (1991) An experimental study of the interaction of water with granitic melt. California Institute of Technology Ph.D. thesis.

Irvine, T.N. (1965) Chromian spinel as a petrogenetic indicator; Part 1, theory. *Can. Jour. Earth Sci.* **2**:648-671.

Ito, K. and Kennedy, G.C. (1967) Melting and phase relations in a natural peridotite to 40 kilobars. *Am. J. Sci.* **265**:519-538.

Jamieson, H.E., Roeder, P.L. and Grant, A.H. (1992) Olivine-pyroxene-PtFe alloy as an oxygen geobarometer. *Jour. Geol.* **100**:138-145.

Jaques, A.L. and Green, D.H. (1979) Determination of liquid compositions in experimental, high pressure melting of peridotite. *Am. Mineral.* **64**:1312-1321.

Jaques, A.L. and Green, D.H. (1980) Anhydrous melting of peridotite at 0-15 kb pressure and the genesis of tholeiitic basalts. *Contrib. Mineral. Petrol.* **73**:287-310.

Johnson, K.T. and Kushiro, I. (1992) Segregation of high-pressure partial melts from peridotite using aggregates of diamonds: a new experimental approach. *Geophys. Res. Lett.* **19**:1703-1706.

Johnson, K.T.M., Dick, H.J.B. and Shimizu, N. (1990) Melting in the oceanic upper mantle: an ion microprobe study of diopsides in abyssal peridotites. *J. Geophys. Res.* **95**:2661-2678.

Kinzler, R. (1997) Melting of mantle peridotite at pressures approaching the spinel to garnet transition: application to mid-ocean ridge basalt petrogenesis. *J. Geophys. Res.* **102**(B1):853-874.

Kinzler, R.J. and Grove, T.L. (1992) Primary magmas of mid-ocean ridge basalts 1. Experiments and methods. *J. Geophys. Res.* **97**(B5):6885-6906.

Kinzler, R.J. and Grove, T.L. (1992) Primary magmas of mid-ocean ridge basalts 2. Applications. *J. Geophys. Res.* **97**(B5):6907-6926.

Kinzler, R.J. and Grove, T.L. (1993) Corrections and further discussion of the primary magmas of mid-ocean ridge basalts, 1 and 2. *J. Geophys. Res.* **98**(B12):22,339-22,347.

Klein, E.M. and Langmuir, C.H. (1987) Global correlations of ocean ridge basalt chemistry with axial depth and crustal thickness. *J. Geophys. Res.* **92**:8089-8115.

Kushiro, I. (1975) On the nature of silicate melt and its significance in magma genesis: regularities in the shift of the liquidus boundaries involving olivine, pyroxene, and silica minerals. *Am. J. Sci.* **275**:411-431.

Kushiro, I. (1995) Compositions of partial melts formed in mantle peridotites at high pressures and their relation to those of primitive MORB.

Kushiro, I. (1996) Partial melting of a fertile mantle peridotite at high pressures: an experimental study using aggregates of diamond. In *Earth Processes: Reading the Isotopic Code*. 109-122. American Geophysical Union.

Kushiro, I. and Hirose, K. (1992) Experimental determination of composition of melt formed by equilibrium partial melting of peridotite at high pressures using aggregates of diamond grains. *Proc. Japan Acad.* **68, ser. B**(5):63-68.

Kushiro, I. and Thompson, R.N. (1972) Origin of some abyssal tholeiites from the Mid-Atlantic Ridge. *Carnegie Inst. Wash. Yearb.* **71**:403-406.

Langmuir, C., Klein, E.M. and Plank, T. (1992) Petrological systematics of mid-ocean ridge basalts: constraints on melt generation beneath ocean ridges. In *Mantle Flow and Melt Generation at Mid-Ocean Ridges*. (ed. J. P. Morgan, D. Blackman and J. Sinton) 183-280. American Geophysical Union.

Langmuir, C.H. and Hanson, G.N. (1980) An evaluation of major element heterogeneity in the mantle sources of basalts. *Phil. Trans. of the Royal Soc. of London A* **297**:383-407.

Le Grand, H.E. (1988) *Drifting Continents and Shifting Theories*. Cambridge, Cambridge University Press.

Lindsley, D.H. (1980) Phase equilibria of pyroxenes at pressures > 1 atmosphere. *Reviews in Mineralogy* 7:289-308.

Maaloe, S. and Aoki, K. (1977) The major element composition of the upper mantle estimated from the composition of lherzolites. *Contrib. Mineral. Petrol.* 63:161-173.

Mattioli, G.S., Baker, M.B., Rutter, M.J. and Stolper, E.M. (1989) Upper mantle oxygen fugacity and its relationship to metasomatism. *Jour. Geol.* 97:521-536.

Mattioli, G.S. and Wood, B.J. (1988) Magnetite activities across the Mg_2AlO_4-Fe_3O_4 spinel join, with application to thermobarometric estimates of upper mantle oxygen fugacity. *Contrib. Mineral. Petrol.* 98:148-162.

McDonough, W.F. and Frey, F.A. (1989) Rare earth elements in upper mantle rocks. In *Geochemistry and mineralogy of rare earth elements.* (ed. B. R. Lipin and G. A. McKay) 99-145. Washington, D.C., Mineralogical Society of America.

McDonough, W.F. and Sun, S.-s. (1995) The composition of the earth. *Chem. Geol.* 120:223-253.

McKenzie, D. (1984) The generation and compaction of partially molten rock. *J. Petrol.* 25:713-765.

McKenzie, D. (1985) The extraction of magma from the crust and mantle. *Earth Planet. Sci. Lett.* 74:81-91.

McKenzie, D. (1989) Some remarks on the movement of small melt fractions in the mantle. *Earth Planet. Sci. Lett.* 95:53-72.

McKenzie, D. and Bickle, M.J. (1988) The volume and composition of melt generated by extension of the lithosphere. *J. Petrol.* 29:625-679.

McMillan, P.F. and Wolf, G.H. (1995) Vibrational spectroscopy of silicate liquids. *Reviews in Mineralogy* 32:247-315.

Merrill, R.B. and Wyllie, P.J. (1973) Iron absorption by platinum capsules in high pressure rock melting experiments. *Am. Mineral.* 58:16-20.

Merzbacher, C.I. and White, W.B. (1991) The structure of alkaline-earth aluminosilicate glasses as determined by vibrational spectroscopy. *Journal of Non-Crystalline Solids* 130:18-34.

Navrotsky, A., Peraudeau, G., McMillan, P. and Coutures, J.-P. (1982) A thermochemical study of glass and crystals along the joins silica-calcium aluminate and silica-sodium aluminate. *Geochim. Cosmochim. Acta* 46:2039-2047.

Newman, S., Finkel, R.C. and Macdougall, J.D. (1983) ^{230}Th-^{238}U disequilibrium systematics in oceanic tholeiites from 21°N on the East Pacific Rise. *Earth Planet. Sci. Lett.* 65:17-33.

Nicholls, I.A. and Ringwood, A.E. (1973) Effect of water on olivine stability in tholeiites and the production of silica saturated magmas in the island arc environment. *Jour. Geol.* **81**:285-300.

Niu, Y. and Batiza, R. (1991) An empirical method for calculating melt compositions produced beneath mid-ocean ridges: application to axis and off-axis (seamounts) melting. *J. Geophys. Res.* **96**:21,753-21,777.

O'Hara, M.J. (1968) Are ocean floor basalts primary magmas? *Nature* **220**:683-686.

O'Neill, H.S.C. and Wall, V.J. (1987) The olivine-orthopyroxene-spinel oxygen geobarometer, the nickel precipitation curve, and the oxygen fugacity of the earth's upper mantle. *J. Petrol.* **28**(6):1169-1191.

Presnall, D.C., Dixon, J.R., O'Donnell, T.H. and Dixon, S.A. (1979) Generation of mid-ocean ridge tholeiites. *J. Petrol.* **20**(1):3-35.

Presnall, D.C., Dixon, S.A., Dixon, J.R., O'Donnell, T.H., Brenner, N.L., Schrock, R.L. (1978) Liquidus phase relations on the join diopside-forsterite-anorthite from 1 atm to 20 kbar: their bearing on the generation and crystallization of basaltic magma. *Contrib. Mineral. Petrol.* **66**:203-220.

Presnall, D.C. and Hoover, J.D. (1978) High pressure phase equilibrium constraints on the origin of mid-ocean ridge basalts. In *Magmatic Processes: Physicochemical Principles.* (ed. B. O. Mysen) 75-90. Geochemical Society.

Presnall, D.C. and Hoover, J.D. (1984) Composition and depth of origin of primary mid-ocean ridge basalts. *Contrib. Mineral. Petrol.* **87**:170-178.

Ringwood, A.E. (1975) *Composition and petrology of the earth's mantle.* New York, McGraw-Hill.

Ringwood, A.E. (1979) *Origin of the earth and moon.* New York, Springer-Verlag.

Robinson, J.A.C., Wood, B.J. and Blundy, J.D. (1998) The beginning of melting of fertile and depleted peridotite at 1.5 GPa. *Earth Planet. Sci. Lett.* **155**:97-111.

Ryerson, F.J. (1985) Oxide solution mechanisms in silicate melts - systematic variations in the activity-coefficient of SiO_2. *Geochim. Cosmochim. Acta* **49**:637-649.

Sack, R.O. and Ghiorso, M.S. (1989) Importance of considerations of mixing properties in establishing an internally consistent thermodynamic database--thermochemistry of minerals in the system Mg_2SiO_4-Fe_2SiO_4-SiO_2. *Contrib. Mineral. Petrol.* **102**:41-68.

Sack, R.O., Walker, D. and Carmichael, I.S.E. (1987) Experimental petrology of alkalic lavas: constraints on cotectics of multiple saturation in natural basic liquids. *Contrib. Mineral. Petrol.* **96**:1-23.

Schairer, J.F. (1954) The system K_2O-MgO-Al_2O_3-SiO_2: I, Results of quenching experiments on four joins in the tetrahedron cordierite-forsterite-leucite-silica and on the

join cordierite-mullite-potash feldspar. *Journal of the American Ceramic Society* **37**:501-533.

Schilling, J.-G. (1986) Geochemical and isotopic variation along the Mid-Atlantic Ridge axis from 79°N to 0°N. In *The Western North Atlantic Region.* (ed. P. R. Vogt and B. E. Tucholke) Geological Society of America.

Schilling, J.-G., Zajak, M., Evans, R., Johnson, T., White, W. and Devine, J.D. (1983) Petrologic and geochemical variations along the Mid-Atlantic Ridge from 29°N to 73°N. *Am. J. Sci.* **283**:510-586.

Sen, G. (1982) Composition of basaltic liquids generated from a partially depleted lherzolite at 9 kbar pressure. *Nature* **299**:336-338.

Shaw, D.M. (1970) Trace element fractionation during anatexis. *Geochim. Cosmochim. Acta* **34**:237-243.

Shen, Y. and Forsyth, D.W. (1993) Geochemical constraints on initial and final depths of melting beneath mid-ocean ridges. *J. Geophys. Res.* **100**(B2):2211-2237.

Shi, P. (1993) Low-pressure phase relationships in the system Na_2O-CaO-FeO-MgO-Al_2O_3-SiO_2 at 1100°C, with implications for the differentiation of basaltic magmas. *J. Petrol.* **34**:743-762.

Stolper, E.M. (1980) A phase diagram for mid-ocean ridge basalts: preliminary results and implications for petrogenesis. *Contrib. Mineral. Petrol.* **74**:13-27.

Stolper, E.M. and Newman, S. (1994) The role of water in the petrogenesis of Mariana trough magmas. *Earth Planet. Sci. Lett.* **121**:293-325.

Takahashi, E. (1986) Melting of a dry peridotite KLB-1 up to 14 GPa: implications on the origin of peridotitic upper mantle. *J. Geophys. Res.* **91**(B8):9367-9380.

Takahashi, E. and Kushiro, I. (1983) Melting of a dry peridotite at high pressures and basalt magma genesis. *Am. Mineral.* **68**:859-879.

Ulmer, P. (1989) The dependence of the Fe^{2+}-Mg cation partitioning between olivine and basaltic liquid on pressure, temperature and composition: an experimental study to 30 kbars. *Contrib. Mineral. Petrol.* **101**:261-273.

von Bargen, N. and Waff, H.S. (1986) Permeabilities, interfacial areas and curvatures of partially molten systems: results of numerical computations of equilibrium microstructures. *J. Geophys. Res.* **91**:9261-9276.

Waff, H.S. and Bulau, J.R. (1979) Equilibrium fluid distribution in an ultramafic partial melt under hydrostatic stress conditions. *J. Geophys. Res.* **84**:6109-6114.

Walter, M.J. (1998) Melting of garnet peridotite and the origin of komatiite and depleted lithosphere. *J. Petrol.* **39**:29-60.

Walter, M.J. and Presnall, D.C. (1994) Melting behavior of simplified lherzolite in the system CaO-MgO-Al$_2$O$_3$-SiO$_2$-Na$_2$O from 7 to 35 kbar. *J. Petrol.* **35**(2):329-359.

Walter, M.J., Sisson, T.W. and Presnall, D.C. (1995) A mass proportion method for calculating melting reactions and application to melting of model upper mantle lherzolite. *Earth Planet. Sci. Lett.* **135**:77-90.

Wasylenki, L.E., et al., EOS Trans AGU, 77(46), F847 (1996) (1996) The effect of source depletion on equilibrium mantle melting. *EOS Trans. AGU* **77**(46):F847.

Watson, E.B. (1991) Diffusion in fluid-bearing and slightly-melted rocks--experimental and numerical approaches illustrated by iron transport in dunite. *Contrib. Mineral. Petrol.* **107**:417-434.

Watson, S. and McKenzie, D. (1991) Melt generation by plumes: a study of Hawaiian volcanism. *J. Petrol.* **32**:501-537.

Wendlandt, R.F. and Mysen, B.O. (1980) Melting phase relations of natural peridotite + CO$_2$ as a function of degree of partial melting at 15 and 30 kbar. *Am. Mineral.* **65**:37-44.

Wiser, N.M. and Wood, B.J. (1991) Experimental determination of activities of Fe-Mg olivines at 1400K. *Contrib. Mineral. Petrol.* **108**:146-163.

Wyllie, P.J. (1976) *The Way the Earth Works*. New York, John Wiley and Sons.

Yang, H.-J., Kinzler, R.J. and Grove, T.L. (1996) Experiments and models of anhydrous, basaltic olivine-plagioclase-augite saturated melts from 0.001 to 10 kbar. *Contrib. Mineral. Petrol.* **124**:1-18.